

3 (1947)



This is to certify that the

dissertation entitled

The Triple Differential Di-Jet

Cross Section at SQRT(S) = 1.8 TeV
presented by

Gian Giuseppe Di Loreto

has been accepted towards fulfillment of the requirements for

Doctor of Philosophy degree in Physics

H. Weerbs

Major professor

Date 11/13/98

MSU is an Affirmative Action/Equal Opportunity Institution

0-12771



# PLACE IN RETURN BOX to remove this checkout from your record. TO AVOID FINES return on or before date due. MAY BE RECALLED with earlier due date if requested.

DATE DUE	DATE DUE	DATE DUE
-		

1/98 c/CIRC/DateDue.p85-p.14

Тне

# The Triple Differential Di-Jet Cross Section at $\sqrt{s}=1.8$ TeV

By

Gian Giuseppe Di Loreto

### A DISSERTATION

Submitted to
Michigan State University
in partial fulfillment of the requirements
for the degree of

### DOCTOR OF PHILOSOPHY

Under the Supervision of Professor Hendrik Weerts

Department of Physics and Astronomy

### **ABSTRACT**

The Triple Differential Di-Jet Cross Section at  $\sqrt{s}=1.8~{\rm TeV}$ 

By

#### Gian Giuseppe Di Loreto

The Measurement of the Triple Differential di-jet cross section at DØ is described. The cross section is corrected for all known detector effects and compared to currently available theoretical predictions from the CTEQ and MRST groups. Of the theories considered, the preliminary measurement favors the CTEQ4M and MRSTg† parton distribution functions. The measurement combined with a detailed error analysis shows considerable discriminatory power among the current theories.

T.

JSL.

end of

₽6:p],ŧ

Micki

ľď

of Ro

and f

Si:

the ca

my m

δekt.c,

.<del>}</del>:

lest n

હ્યાતું ]

#### **ACKNOWLEDGEMENTS**

This Dissertation is the cumulative effort of many years of work, some at Fermilab and some at Michigan State University. I have often made the claim that attending MSU was the best decision I had ever made, and I'm happy to report that at the end of my long tenure there, I'll stick to that statement. The graduate student experience can be a grueling one and without the support and friendship of many people, I'd never have made it. I'll attempt to acknowledge them below.

I'd like to start by acknowledging a man who, without my asking, spoke with Michigan State University on my behalf while I was still a student at The University of Rochester. By that action, Professor Tom Ferbel steered the course of my life, and for it, has my sincere gratitude.

Sincere thanks to Bernard Pope who also contributed to fishing me, through the Rochester-MSU pipeline, out of college. Bernard was there during the early classes, the candidacy exam, all the way to the end. I hope after all this, I've made up for my miserable performance on the entrance exam. Thank you, Bernard.

At first, MSU was both a wonderful and overwhelming place to be. I'd like to acknowledge Dave Brown, Mike Wiest, Kenny, Ty, (forgive me, I never knew their last names), and Jac Caggiano for their friendship. Special thanks go to Jon Kruse and Joelle Murray who not only profoundly changed the way I think about physics,

but a

Ľ

phys.

first f

on ti

to th.

the er

T:

of ti.

to ack

Elvira away

many

Specia

Studio

1,

 $v_{\rm Cop}$ 

 $W_{M,\delta}$ 

 $A_{
m S}$ 

rane,

to, wil

Davis,

but also life, death, and most things in between (including waffle irons).

During my time at Fermilab, I have had the distinct pleasure of knowing many physicists who've shaped this analysis and me as a scientist in the process. The first face I saw here belonged to Rich Astur, who helped me get started, working on the showering correction which I'm sorry to say, still isn't understood. I'd like to thank Terry Geld and Jerry Blazey whose initial enthusiasm for me was exactly the encouragement a new student needs.

The analysis presented in this thesis would not exist without the combined effort of the DØ experiment, and especially the QCD and energy scale groups. I'd like to acknowledge my debt to all of them, and a few of them by name. To Daniel Elvira, Nikos Varales, Rich Partridge, and Mark Strovink, for never letting me get away with anything. To Harry Melanson, Andrew Brandt, and Greg Snow, for many encouraging words. To John Womersley for many, many sarcastic comments. Special thanks to Heidi Schellman for her thoughtful work on the vertex resolution studies.

I would like to give special thanks to Bob Hirosky, and Iain Bertram who developed much of the techniques and computer code used to perform this analysis. Without their help, this thesis would be *years* away from where it is today.

As I have mentioned, the graduate student experience is a difficult one, however the hardships here are eased greatly by the company of others in the same boat, namely other graduate students. Among those whom I'd like to express my gratitude to, whom I've had the privilege to work with, are Sal Fahey, Ki-Suk Hahn, Kevin Davis, Kathy Fatyga, Jill Perkins, Kate Frame, Tracy Taylor-Thomas, Tacy Joffe-

Mine

Rob :

a pr

times

S:

peach:

emet;

Ву a fello

John i

 $J_{0 \rm mR} \}$ 

analy:

this re

A: lab i

outsi.

Chica

that

 $S_{0011}$ 

The

Were

for t

Ĭ:

Minor, and Tom Rockwell. I've enjoyed a long friendship with another student, Rob Snihur, whose insight into physics, pool, basketball, and meeting girls has had a profound impact on me and has helped make graduate school downright fun at times.

Steve Jerger has been a valued friend during this experience, we lived together peacefully against all odds and he continues to be a valued source of support, 90% emotional and 10% financial.

By far, the largest debt owed by this analysis is payable to John Krane. Although a fellow student, his insight and expertise has profoundly influenced this thesis. If John hadn't come to DØ, the Triple Differential as we know it now would not exist. John has filled the roles of post-doc, editorial board, and thesis committee to this analysis. It would not overstate things to say he deserves almost as much credit for this result as do I.

As much a part of my graduate student life as Fermilab, my life outside the lab helped keep me (almost) sane and the people I've met and come to rely on outside the field deserve recognition as well. I'd first like to thank my friends from Chicago and Oak Park who have helped get my mind off physics when it needed that most. These include Eric Duskin, Bill, Steve, and Stephanie, Jamie Damato, Scott and Wendy Baxter, and all the other folks from 58 West Superior, Oak Park. The evenings spent in your company enjoying a fine cigar, cocktail, and conversation were some of the most memorable of my life.

In Chicago I'd like to express my thanks to Mike Dominick and Steve Jackson for teaching me you can be sensitive but still ride around on a large, old motorcycle.

Credit goes to and compani-Additional corner bar for and I knew no iong, but alwa Among the have helped in McMurtry, Je Vaughn, The I Prisig, John Iand Lyle Love I have ack men who fall months of my the long com erjoyed cover I learned fro: benefited im:

> Dylan Cas Vears of gra

my thinking a

Credit goes to Karen Cassidy and Lisa Kramer for consistently providing friendship and companionship through many long and arduous years.

Additionally I'd like to thank the staff and regulars of the Inner Town Pub, my corner bar for awhile, who provided me a place to go when I was living in the city and I knew no one. The nights spent there playing pool were often strange and too long, but always memorable.

Among the list of people to whom I am grateful and who, in one way or another have helped me finish this thesis, but who may not know who I am are: James McMurtry, John Fogerty, David Lowery, Robert Smith, Chris Issak, Stevie Ray Vaughn, The Reverend Horton Heat, David Lynch, S.C.O.T.S, Annie Proulx, Robert Prisig, John Krackower, Sammy Sosa, Michael Jordan, Honda Motorcycles U.S.A., and Lyle Lovett.

I have acknowledged the support of friends and fellow scientists, there are two men who fall heavily into both categories, Jim Jaques and Dylan Casey. For many months of my graduate career, Jim, Dylan, and Simon (Dylan's son) and I endured the long commute from Oak Park to Fermilab together. The conversations we enjoyed covered music, love, cars, martial arts, in addition to, of course, physics. I learned from both of them during these commutes, my mind and my analysis benefited immensely from their company. Jim deserves special credit for starting my thinking about the offset correction.

Dylan Casey deserves special recognition for consistent friendship during almost 7 years of graduate school. It may be that opposites attract, but in our case our combined love for Lyle Lovett, guitars, motorcycles and lengthy discussions regard-

ing statistica I thank you. One of the between you own family. a Jason, Debor and Matthew turn of event from your pro In spite of all kinds of su brother who calling me to watch togeth With suggest! at baseball g this thesis po never forget p ) ou, Greg  $D_i$ provided my to go to colle many late nic other daily car ing statistical significances, I suspect, will be fuel for many more years of comraderie.

I thank you, Dr. Casey.

One of the more difficult aspects of graduate school is the distance it places between you and your family. I am doubly lucky in this regard in that I have my own family, and that of my fiancée. I extend sincere thanks to Pola, Daniel, Ryan, Jason, Deborah, David, and André Aguirre, to Anthony, Leticia, Jennelle, Jillian and Matthew Madrigal. I hope I can someday convey to you all what a fantastic turn of events it was for me to meet you all and how much this thesis has benefited from your presence in my life.

In spite of the many miles between all of us, my own family has provided me with all kinds of support and encouragement throughout my academic career. My "little" brother who consistently reminds me to look at the larger picture by, for example, calling me to tell me about the Vanilla Ice movie right now on VH1, which we then watch together, thank you, Glenn Di Loreto. My older brother was always there with suggestions when things weren't going right. His companionship in Chicago at baseball games, movies, and the coffee shop went a long way towards making this thesis possible. I don't know if I would have lasted out here without him. I'll never forget passing the candidacy exam and seeing his face when I told him. Thank you, Greg Di Loreto. Early trips to see my sister at the University of Pennsylvania provided my first peek into academics, they were largely responsible for my desire to go to college. Since then, she has been there every step of the way, through many late night phone calls regarding problematic relationships, sick animals and other daily catastrophes. Her consistent support and love is one of my most favorite

things; that

When I

my dad. My
how things
this thesis.

a mo-ped st
job" he said

curiosity, an my self.

the Italians  $\,$ 

of work, to

Of all the

understandin

my brothers

decision since

Rhoads-Di L.

Any Ph.D

In my case, I

young student

trails of class

that I could g

DO data. Thi

things; thank you, Gioia (and Bob and Nathaniel) Sharp.

When I was very young, I found a cassette player that didn't work and I gave it to my dad. My father's fixing this thing started me down this long path of wondering how things work, a path that has led me through many years of classes and finally this thesis. A scene is brought to mind during which we were both trying to get a mo-ped started with the kill switch off. "Never leave two Italians alone to do a job" he said. I hope by graduating I've brought some pride to my father and all the Italians on his side of my family. I thank you Giuseppe Di Loreto for giving me curiosity, and a desire to understand things. It has grown into a defining quality of my self.

Of all the people who have contributed in some small (or large) way to this body of work, to no one am I more grateful to than my mother. At some point when I was young, she was able to convey to me a respect for science, intelligence and understanding. When I was very small, listening to her speak, sing, or debate with my brothers and sister stuck with me. I have had to make more than one difficult decision since then; she has influenced them all. Thank you most of all, Gretchen Rhoads-Di Loreto.

Any Ph.D. thesis is likely to contain an acknowledgement of the thesis advisor. In my case, I owe an enormous debt to my advisor, Harry Weerts. Unlike most young students at Michigan State, I had an advisor from the beginning. The early trails of class and exams were put into a larger context by Harry who reminded me that I could get through them and then begin working on the real important thing, DØ data. This promise was a guiding light through many tough months at MSU.

After more gratef
the confusir
experiment
always beer
quality, and
friend throughout the confusir

the future, a

putting up a

problems wi

academic ca

These ac

this disappea

But Laur We've gotter: together.

October 7, 19

After moving to Fermilab and getting to know Harry as a scientist, I became even

more grateful to have him as my advisor. Harry has the unique gift to see through all

the confusing notation, jargon, and other noise that often surrounds a complicated

experiment and analysis, through to the really important core. Although I haven't

always been grateful for this (it's hard to pull anything over on him), it is a rare

quality, and this analysis has benefited from it greatly. Harry has also been a good

friend through all this, we have more in common than I ever expected. Thank you

for everything Harry, I've learned more from you than from any other person in my

academic career.

These acknowledgements have dealt largely with the past, let me turn now to

the future, the future I owe largely to my fiancée, Laura Aguirre. Thank you for

putting up with the months of stress, for listening to me babble on about various

problems with this analysis, for dealing with me as my ability to see the end to all

this disappeared and reappeared weekly.

But Laura, thank you most of all for you, for your fire, spice, and lust for life.

We've gotten me through graduate school, honey, let's see what else we can get done

together.

October 7, 1998. Chicago, Il

vii

"To wonder is to begin to understand."

(unknown)

# Cont

ΙΙ	ntroc
----	-------

1.1 A

1.2 M

1.:

1.:

1.2

## 2 Quantu

2.1 Th

2.1

2.1

2.1.

2.1.

2.1.5

2.2 NLO

### **Contents**

1	Intr	troduction		1
	1.1	A Brie	ef History of Particle Physics	1
	1.2	Moder	rn Particle Physics	5
		1.2.1	Forces	6
		1.2.2	Modern Experimental Particle Physics	7
		1.2.3	Quantum Chromodynamics	8
2	2 Quantum Chromodynamics		10	
	2.1	The G	Golden Rule	11
		2.1.1	Calculating Matrix Elements	12
		2.1.2	Parton Distribution Functions	13
		2.1.3	Radiative, Loop Corrections and Next to Leading Order	19
		2.1.4	Total Next to Leading Order Predictions	20
		2.1.5	Loop Corrections and Renormalization	21
	2.2	NLO	QCD and the Triple Differential	22

2.2

2.3 Ti

2...

2.3

2.4 In

2.

2.

3 The Te

3.1 T

3.2 T

3.

3.

3.

3.

3.

3.3 D

3.

3..

3.:

		2.2.1	Hadronization and Jets	22
	2.3	The T	riple Differential Di-Jet Cross Section	27
		2.3.1	Choice of Variables	28
		2.3.2	$x_1, x_2$ and the Triple Differential $\dots \dots \dots \dots$	29
	2.4	Imple	mentation of QCD, Monte Carlo Predictions	33
		2.4.1	Jetrad	33
		2.4.2	Herwig	33
3	The	Tevat	ron, the DØ Detector and Jets	35
	3.1	The F	ermilab Tevatron	35
	3.2	The D	ØØ Detector	39
		3.2.1	Tracking	41
		3.2.2	The DØ Muon System	41
		3.2.3	Level Zero	41
		3.2.4	Luminosity Calculation	42
		3.2.5	The DØ Calorimeter	43
	3.3	Data	Filtering and Reconstruction	48
		3.3.1	The DØ Trigger System	48
		3.3.2	Offline Reconstruction	49
		3.3.3	Triggers	50

4.2 Qu

4.2

4.2.

4.2.

4.3 Cor

4.3.

4.4 Jet

4.4.1

4.4.2

4.4.3

4.4.1

4.4.5

4.4.6

4.4.7

5 Resolutio

5.1 Jet E

	3.4	Jet De	efinitions	. 51
4	The	Data		54
	4.1	The M	Seasurement	. 54
	4.2	Qualit	zy Cuts	. 56
		4.2.1	Missing $E_T$ cut	. 56
		4.2.2	Vertex Position	. 60
		4.2.3	Jet Quality Cuts	. 63
	4.3	Correc	ctions to the Data	. 71
		4.3.1	Jet $\eta$ Definition	. 71
	4.4	Jet Er	nergy Scale Corrections	. 79
		4.4.1	The Offset Correction	. 80
		4.4.2	Physics Underlying Event Correction	. 88
		4.4.3	Out of Cone Showering Correction	. 90
		4.4.4	The Response Correction	. 91
		4.4.5	Energy Scale Closure Tests	. 93
		4.4.6	Energy Scale Error	. 94
		4.4.7	Cross Section Energy Scale Error Estimation from Data	. 98
5	Res	olutio	ns and Unsmearing	103
	5.1	Jet Er	nergy Resolutions	. 104

5.1

5.1

5.1

5.1

5.2 Jet5.3 Un

5.4 Des

5.4

5. 1.

6 Results.

6.1 Gra

6.2 Qua

6.2.

6.2.2

6.2.3

6.2.4

		5.1.1	Soft Third Jet and Particle Out of Cone Corrections 1	05
		5.1.2	Vertex Position Resolution and Di-Jet Asymmetry	09
		5.1.3	Monte Carlo Closure of the Vertex Position Resolution Mea-	
			surement	20
		5.1.4	The Plan	22
	5.2	Jet Er	nergy Resolution Results	23
	5.3	Unsme	earing the Data	23
	5.4	Deriva	ation of Vertex Position Resolution Correction	128
		5.4.1	Outline of Assumptions	128
		5.4.2	Correction Derivation and Implementation	32
6	Res	ults, E	Error Analyses, and Conclusions	36
	6.1	Graph	nical Comparisons to Theory	136
	6.2	Quant	sitative Theory Comparisons	156
		6.2.1	Construction of the Covariance Matrix for Errors not Associ-	
			ated with the Energy Scale Correction	157
		6.2.2	Construction of the Covariance Matrix for Errors Associated	
			with the Energy Scale Correction	159
		6.2.3	$\chi^2$ Tests	162
		6.2.4	Conclusion	163

A Resolut

A.1 Zero

A.2 Clo

A.2

B Numeri

Bibliograp

A	Res	Resolution Monte Carlo Closure	
	A.1	Zero Bias Overlay	165
	A.2	Closure Tests	165
		A.2.1 Vertex Position Resolution and Energy Resolution Closure	168
В	Nur	merical Cross Sections	170
Bi	bliog	graphy and Notes	177

# List o

- 1.1 Kn
- 2.1 Qu
- 2.2 Bir.
- 2.3 x s
- 3.1 Ma
- 3.2 Jet
- 4.1 E<sub>T</sub>
- 4.2 Ver
- 4.3 Jet
- 4.4 Err
- 4.5 Sou
- 4.6 Sou
- 4.7 Sour

### List of Tables

1.1	Known forces and their mediators	7
2.1	Quarks: masses and charges	12
2.2	Binning of the Triple Differential	28
2.3	x space covered by the Triple Differential	30
3.1	Major components of the Fermilab Tevatron	37
3.2	Jet triggers used in the Triple Differential	50
4.1	$ \mathcal{E}_T $ efficiency for the 8 slices considered in the Triple Differential	59
4.2	Vertex cut efficiency and errors	62
4.3	Jet Quality Cuts	66
4.4	Errors on the cross sections due to the total $\eta$ bias	74
4.5	Sources of energy scale correction errors for central jets	95
4.6	Sources of energy scale correction errors for central jets	95
4.7	Sources of energy scale correction errors for central jets	96

5.1 Fra

5.2 So

6.1 Fra

fer

6.2 Fra

fere

6.3 Sot

6.4 Sot

 $6.5 - \chi^2$ 

B.1 The

B.2 The

B.3 The

B.4 The

B.5 The

B.6 The

B.7 The

B.8 The

5.1	Fraction of single vertex events for all slices
5.2	Sources and magnitudes of unfolding error
6.1	Fractional (%) error components for slices 1 and 2 of the Triple Dif-
	ferential
6.2	Fractional (%) error components for slices 3 and 4 of the Triple Dif-
	ferential
6.3	Sources of error in the Triple Differential and their correlations 156
6.4	Sources of energy scale error and their correlations
6.5	$\chi^2$ test results for the Triple Differential
B.1	The DØ Triple Differential for same side events, $ \eta  \leq 0.5$ 171
B.2	The DØ Triple Differential for same side events, $0.5 \le  \eta  \le 1.0.$ 172
B.3	The DØ Triple Differential for same side events, $1.0 \le  \eta  \le 1.5.$ 173
B.4	The DØ Triple Differential for same side events, $1.5 \le  \eta  \le 2.0.$ 173
B.5	The DØ Triple Differential for opposite side events, $ \eta  \leq 0.5$
B.6	The DØ Triple Differential for opposite side events, $0.5 \le  \eta  \le 1.0$ 175
B.7	The DØ Triple Differential for opposite side events, $1.0 \le  \eta  \le 1.5$ 176
B.8	The DØ Triple Differential for opposite side events, $1.5 \le  \eta  \le 2.0$ 176

## List

- 2.1 Th
- 2.2 A s
- 2.3 An
- 2.4 Tw
- 2.5 Lea
- 2.6 Hig
- 2.7 Sun
- 2.8 Gra
- 2.9 Rep
- 3.1 Ove
- 3.2 Coor
- 3.3 The
- 3.4 A Do

# List of Figures

2.1	The CTEQ3M parton distribution function	15
2.2	A simple diagram for parton-parton scattering	17
2.3	An example of a radiative correction	19
2.4	Two examples of loop corrections	20
2.5	Leading order diagrams for di-jet production	23
2.6	Higher order diagrams for di-jet production	24
2.7	Summary of contributions to QCD jet production	26
2.8	Graphical representation of $x$ coverage of all slices and topologies of	
	the Triple Differential.	31
2.9	Representative slices of the Triple Differential and their $\boldsymbol{x}$ coverage	32
3.1	Overview or the Fermilab Tevatron	36
3.2	Coordinates used in the DØ detector	40
3.3	The DØ liquid argon calorimeter	44
3.4	A DØ calorimeter cell	45

3.5 :

3.6

3.7 E

4.1 (

4.2 E

4.3 E

4.4 Sc

4.5 Ve

4.6 Re

ьп

4.7 Jet

4.8 Jet

4.9 Jet

4.10 Jet

4.11 Tot

4.12 Tor.

4.13 Tota

4.14 Tota

4.15 The

4.16 Mock

3.5	A cross section of the DØ calorimeter	46
3.6	An event as seen by the DØ detector	47
3.7	Block diagram of the DØ trigger system	49
4.1	Cartoon representation of jets for two slices of the Triple Differential.	55
4.2	$E_{Tlead}/E_{T}$ for Same Side central jets	57
4.3	$E_{Tlead}/E_{T}$ for all slices	58
4.4	Schematic of the calculation of the efficiency associated with the $\not\!\!E_T$ cut.	60
4.5	Vertex Distribution (before cuts) for two slices of the Triple Differential.	62
4.6	Representative electromagnetic and coarse hadronic fraction distri-	
	butions	65
4.7	Jet and event quality cuts efficiencies and errors for slice 1	67
4.8	Jet and event quality cuts efficiencies and errors for slice 2	68
4.9	Jet and event quality cuts efficiencies and errors for slice 3	69
4.10	Jet and event quality cuts efficiencies and errors for slice 4	70
4.11	Total $\eta$ bias as measured in Herwig as a function of jet $\eta$	74
4.12	Total $\eta$ bias as measured in Herwig as a function of jet energy	75
4.13	Total $\eta$ bias before and after the total $\eta$ bias correction	76
4.14	Total fractional $\eta$ bias error for all slices as a function of jet $E_T$	77
4.15	The effect of the total $\eta$ bias corrections on the forward cross sections.	78
4.16	Mock plot of energy in a calorimeter cell due to uranium decay	82

4.17 Occ

sup

4.18 Ene

4.19 Ene

4.20 Ene

4.21 The

4.22 The

4.23 The

4.24 Ener

4.25 Ener

4.26 Ener

4.27 Ener

4.28 The

5.1 An

fit.

5.2 E<sub>Xa</sub>

 $^{5.3}$   $\mathrm{U}_{\mathrm{he}}$ 

5.4 Unc.

4.17	Occupancies for the different data sets used in the derivation of the	
	suppression correction	83
4.18	Energy introduced into zero bias data due to zero suppression 8	84
4.19	Energy due to zero suppression in zero bias and jet data together	
	with prediction based on occupancy.	86
4.20	Energy density due to physics underlying event	89
4.21	The total offset correction for different luminosity bins	89
4.22	The out-of-cone showering energy correction factors (S) and errors	
	for different $\eta$ bins	91
4.23	The jet response for jets in the DØ calorimeters	93
4.24	Energy scale Monte Carlo closure test	94
4.25	Energy scale energy correction factors for jets of different rapidity 9	97
4.26	Energy scale factors to the cross sections and errors for slices 1 and 2	99
4.27	Energy scale factors to the cross sections and errors for slices 3 and 4 10	00
4.28	The raw Triple Differential cross section	02
5.1	An example of an asymmetry distribution, together with a Gaussian	
	fit	05
5.2	Example of the third jet cut extrapolation	06
5.3	Uncorrected jet energy resolutions for two central slices	07
5.4	Uncorrected jet energy resolutions for two forward slices	08

5.5

5.6 V

5.7 F

5.8 F

5.9 S

5.10 E

 $5.11 \sigma_Z$ 

re;

5.12 Un Dif

5.13 Mo

are

5.14 Mor

reca

bet*u* 

5.15 Eff.

rive.

5.16 Eff.

 $n_{V_{f_{i}}}$ 

6.1 Con

5.5	The difference between vertices in events where more than one is
	found, for all slices of the Triple Differential
5.6	Variables used in the calculation of the effect of vertex resolution 112
5.7	Fractional jet energy resolutions for the first two slices
5.8	Fractional jet energy resolutions for two forward slices
5.9	Same Side and Opposite side resolutions overlaid
5.10	Effective vertex position resolution for all slices
5.11	$\sigma_Z$ extracted from MC data shown together with input vertex position
	resolution distribution
5.12	Unsmearing correction factors and errors for all slices of the Triple
	Differential
5.13	Monte Carlo derived effect of vertex smearing if only jet $E_T$ or jet $\eta$
	are recalculated
5.14	Monte Carlo derived effect of vertex smearing if jet $E_T$ and jet $\eta$ are
	recalculated, with different assumptions regarding the correlations
	between these variables
5.15	Effective vertex position resolution correction factors and errors de-
	rived from three Monte Carlo samples for slices 1 and 2
5.16	Effective vertex position resolution correction factors and errors de-
	rived from three Monte Carlo samples for slices 3 and 4
6.1	Components of the error for slices 1 and 2

6.2 C

6.3 T

μ

μ

 $\mu$ 

6.4 T

6.5 Ti

6.6 Th

μ =

6.7 Th

μ =

6.8 The

 $\mu =$ 

6.9 The

 $\mu =$ 

6.10 The

 $\mu =$ 

6.11 The

 $\mu =$ 

6.12 The

 $\mu \simeq$ 

6.2	Components of the error for slices 3 and 4
6.3	The fully corrected triple differential compared to NLO Jetrad, CTEQ3M,
	$\mu = \frac{1}{2}E$ for slices 1 and 2
6.4	The fully corrected triple differential compared to NLO Jetrad, CTEQ3M,
	$\mu = \frac{1}{2}E$ for slices 1 and 2, (data - theory)/theory
6.5	The fully corrected triple differential compared to NLO Jetrad, CTEQ3M,
	$\mu = \frac{1}{2}E$ for slices 3 and 4
6.6	The fully corrected triple differential compared to NLO Jetrad, CTEQ3M,
	$\mu = \frac{1}{2}E$ for slices 3 and 4, (data - theory)/theory
6.7	The fully corrected triple differential compared to NLO Jetrad, CTEQ4M,
	$\mu = \frac{1}{2}E$ for slices 1 and 2, (data - theory)/theory
6.8	The fully corrected triple differential compared to NLO Jetrad, CTEQ4M,
	$\mu = \frac{1}{2}E$ for slices 3 and 4, (data - theory)/theory
6.9	The fully corrected triple differential compared to NLO Jetrad, CTEQ4HJ,
	$\mu = \frac{1}{2}E$ for slices 1 and 2, (data - theory)/theory
6.10	The fully corrected triple differential compared to NLO Jetrad, CTEQ4HJ,
	$\mu = \frac{1}{2}E$ for slices 3 and 4, (data - theory)/theory
6.11	The fully corrected triple differential compared to NLO Jetrad, MRST,
	$\mu = \frac{1}{2}E$ for slices 1 and 2, (data - theory)/theory
6.12	The fully corrected triple differential compared to NLO Jetrad, MRST,
	$\mu = \frac{1}{2}E$ for slices 3 and 4, (data - theory)/theory

6.13

6.14

6.15 T

μ

6.16 T

 $\mu$ 

6.17 T

CO

6.18 Cc

Ca

6.19 The cor

A.1 Mon

A.2 Mor.

6.13	The fully corrected triple differential compared to NLO Jetrad, MRSTg <sup>†</sup> ,
	$\mu = \frac{1}{2}E$ for slices 1 and 2, (data - theory)/theory
6.14	The fully corrected triple differential compared to NLO Jetrad, MRSTg $\uparrow$ ,
	$\mu = \frac{1}{2}E$ for slices 3 and 4, (data - theory)/theory
6.15	The fully corrected triple differential compared to NLO Jetrad, MRSTg $\downarrow$ ,
	$\mu = \frac{1}{2}E$ for slices 1 and 2, (data - theory)/theory
6.16	The fully corrected triple differential compared to NLO Jetrad, MRSTg $\downarrow$ ,
	$\mu = \frac{1}{2}E$ for slices 3 and 4, (data - theory)/theory
6.17	The correlation matrix for errors not associated with the energy scale
	correction
6.18	Comparison of energy scale errors from data and from the toy Monte
	Carlo
6.19	The correlation matrix for errors associated with the energy scale
	correction
A.1	Monte Carlo closure of the di-jet asymmetry method
۸ ၁	Monte Carlo closure measurement with an input vertex resolution 160

#### About th

Gian G. D sey, a New N.Y. where Physics in

### Computer

This analysi

gan State U

currently liv

perspective,
Challenge ru
data set was
of theoretica.

Open VMS v

Free Vms v

author at Be-

#### About the Author

Gian G. Di Loreto was born in Manhattan in 1969, he grew up in Ramsey, New Jersey, a New York City suburb. He attended the University of Rochester in Rochester, N.Y. where he studied Physics and Latin. After receiving a Bachelor's Degree in Physics in 1992, he left Rochester for the midwest, to continue studying at Michigan State University where he obtained a Master's degree in Physics in 1994. He currently lives in Chicago, Illinois.

#### Computer Support

This analysis employed a variety of computers and operating systems, for historical perspective, we include a short description. The data were processed on an SGI Challenge running Unix, with sixteen parallel processors. The size of the reduced data set was  $\approx 9$  gigabytes which was processed in  $\approx 5$  minutes. The generation of theoretical predictions employed a farm of DIGITAL Alpha processors running Open VMS with clock speeds from 90-200 MHz. This thesis was written using Lagrangian Pentium 300 MHz running Microsoft Windows NT 4.0, purchased by the author at Best Buy in Aurora, II.

For My Parents, Gretchen Rhoads and Giuseppe Di Loreto.

And for Nana.

# Cha

# Intro

This thesis

accelerator
specific to

Before getti

duction to 1

introduction

# 1.1 A

How do we e

 $u_{\rm something}$ 

own structu:

One asp.

questions al.

torical instac

## Chapter 1

### Introduction

This thesis is a study of data taken at the Fermilab Tevatron, a high energy particle accelerator located in Batavia, Illinois, a suburb of Chicago. The measurement is specific to a process common during the type of collisions that occur at Fermilab. Before getting into the details of the measurement, we present a very broad introduction to particle physics, and then to the specifics of high energy physics. The introduction is not meant for the scientist, it is for family and friends.

#### 1.1 A Brief History of Particle Physics

How do we define intelligent life? One place to start is the notion of self awareness. If something begins to wonder about the notion of itself, its surroundings, even its own structure, one could argue that the criteria for intelligence have been satisfied.

One aspect of understanding ourselves and our surroundings involves asking questions about from what are we and everything around us made. This first historical instance of this question is usually associated with the Greek civilization.

Two philoso called early atomic theo after which. word atom, in two. Cor over and ove the atom is granular or early as 1200 The notic years ago by in Latin by Natura, On 1 particle physi De Rerun 1800's which of the eleme: performed by to create or: elements and

he called, ti

involves assig

Two philosophies regarding the nature of matter were put forth: the first can be called early atomic theory and the second continuity theory. The assumption in atomic theory is that all matter can be divided in half a finite number of times, after which, the matter will be small enough that it can not be divided again. The word atom, in fact, is derived from the Greek word for a body which cannot be cut in two. Conversely, continuity theory asserts that matter can be divided in two, over and over again, without limit. As mentioned, the introduction of the idea of the atom is usually ascribed to the Greek civilization, however the concept of the granular or atomic nature of matter can be attributed to Indian philosophers as early as 1200 B.C.

The notion of the atom is, by now, universally accepted. It was put forth  $\sim 2400$  years ago by a Greek named Leucippus and his pupil Democritus, and put to verse in Latin by a Roman, Lucretius, in the first century B.C. in his work, *De Rerum Natura*, On the Nature of Things. It is in this proud tradition that elementary particle physics still tries to come to terms with the nature of matter today.

De Rerum Natura represented the status of knowledge of atomic theory until the 1800's which saw the advent of the notion of atomic weight and the periodic table of the elements. An English scientist, John Dalton, studied several experiments, performed by contemporary scientists, involving the combination of known elements to create other known elements. He was able to explain the mass of the initial elements and their relationship to the mass of the resultant elements with, what he called, the law of single and multiple proportions. One facet of this theory involves assigning an atomic weight to each of the elements. The atomic weight was

were comend of the atomic we the element

After the elements.

The question of the plum properties of the collision while looking gold target. It to look for he

the nucleus.

An alpha;

keep his stuef

which scarte

the atom in 1

empirically determined by measuring the mass of a system before and after elements were combined; it appeared to be consistent for each known element. Towards the end of the nineteenth century Dmitri Mendeleev tabulated the known elements, their atomic weights, and their chemical and physical properties in the *periodic table of the elements*. This table implies that atoms of different elements have some similar characteristics; that perhaps different elements are made up of the same thing.

After the advent of the periodic table and the tabulation of all the different known elements, it was thought that the question posed years before had been answered. The question now was, what is the nature of the atom? One model, usually called the plum pudding model, put forth by J.J. Thomson, asserted that the atom was a homogeneous blob of positive charge, with negatively charged electrons embedded in it. The road to debunking this model began when an New Zealander scientist named Ernest Rutherford, who was scattering alpha particles<sup>†</sup> from various thin films of heavy metals, discovered the nuclear structure of the atom. Scattering a charged object off of a target and observing the angular distribution of the projectile after the collision, is a way to learn about the distribution of charges within the target. While looking at small angle scattering of positively charged alpha particles from a gold target, Rutherford's colleague, Hans Geiger, asked his student, Ernest Marsden to look for large angle scattering, which he did not expect to see, but hoped it would keep his student busy. They were very surprised to see there that were some particles which scattered at very large angles. This gave rise to the current nuclear model of the atom in which the positive charge is concentrated in the middle of the atom, or the nucleus.

<sup>&</sup>lt;sup>†</sup>An alpha particle is another name for a helium nucleus.

The radiation be bent that make known p

of the at

The

tons and scrutiny.

proton and energy lev quantized.

chanics is a their interactiventieth certains.

a cat in a !.

supposes th.

in physics a

of states. In

in either one

light, in que

If one str

The electron was discovered in the late 1800's by J.J. Thomson who was studying radiation emitted by heated filaments. He discovered that these *cathode rays* could be bent by a magnetic field. He calculated the charge to mass ratio for the particles that made up the rays, and discovered that this ratio was not consistent with any known particles. He further asserted that the electron was a fundamental constituent of the atom.

The nuclear model of the atom has been refined within the last 100 years. The nucleus of an atom is now believed to be made up of smaller particles, called protons and neutrons. In particular, the element hydrogen has been the subject of some scrutiny. Hydrogen is the lightest and simplest of all elements, consisting of only one proton and one orbiting electron. By studying the hydrogen atom, specifically the energy levels of the orbiting electron, it became clear that these energy levels were quantized, which eventually lead to the study of quantum mechanics. Quantum mechanics is a completely different, non-classical theory which describes particles and their interactions and represented a new way of thinking for physicists in the early twentieth century. The dramatic difference in philosophy between classical thinking in physics and quantum theory involves a concept we'll define as the superposition of states. In pre-quantum mechanics times, a physical observable was thought to be in either one state, or in another. For example, light was either a particle or a wave, a cat in a box that you couldn't see was either alive or dead. Quantum physics supposes that an observable can exist simultaneously in any of its available states; light, in quantum mechanics, is both a particle and a wave.

If one strips away the electron from a hydrogen atom, only a proton is left. The

proton is many of t

### 1.2

It could be with the i discovery physicists as describe duality prea better un

Positive cha nucleus toge

In an at

just as it wa quantized.

looked liked

problems w:

with the ni.

measuremer

After a  $\tau$ 

modern pari This force

proton is a fundamental unit of matter; we will see that it contains the answer to many of the modern physicist's questions.

#### 1.2 Modern Particle Physics

It could be argued that the beginning of modern particle physics was contemporary with the introduction of the *photon* and the advent of quantum mechanics. The discovery of the photon came in the beginning of the nineteenth century while physicists were studying electro-magnetic radiation from hot objects. The photon, as described by quantum mechanics, behaves as both a particle and a wave. This *duality* presents a conceptual challenge to the student, but provides scientists with a better understanding of matter and the forces acting on it.

In an attempt to explain how the nucleus of an atom stays together when only positive charge exists there, Yukawa proposed that there is a force that holds the nucleus together<sup>‡</sup>. This field which defines this force was proposed to be quantized, just as it was (and is) believed that the electromagnetic and gravitational fields are quantized. Yukawa called the mediator of this field the *meson*. Particles which looked liked mesons were discovered in cosmic rays in 1937, but there were some problems with the model. The particles discovered in the cosmic rays didn't interact with the nucleus strongly enough to be the mediator Yukawa predicted, and the measurements indicated that there were many mesons.

After a watershed of particle discoveries in the middle of the twentieth century, modern particle physics was in an uncertain state. There were simply too many

<sup>&</sup>lt;sup>‡</sup>This force has come to be called the strong force.

particles
blocks of
In 19
cles into
underlyi
particles
now app

#### 1.2.1

and that

The notion read this.

back against level, you may finger a up my hand when particle the nature of all pulled to your refrictories that the latest to your refrictories that the your refrictories that the latest to your refrictories that the your refrictories that the latest the latest the your refrictories that the latest the your refrictories that the your refrictories the your refrictories that the your refrictories the your refrictories that the your refrictories that the your refrictories the your refrictories the your refrictories that the your refrictories the your refrictories the your refrictories the your refrictories the y

forces are a

is usually rei

particles on record for any theory to describe them as the fundamental building blocks of matter. Particle physics needed a modern periodic table.

In 1961, Murray Gell-Mann proposed the *eightfold way* of arranging known particles into geometric tables. This method of cataloging seemed again to indicate some underlying structure. Murray Gell-Mann and G. Zweig proposed that all modern particles are made up of elementary constituents which Gell-Mann called quarks. It now appears that the quark model is consistent with all experimental observables, and that the proton is indeed made up of quarks.

#### **1.2.1** Forces

The notion of a force follows from a thought experiment involving touch. If, as you read this, you press your finger down on the table, you'll feel the table pressing back against your finger. If you begin to think about this interaction at the particle level, you may wonder, "what is happening to the atoms that make up my finger as my finger approaches the table?". "What does it mean for the particles that make up my hand to touch the particles that make up the table?" The answer is that when particles get close enough together, depending on the distance between and the nature of the particles, a force keeps them apart or pulls them together. We are all pulled towards the earth by gravity which acts on all particles. Magnets stick to your refrigerator due to the electromagnetic force. There are at least two other forces that have been measured: the strong and the weak force. In one theory, these forces are all thought to be different manifestations of the same thing. This theory is usually referred to as the Grand Unified Theory of Particle Physics.

The stational and inversely proton. To tational and inversely proton further appears they go close toget behavior with all force, the proton of the median force of the proton of the median force of the proton of the prot

Media
glue
phot

W<sup>2</sup>

Gravi

presented in

1.2.2 N

In the tradi-

The strong force describes, among other things, how quarks interact within the proton. The strong force has one distinctive difference from the more familiar gravitational and electromagnetic forces. The force due to gravity acting on two objects is inversely proportional to the square of the distance between them; it gets smaller the further apart the objects are. The strong force between objects actually *increases* as they get further apart. A consequence of this is that as the objects get very close together, the strong force gets quite weak; the ramifications of this *asymptotic behavior* will be discussed in Chapter 2.

All forces are mediated by a particle; in the more familiar electromagnetic case the mediator is a photon, a quantized particle of light. In the case of the strong force, the mediator is called the *gluon*, which like the photon, is massless. These different forces and their mediators along with some other interesting quantities are presented in Table 1.1.

Mediator	Charge $(e^-)$	Mass $(MeV/c^2)$	Lifetime	Force
gluon	0	0	$\infty$	strong
photon	0	0	$\infty$	electromagnetic
W±	±1	81,800	unknown	weak
$Z^0$	0	92,600	unknown	weak
Graviton	0	not observed	unknown	gravity

Table 1.1: Known forces and their mediators.

#### 1.2.2 Modern Experimental Particle Physics

In the tradition of Rutherford's gold foil experiment, modern particle physics usually involves colliding particles together, either with both particles moving or one moving

and one for can be sto a certain a cross so surface a in partic

when a considered to chapters.

of barns,

This t

cross secti shown to l

the proton.

## 1.2.3 Q

In electrody
electromag:
involving t)

QCD, the a

in electrody.

Triple Differer

and one fixed, in order to determine what makes up one, or both. These interactions can be studied by examining what is produced, and how often. The number of times a certain outcome occurs, divided by the number of interactions, is referred to as a cross section. This term refers to classical physics in which a cross section is the surface area of an object subject to collision. Following this analogy, cross sections in particle physics have units of area. Cross sections are usually presented in units of barns, where 1 barn =  $10^{-24}$  cm<sup>2</sup>.

This thesis concerns data taken at an experiment in which protons and antiprotons are collided at very high energies. One outcome of these collisions occurs
when a component of each proton is released and detected. These components are
referred to as quarks and gluons and will be discussed in detail in the following
chapters. The triple differential di-jet cross section refers to the measurement of
cross sections associated with this type of event§. The Triple Differential will be
shown to be sensitive to different theoretical predictions regarding the structure of
the proton. The goal of this analysis is a better understanding of proton structure.

#### 1.2.3 Quantum Chromodynamics

In electrodynamics, the property that a particle has in order to interact via the electromagnetic force has the familiar name of electric charge. In an interaction involving the strong force, hereafter referred to as quantum chromodynamics or QCD, the analog of electric charge is called color. While there are only two charges in electrodynamics, positive and negative, there are 3 colors in QCD, referred to

<sup>§</sup>From this point forward, the triple differential di-jet cross section will be referred to as the Triple Differential.

as red, feature

are equa

treatme

theories

Mode

introduce

as red, blue, and green. This nomenclature is essentially arbitrary, however, one feature of QCD is that all naturally occurring particles are colorless, that is there are equal distributions of red, green, and blue color within. For a more thorough treatment, the reader is directed to Chapter 2.

Modern particle physics requires large experimental apparati and complicated theories to produce and describe experimental results. The next three chapters introduce quantum chromodynamics, collider physics, and the DØ detector.

# Cha

## Qua

We presen

ics.

Quantu

present her

here is avai

will endeave

QCD  $_{\rm is}$ 

describe ho

quarks and

electromag:

aspects of t

simple and

electrody:16

In this,

## Chapter 2

### Quantum Chromodynamics

We present here an introduction; a pedestrian overview of quantum chromodynamics.

Quantum chromodynamics, or QCD, is a very complicated subject; we will present here an experimentalist's overview of the theory. The information presented here is available in much more detail in any of many references[1, 2, 3] however, we will endeavor to present QCD in a slightly distilled form.

QCD is a theory that describes how elementary particles interact. QCD doesn't describe how all particles interact, only particles that interact strongly such as quarks and gluons. Other particles, such as electrons, don't interact strongly, but electromagnetically and are described by quantum electrodynamics or QED. Many aspects of these two theories are very similar; QED has the advantage that it is simple and more familiar. The student can enlist his understanding of classical electrodynamics and QED to help him understand QCD.

In this chapter, we introduce some techniques in QCD and currently available

Monte Carlo event generators, and we motivate the measurement of the Triple Differential.

#### 2.1 The Golden Rule

If two particles come in some proximity to each other, their differential cross section, that is their differential interaction *area* can be described by

$$d\sigma = \frac{2\pi}{\hbar} |M|^2 \times \text{(phase space)}.$$
 (2.1)

In Equation 2.1,  $\hbar$  is a constant, and M is the amplitude, or matrix element for the interaction. The amplitude contains all the dynamical information. It tells us, for instance, what happens when a quark of type i interacts with a quark of type j. Phase space refers to all of the kinematic information. For example, the relative masses and momenta of the initial and final state particles and how likely it is for one kind of initial state particle to produce some final state particle. A useful example of this follows from mass considerations: it is more likely for a heavy particle to produce two light ones, than the other way around; the phase space term accounts for this. The cross section is differential in that in order to obtain the total cross section, one must integrate over all phase space and sum over all initial and final state particles. QCD manifests itself in the amplitude; the rest of the golden rule is relatively easy to calculate. The amplitude tells us what to expect when two strongly interacting particles hit each other; theorists need to flex all their muscles to calculate M.

is presen

that is unic

by the stron

two up qua

state of a

electron ar.

the proton

Quarks a

#### 2.1.1 Calculating Matrix Elements

The first thing we need in order to proceed with the calculation of the amplitude of two (or more) quarks or gluons<sup>†</sup> interacting is a cast of characters; the list of quarks is presented in Table 2.1.

Name	Electric Charge $(e^-)$	Mass $(MeV/c^2)$
down	-1/3	7.5
up	+2/3	4.2
strange	-1/3	150
charm	2/3	1100
bottom	-1/3	4200
top	+2/3	180,000

Table 2.1: Quarks: masses and charges.

All of the quarks have been observed experimentally. The top quark was the most elusive, it was discovered in 1995 at the Fermilab Tevatron[5, 6].

Now that we have a list of partons to consider we need to think about where these partons come from. We can see from Table 2.1 that the quarks have fractional charge which is something we haven't seen before, this is indicative of a feature of partons that is unique to them: partons do not exist alone. They only exist, held together by the strong force, inside other particles. For example, a proton is a bound state of two up quarks and a down quark in the same sense as the hydrogen atom is a bound state of a proton and an electron. However, in the case of the hydrogen atom, the electron and proton can be liberated and exist alone, the quarks cannot exist outside the proton. However, at high enough energies and at very small distance scales, the

<sup>&</sup>lt;sup>†</sup>Quarks and gluons are collectively called partons.

partons can interact as if they are independent. This concept is called *asymptotic* freedom, that is, the interacting partons act free if they are asymptotically close together.

#### 2.1.2 Parton Distribution Functions

Another aspect of QCD theory involves the probability of finding a specific quark inside the proton. While we have said that a proton is made up of up and down quarks, it is true that there are also smaller amounts of other quarks within the proton. This is because in the proton, there are also gluons, which with some probability will split into pairs of quarks for a small amount of time. These quarks are called sea quarks and need to be considered in our calculations. Meanwhile, the quarks that make up the proton, the ups and downs, are called valence quarks and carry approximately half the momentum of a proton, while gluons and sea quarks carry the other half.

In addition to the type of quarks (up, down etc.<sup>‡</sup>), another quantity used to identify a particular parton in the proton is the fraction of the momentum of the proton that the parton carries. This parton momentum fraction is usually denoted simply by x. The number of each type of parton that exists in the proton is called a parton distribution function and is usually represented by  $f_a(x)$ , where a is the parton type and x is the momentum fraction. Parton distribution functions are not predictable by QCD theory but are essential ingredients to understanding the structure of the proton. They are, in fact, one of the unknowns in QCD theory that one can mea-

<sup>&</sup>lt;sup>‡</sup>This description of a quark is usually referred to as *flavor*.

SUF

set

The

wini

PeΓ

**w**e

par

sure by looking at proton-antiproton<sup>§</sup> collisions. In Figure 2.1, we include a current set of parton distribution functions from the CTEQ group. CTEQ (Coordinated Theoretical and Experimental QCD) is a group of theorists and experimentalists which provides parton distribution functions by fitting data from many different experiments around the world. In Figure 2.1, f(x) is the parton distribution function; we plot x \* f(x) as this more closely corresponds to the momentum fraction of the partons at each x value.

<sup>§</sup>An antiproton is the anti-matter counterpart of the proton; it has the same mass and opposite charge. Every particle has a corresponding anti-particle, it is customary to refer to a proton as p and an anti-proton as  $\bar{p}$ .

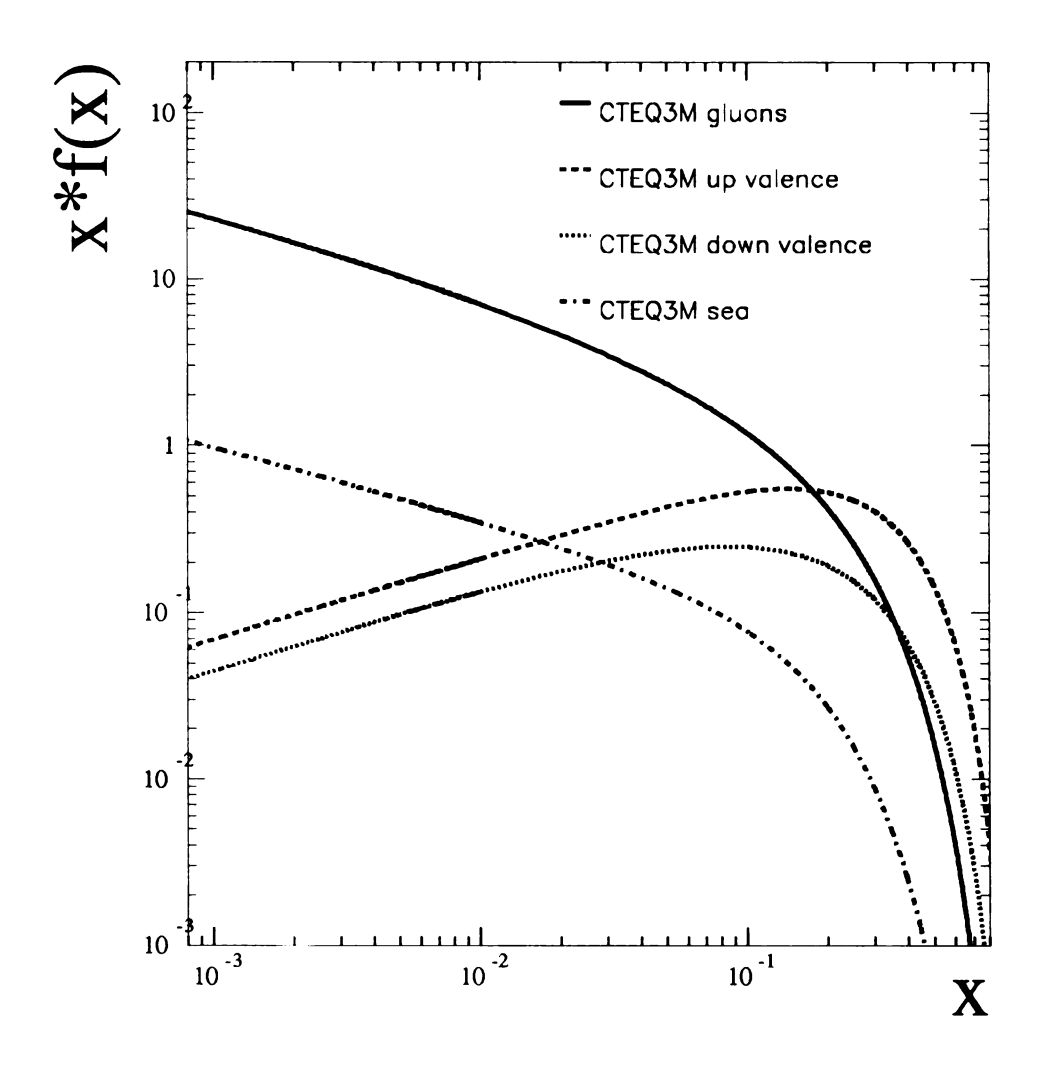


Figure 2.1: The CTEQ3M parton distribution function.

To be slightly more rigorous, a parton distribution function (pdf),  $f_a(x)$ , is actually better represented as  $f_a(x, Q^2)$ , where  $Q^2$  has units of energy and is the momentum exchanged during the partonic collision. The essence of this formalism is that the structure of the hadron depends on how closely you look at it. More energetic collisions allow better resolution such that what appears to be a single quark at  $Q = Q^0$  may be a pair of gluons at  $Q = Q^{q}$ . Fortunately if one measures  $f_a(x, (Q^0)^2)$ , a set of equations allows the calculation of  $f_a(x, Q^2)$  for any  $Q^2$ . This is referred to as Alterelli-Parisi (DGLAP) evolution.

We can see that the matrix element M is becoming very complicated. It involves what will happen when two partons interact, but it must also reflect how many of each type of parton is present. M can be broken into these two components thanks to a feature of QCD called factorization.

$$M_{i,j\to k,l} = f_i(x, Q^2, \mu_F) f_j(x, Q^2, \mu_F) \hat{\sigma}(i, j \to k, l)$$
 (2.2)

In Equation 2.2, f is the parton distribution function described above and  $\hat{\sigma}$  is called the hard scattering matrix element. It is the matrix element, or amplitude for the parton-parton interaction assuming the partons are free. That we can factor M this way reflects the fact that QCD is a factorizable theory. There is a price to pay for this advantage, however, in order to separate the components of M as in Equation 2.2, one must introduce a parameter, usually referred to as the factorization scale,  $\mu_F$ . This is an arbitrary parameter, it represents no physical quantity; furthermore, no physical oberservable can depend on it. It is usually assumed that  $\mu_F \sim Q^2$ .

This assumes  $Q^0 < Q'$ .

t in Fi  $\mathbf{W}_{i,j}^{1}$ 

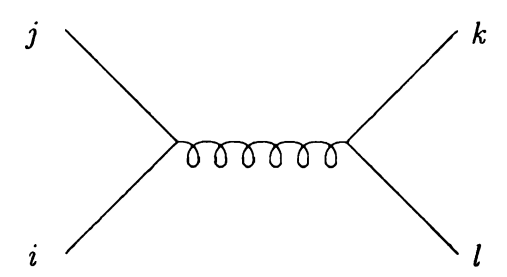


Figure 2.2: A simple diagram for parton-parton scattering

One can think of  $\mu_F$  as a cutoff beyond which partons act as free particles, in that it separates the pdf's from the hard scatter matrix element. We will see this is not the only scale necessary in QCD.

A graphical illustration of  $\hat{\sigma}$  is in order. In Figure 2.2, we present a diagram for parton of type i interacting with a parton of type j and producing partons k and l.

The diagram represents the matrix element described above  $(\hat{\sigma})$ . It is one of the simplest diagrams for quark-quark scattering. There are many other diagrams that contribute to the total hard scatter matrix element for quark-quark scattering. In the picture, the straight lines correspond to quarks and the curly line to a gluon. The rules of QCD dictate that two quarks can only couple to a gluon. At each vertex in the diagram, where there is one parton incoming and two outgoing, or vice versa, QCD can calculate the corresponding rate. This rate turns out to be proportional to a parameter called the *strong coupling constant*, denoted by  $\alpha_S$ . Each vertex introduces another factor of  $\alpha_S$ . The contributions from each of the two vertices in Figure 2.2 are added together according to

$$|M|^2 = |V_1|^2 + |V_2|^2$$

where  $|V_1|$  and  $|V_2|$  are the amplitudes for each of the two vertices. There are rules

for v
gaus
to p
the
calc
Figu

are a In

one (

of sma

calcula We hop

good ap

the case,

leading or

order  $\alpha_S^3$ .

for which partons can couple (interact) with which. These rules are derived from gauge theories. For example,  $|V_1|$  could be the amplitude for two quarks annihilating to produce a gluon; QCD can predict the rate for such an interaction. In fact, the diagram in Figure 2.2 is much more than a picture, it represents a complete calculation. There also are rules that govern the complete calculation pictured in Figure 2.2; these are called *Feynman rules*. The reader is again directed to the references[1, 2, 3] for more detail.

The diagram in Figure 2.2 is called a *leading order* diagram; it represents only one contribution to the total cross section from quark-antiquark scattering. There are actually an infinite number of diagrams for any given QCD process.

In calculus, a function can be represented by a Taylor series which is a series of smaller and smaller terms. A good approximation to the function can usually be obtained by only considering the first few terms. In QCD jet production, the calculation of all but the first one or two terms (diagrams) is prohibitively difficult. We hope, therefore, that the series is well behaved enough that this will provide a good approximation of the total matrix element. We will see that this in not always the case, and we'll discuss some of the tricks used to deal with this. In QCD jet production, the expansion is actually in terms of the strong coupling constant  $\alpha_S$ ; leading order calculations are of order  $\alpha_S^2$ , and next-to-leading order (NLO) are of order  $\alpha_S^3$ .

2

c

d

p:

a 1

dias

An

diagram

This co

It app

On So that

lan the co

### 2.1.3 Radiative, Loop Corrections and Next to Leading Order

The total matrix element for two quark to two quark scattering is a sum of many contributions of which only one is illustrated in Figure 2.2. Just as in QED, where an accelerating electron can radiate a photon, a quark in QCD can radiate a gluon. This radiation gives rise to an additional diagram called a radiative correction. The diagram in Figure 2.2 is a leading order diagram; if we were to include one of the possible radiated gluons, we would introduce another factor of  $\alpha_s$ . The result is a next to leading order (NLO) calculation. Currently, theorists are only able to calculate matrix elements to next to leading order. One of the next to leading order diagrams for quark-antiquark annihilation is pictured below in Figure 2.3.

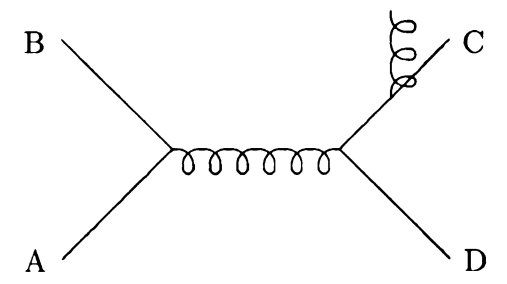


Figure 2.3: An example of a radiative correction.

Another type of correction to a leading order diagram is called a loop correction.

This correction accounts for radiated gluons which are quickly re-absorbed. Two diagrams for loop corrections appear in Figures 2.4.

It appears that each of the loop corrections contributes two additional factors of  $\alpha_s$ , so that the loop diagrams are actually next-to-next-to leading order. This is in fact the case, but we will see that these diagrams, when combined with the leading

B \

û**r**de

0.ce

2.1

Eac for (

01 t]

pr<sub>00</sub>

û. 0

tl<sub>iät</sub>

Corre

It

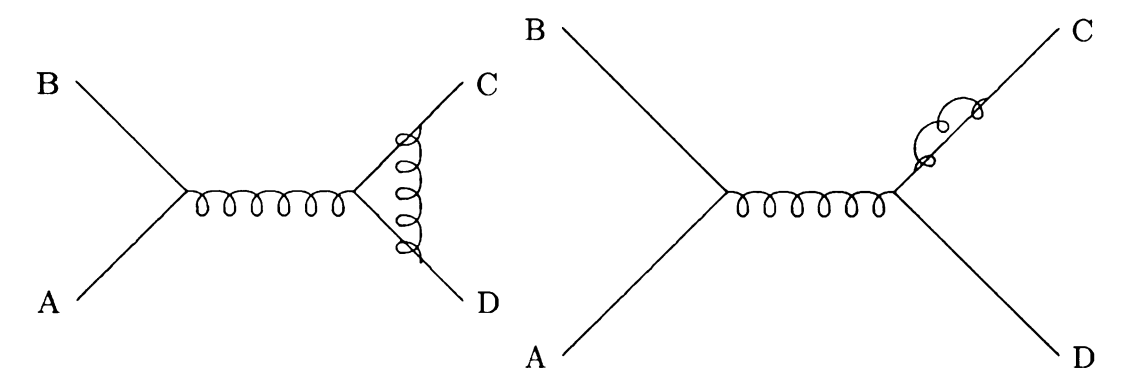


Figure 2.4: Two examples of loop corrections.

order diagrams to produce a full matrix element contribute to the next to leading order prediction.

#### 2.1.4 Total Next to Leading Order Predictions

Each of the diagrams in Figures 2.2-2.4 represents a contribution to the amplitude for quark-antiquark annihilation. We have seen that at NLO there are either two or three final state partons. In order to calculate the total NLO amplitude for this process we need to sum up all the possible diagrams and drop all terms of order  $\alpha_s^4$  or higher. The sum proceeds as follows: assume we have only two diagrams that contribute to the NLO amplitude, the leading order diagram,  $D_1$ , and the loop correction discussed above,  $D_2$ . The total amplitude squared is defined by:

$$|M|^2 = (|D_1| + |D_2|)^2 = |D_1|^2 + |D_2|^2 + 2D_1 \times D_2$$
 (2.3)

In Equation 2.3,  $D_1$  is proportional to  $\alpha_s^2$ ,  $D_2$  is proportional to  $\alpha_s^4$ , therefore

 $\sqrt{D_1}$ 

in thi

while

inch

2.6.

2

 $\sqrt{(D_1 \times D_2)}$  is proportional to  $\alpha_s^3$ . This cross term is important to consider. Indeed, in this special case, the loop diagram contributes to the cross term to the order  $\alpha_s^3$ , while by itself it does not make it into the NLO calculation.

All diagrams, to leading order, corresponding to two initial state partons are included in Figure 2.5. Some next-to-leading order diagrams are included in Figure 2.6.

#### 2.1.5 Loop Corrections and Renormalization

The loop correction introduces one of the more difficult aspects of QCD to digest. Unlike the photon, the gluon can interact with itself. This self correction introduces divergences into the calculations. Although the specific nature of these divergences are beyond the scope of this discussion, we can agree that if QCD is to describe an interaction in nature, it should predict only physically allowable results. To deal with this, the theory is renormalized. This involves introducing a scale which cancels the divergences introduced by the gluon self-correction. It essentially involves cutting off the integrations in the calculations at some distance, defined by the renormalization scale,  $\mu_R$ . Like  $\mu_F$ ,  $\mu_R$  is expected to be proportional to the momentum exchange. In the scheme used in this analysis and corresponding theories,  $\mu_F = \mu_R$ . Also, like  $\mu_F$ ,  $\mu_R$  is an arbitrary parameter; any observable quantity cannot depend on the renormalization scale.

#### 2.2 NLO QCD and the Triple Differential

The previous examples are some of the contributions to two and three final state parton production from proton-antiproton collisions. We have not gone into detail regarding the actual calculations of the individual matrix elements; the reader is again directed to the references. However, even without a rigorous derivation we can see some of the considerations necessary to predict at NLO how often we can expect multi-parton final states in proton-antiproton collisions. We will now discuss how final state partons evolve after the interaction to produce final state objects. These final state objects are referred to as *jets* and are what are actually measured during the experimental cross section calculation described in this thesis. The Triple Differential is a measurement of a two jet final state cross section. The measurement is sensitive to the partonic cross section; it is a test of our understanding of proton structure.

#### 2.2.1 Hadronization and Jets

As aforementioned, one cannot observe free partons. Within a very short time after they are produced, the final state partons join up with other asymptotically free particles to form stable hadrons. This process is called *hadronization*. There are only empirical models for hadronization, it cannot currently be calculated explicitly. In a detector, one can observe a collection of highly collimated particles coming from a proton-antiproton collision. One assumes that all these stable particles came from a single parton. This collection of stable final state particles is called a *jet*, and is what is actually measured while studying QCD in a  $p\bar{p}$  experiment. Some different

methods for defining jets is the subject of a later discussion.

In Figure 2.5, we include all diagrams for two or more jet production at leading order and in Figure 2.6, we include some diagrams at NLO. Additionally, a summary of  $p\bar{p}$  interactions involving jet production appears in Figure 2.7.

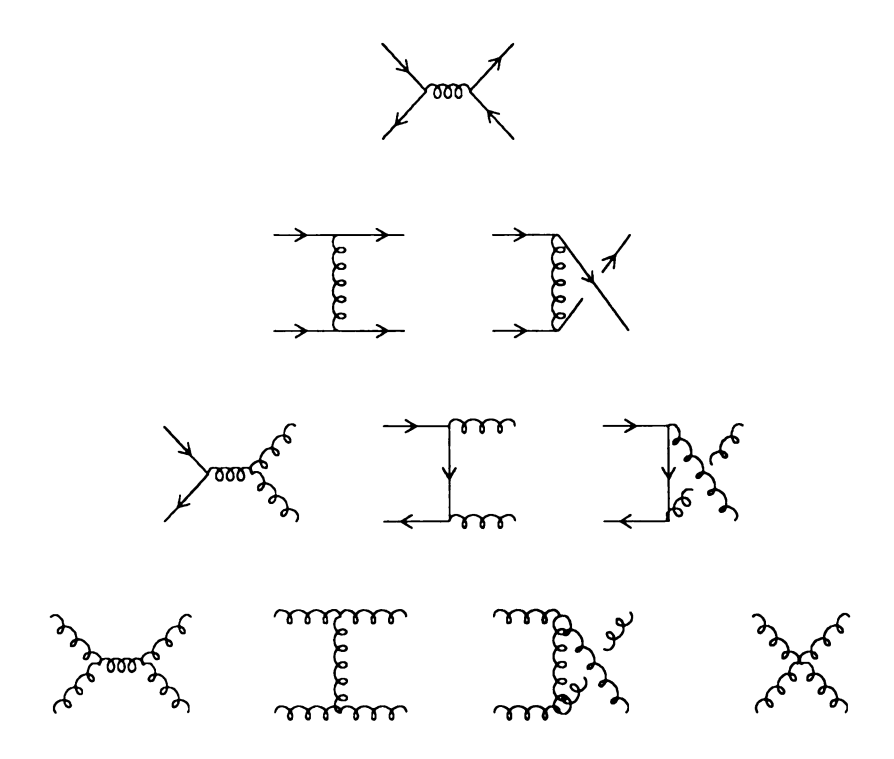


Figure 2.5: Leading order diagrams for di-jet production.

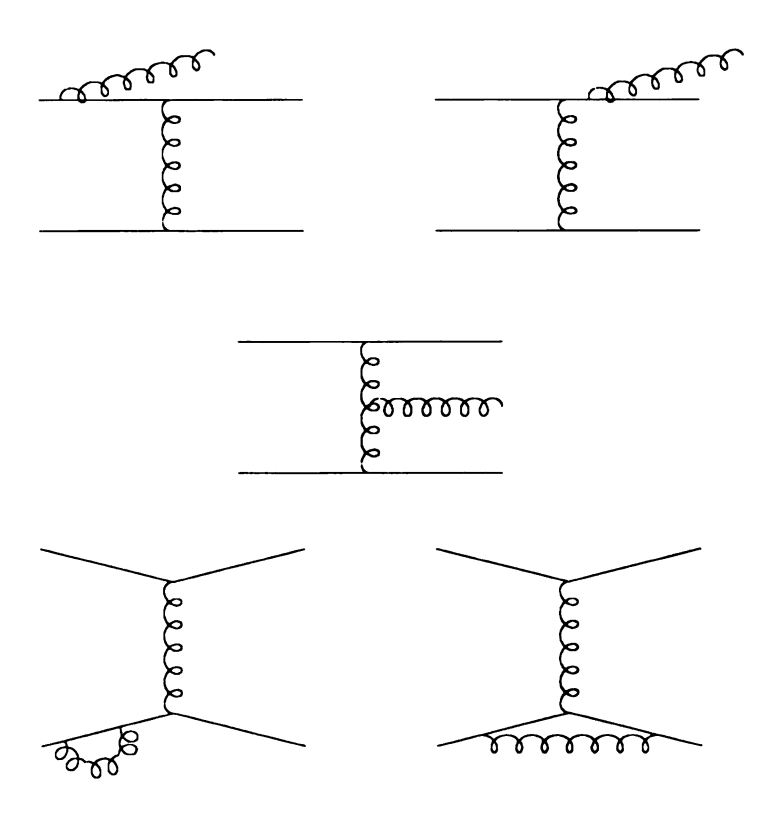


Figure 2.6: Higher order diagrams for di-jet production.

In Figure 2.7,  $h_1$  and  $h_2$  are the proton and the antiproton which contain partons a and b with momentum fractions  $x_1$  and  $x_2$  respectively. Additionally, the probabilities of finding partons a and b in the proton are described by  $f(x_1)$  and  $f(x_2)$ , the parton distribution functions. The center of the diagram represents the partonic interaction,  $\hat{\sigma}$ , which depends on the strong coupling constant,  $\alpha_s$ , and the momentum exchanged during the interaction,  $Q^2$ . Finally, the final state partons c and d form a hadron  $h_3$  and a jet respectively. In this example, parton c hadronizes immediately, while parton d showers into many partons, each of which will eventually hadronize as well.  $D_{h\leftarrow k}(z)$  is a hadronization model for parton cto form hadron  $h_3$ . Like hadronization, the development of parton showers is not a process one can measure. Different models for parton showering currently exist, among them string fragmentation, which assumes a color connection between two partons. When the distance between the partons becomes large enough, two more partons are created from the vacuum. In another model, independent fragmentation, single quarks fragment into a  $q\bar{q}_1$  pair and a remainder quark  $q_1$ . These new quarks fragment as well until they no longer have enough energy to create quarks from the vacuum.

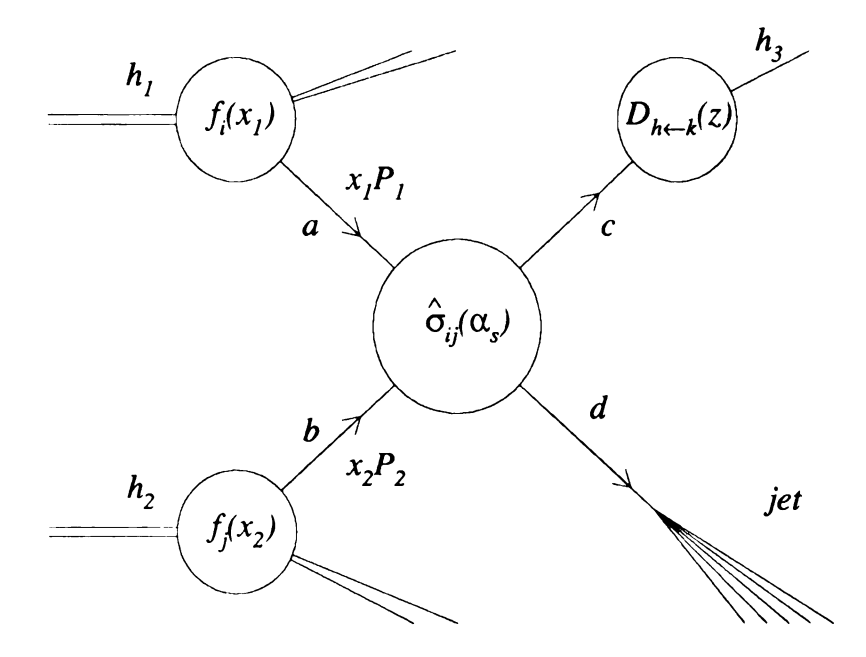


Figure 2.7: Summary of contributions to QCD jet production.

me cor

at:

Dif

2.

Bet

is :

exc

ene Th

bea

In E

thát

The Triple Differential measures how often different configurations of two or more jet final states are observed from  $p\bar{p}$  collisions. The assumption is that this corresponds to two or more final state partons. Armed with the previous considerations of NLO QCD and parton distribution functions, one can expect the Triple Differential to be sensitive to parton distribution functions as well the accuracy of the NLO matrix element calculations.

#### 2.3 The Triple Differential Di-Jet Cross Section

Before introducing the explicit form of the theoretical cross section, it is necessary to introduce some of the variables used in jet physics. The jet *rapidity*, defined as

$$y = \frac{1}{2}log(\frac{E - P_z}{E + P_z})$$

is used to describe the *position* of the jet. The rapidity is used because it is invariant, except for an additive factor, under Lorentz transformations along the z-axis. The energy of the jet is defined as E, however the transverse energy,  $E_T = E\sin(\theta)$ , where  $\theta$  is the polar angle between the particle's trajectory and the direction of the beam, is usually used as it is also Lorentz invariant.

Explicitly, the lowest order Triple Differential takes the form:

$$\frac{\partial^3 \sigma}{\partial E_T \partial y_1 \partial y_2} = \frac{1}{8\pi} \sum_{ij} x_1 f_i(x_1, \mu_F) x_2 f_i(x_2, \mu_F) \frac{\alpha_s^2(\mu_R)}{E_T^3} \frac{|M_{ij}(y^*)|^2}{\cosh^4 y^*}.$$
 (2.4)

In Equation 2.4, y is the jet rapidity and  $y^* = \frac{y_1 - y_2}{2}$ . We can see from Equation 2.4 that the Triple Differential is sensitive to both the matrix elements  $(M_{ij})$  and the

y bin	Topology	Slice
0.0 - 0.5	SS	1
0.0 - 0.5	OS	1
0.5 - 1.0	SS	2
0.5 - 1.0	OS	2
1.0 - 1.5	SS	3
1.0 - 1.5	OS	3
1.5 - 2.0	SS	4
1.5 - 2.0	OS	4

Table 2.2: Binning of the Triple Differential.

parton distribution functions<sup>†</sup>.

#### 2.3.1 Choice of Variables

The Triple Differential cross section as represented in Equation 2.4 is a four dimensional object. In order to measure it, it is necessary to decide which variables to fix and which to plot. This analysis defines the Triple Differential by fixing the angles of the two jets and casting their  $E_T$  distributions. Both jets are restricted to be within the same rapidity bin; we define 4 bins between y = 0 and |y| = 2.0. We also distinguish separately events in which both jets are on the same side of the detector (SS) and both jets are on opposite sides of the detector (OS). To elaborate, in the same side topology,  $y_1 \approx y_2$  while for the opposite side case  $y_1 \approx -y_2$ . In this scheme there are eight cross sections<sup>‡</sup>, they are listed in Table 2.2.

<sup>&</sup>lt;sup>†</sup>In Equation 2.4,  $f_i(x_1, \mu_F)$ ,  $i = (g, q, \bar{q})$ , is the parton distribution function evaluated at factorization scale  $\mu_F$ .

<sup>&</sup>lt;sup>‡</sup>In the proceeding chapters, an individual rapidity bin is referred to as a *slice*.

#### **2.3.2** $x_1, x_2$ and the Triple Differential

The Triple Differential measurement described here depends on variables specific to jets. A more illuminating measurement might be the number of events involving a parton of momentum fraction  $x_1$  interacting with a parton of momentum fraction  $x_2$  as a function of the momentum exchanged between them. This differential cross section would be expressed as

$$\frac{\partial^3 \sigma}{\partial x_1 \partial x_2 \partial (Q^2)} \tag{2.5}$$

where  $Q^2$  is the partonic momentum exchange. This representation has the advantage that it is in the variables of partons distribution functions. Once the measurement is made, the corresponding PDF could essentially be read from the plot. However, the DØ detector doesn't measure parton momentum fractions; it is much easier to cast the cross section in variables we measure. Fortunately, the mapping from one space to the other is relatively straightforward, it takes the form

$$x_{1,2} = \sum_{njets} \frac{1}{\sqrt{s}} (e^{\pm y_1} + e^{\pm y_2}). \tag{2.6}$$

For our choice of cross sections,  $|y_1| \cong |y_2|$ , so we can easily transform our measurement of the Triple Differential to the more theoretical variables. For example, the SS cross section in the bin  $1.5 \leq |y| \leq 2.0$ , pictured schematically in Figure 2.9, involves a large x and a small x partonic interaction. In the case of opposite side cross sections, calculated at leading order,  $x_1 = x_2$ . This means each point on the x axis of the OS Triple Differential, maps to a point on the  $x_1, x_2$  plane. A representative opposite side cross section is also pictured schematically in Figure

2.9. B

calcula

these c

2.8: th

For

We ha

eciral

the fi

V

926

μŀ

T į 2.9. By solving<sup>§</sup> Equation 2.6 for all the slices considered in this analysis, one can calculate the region of x space covered by the Triple Differential. The results of these calculations appear in Table 2.3.

For further illustration of the x range covered by this analysis, we include Figure 2.8; the area in the  $x_1 - x_2$  plane covered our definition of the Triple Differential. We have calculated, for each of the 8 cross sections,  $x_1$  and  $x_2$  assuming two jets of equal  $E_T$ . We plot  $x_1$  and  $x_2$  for each of the cross sections, labeled accordingly in the figure.

When we discuss results in Chapter 6, we will be able to see which x regions we are probing and where in x space the theoretical predictions are capable of matching the experimental data.

y bin	Topology	$x_{min}$	$x_{max}$
0.0 - 0.5	SS	0.05	0.57
0.0 - 0.5	OS	0.06	0.45
0.5 - 1.0	SS	0.03	0.70
0.5 - 1.0	OS	0.08	0.43
1.0 - 1.5	SS	0.02	0.29
1.0 - 1.5	OS	0.13	0.54
1.5 - 2.0	SS	0.01	0.80
1.5 - 2.0	OS	0.19	0.52

Table 2.3: x space covered by the Triple Differential via Equation 2.6 assuming two jets of equal  $E_T$ .

<sup>§</sup>The calculations covered in this section are performed to leading order.

#### **Triple Differential X Coverage**

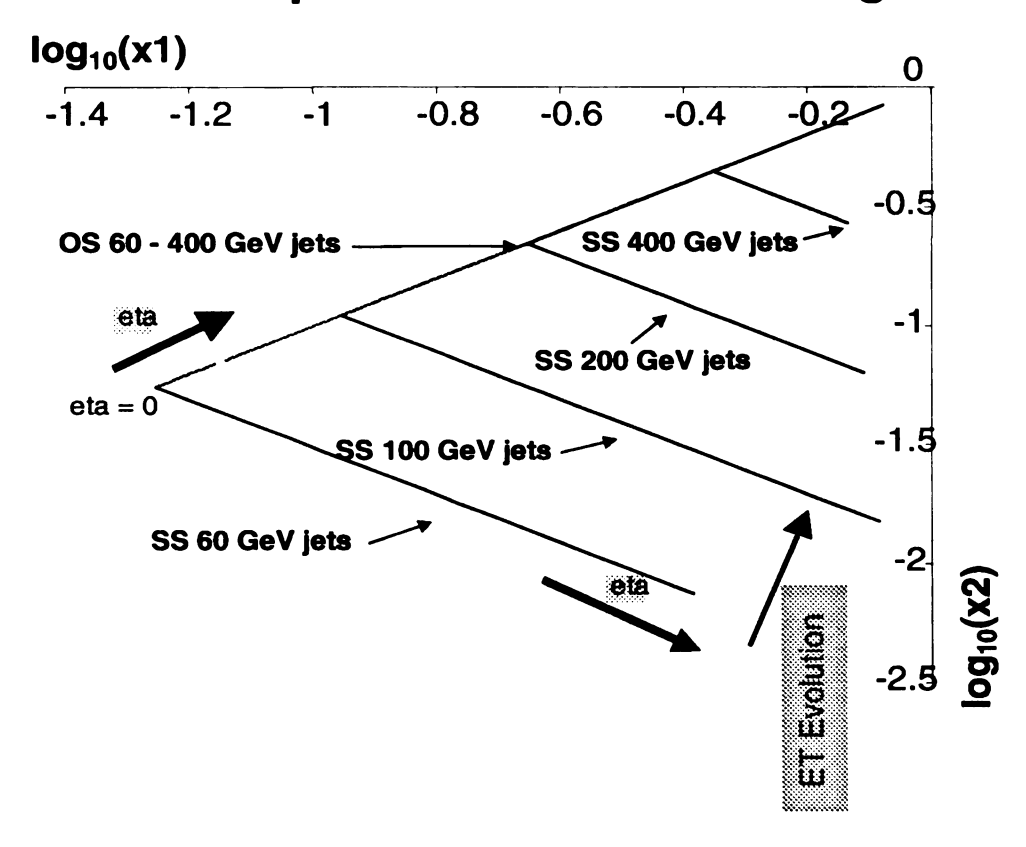
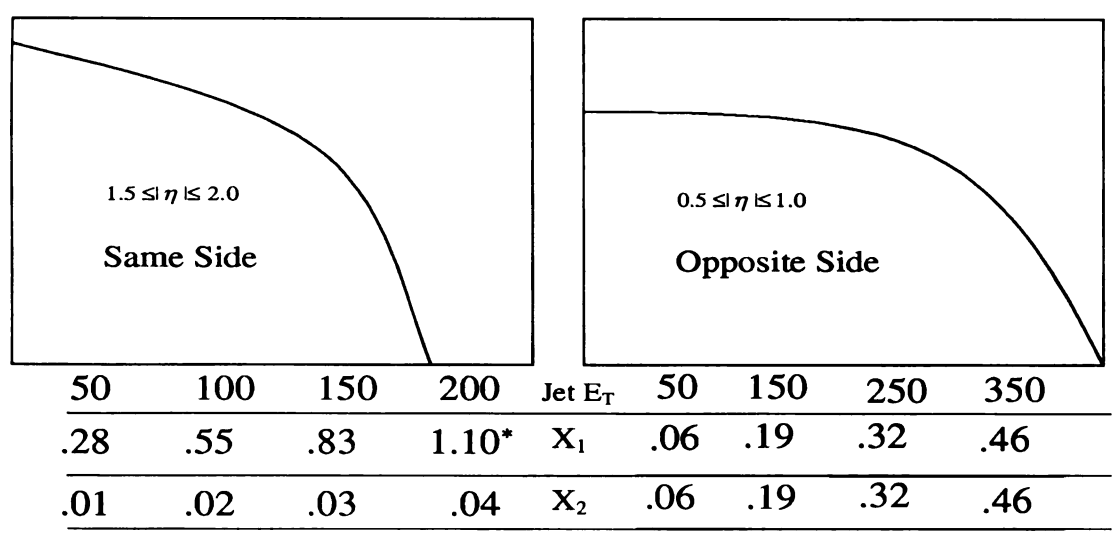


Figure 2.8: Graphical representation of x coverage of all slices and topologies of the Triple Differential.



<sup>\*</sup> not allowed

Figure 2.9: Representative slices of the Triple Differential and their x coverage. Notice the kinematic limit in the SS forward cross section at large  $E_T$ .

2.

Ti aş

2.

CI

Ję

dis

ďô

рa

Sta

to

2

H â١

fi ing

the

\**•** 

## 2.4 Implementation of QCD, Monte Carlo Predictions

The calculations discussed in this chapter are used with various Monte Carlo packages to produce predictions for the Triple Differential. Specifically, the packages used are named Jetrad[8] and Herwig[7] and are described below.

#### **2.4.1** Jetrad

Jetrad is a full next-to-leading order parton level Monte Carlo which produces a cross section including loop and radiative corrections. The user can input a parton distribution function as well as renormalization and factorization scales. Jetrad doesn't model any detector effects, additionally it assumes that each final state parton contributes all of its energy to a jet. In the event of a three parton final state, Jetrad uses a cone algorithm to decide whether or not to cluster partons together.

#### 2.4.2 Herwig

Herwig is an event generator rather than a NLO cross section calculation. It generates a leading order partonic interaction, but it contains initial state radiation and final state parton showers. It employs string fragmentation to model parton showering. Particles from Herwig output can be matched with test beam data to simulate their behavior in the DØ detector. Like Jetrad, Herwig can be adjusted based on

<sup>¶</sup>See Chapter 3 for discussions regarding jet definitions.

the re: ti to the user's desire for a particular parton distribution function and factorization and renormalization scale.

We will see the need for both of the Monte Carlos during the measurement of the Triple Differential.

Having discussed the theoretical motivation for the measurement, we move on to the experimental setup necessary to perform it.

#### Chapter 3

# The Tevatron, the DØ Detector and Jets

Now that there exists a motivation for observing jets, we'll describe how a jet is defined and produced. Before one can observe jets, one needs a mechanism for creating them, that is a device which produces energetic beams of particles directed to collide with each other. In this chapter, we introduce such a device as well as the DØ detector along with some general principles of jet physics.

#### 3.1 The Fermilab Tevatron

What is desired is a narrow beam of protons and antiprotons which collide in a well defined way. The Fermilab Tevatron is the largest and most energetic collider in the world today. It produces proton-antiproton collisions of center of mass energy  $\sqrt{s} = 1.8 TeV$ . These collisions are achieved by coordinating several different large and complicated accelerators together with many magnets, computers and people.

In order to achieve such energetic collisions, several separate accelerators are needed, each capable of taking particles from one energy to another. These machines, described below, work together like gears in a car to take the particles from E=0 to  $E=900\ GeV$ .

The layout of the Fermilab Tevatron is pictured in Figure 3.1. The components are listed in Table 3.1.

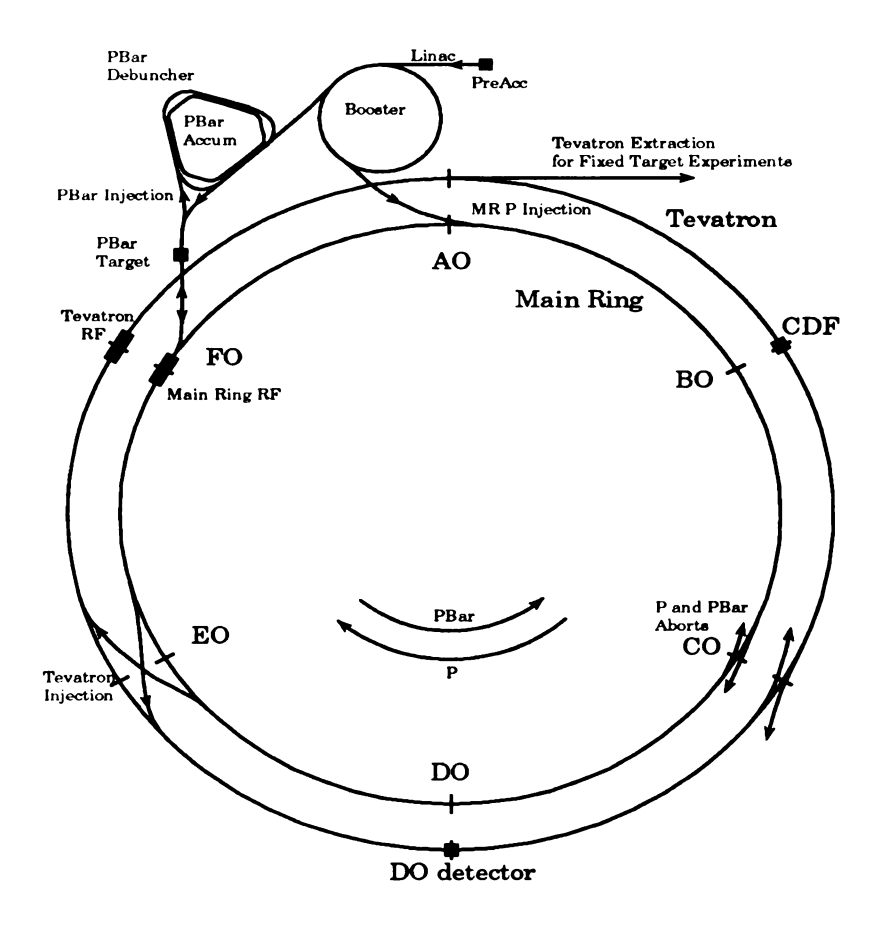


Figure 3.1: Overview or the Fermilab Tevatron.

The process starts in the Pre-Accelerator where hydrogen ions are produced from a surface-plasma magnetron. The ions are then accelerated to 750 KeV and injected into the linear accelerator called the *Linac*.

The Linac is constructed from five steel drift tubes of increasing length, with a

Name	Type	Beginning Energy (GeV)	Final Energy (GeV)
Pre-Accelerator	Linear	0	.00075
Linac	Linear	.00075	.4
Booster	Circular	.4	8
Main Ring	Circular	8	150
Tevatron	Circular	150	900

Table 3.1: Major components of the Fermilab Tevatron.

gap between them. An electric potential is applied carefully such that while the ions are in the gaps between the tubes, they are exposed to a negative potential so that they speed up. While they are in the steel tubes, they are protected from the field and they simply drift. A collection of focusing and de-focusing magnets keep the ions on a linear trajectory. The ions leave the Linac with an energy of 400 MeV.

After the Linac, the hydrogen ions have their electrons stripped as they pass through a carbon foil; what remains is a proton. These protons then pass into the Booster Synchrotron. The Booster is the first circular accelerator in the chain. The protons are bent into a roughly circular orbit and cavity resonators are used to increase the energy of the beam. The magnetic fields are increased as the energy increases to keep the proton beam, by now a beam of proton bunches, in the same circular path. The bunches leave the Booster as "kicker" magnets bend them out of their circular orbits and direct them into the next accelerator, the Main Ring.

The Main Ring lies directly over the Fermilab Tevatron, the final stage of the acceleration process. The Main Ring, like the Booster, is a synchrotron; it takes the proton bunches from 8 GeV to 150 GeV. With careful timing, the bunches are then injected into the Tevatron below.

The Tevatron is the world's highest energy superconducting accelerator. Like the Main Ring, the Tevatron is a synchrotron. The difference is in the strength of the magnetic fields the two machines need to produce. In order to bend and contain the high energy proton beams, the magnets must be very powerful, capable of producing very large magnetic fields. To accommodate this need, the wires which are wound to make up the magnets are cooled to  $\sim -450^{\circ}$  F by liquid helium. The Tevatron accelerates the proton bunches to their final energy of 900 GeV at which point they are traveling  $\sim .9999 \times$  the speed of light.

We have described thus far the acceleration of protons in the Fermilab Tevatron, however we recall that the Tevatron is a proton-antiproton collider so we'll need some place to get them from.

Antiprotons are produced by skimming some of the protons from the Main Ring and directing them towards a nickel<sup>†</sup> target. A shower of particles results, some of which are antiprotons. These antiprotons are directed into the  $\bar{p}$  Debuncher, an accelerator in the shape of a rounded triangle with three straight legs. During their time in the Debuncher, the antiprotons are collected into bunches with like momenta by a process known as stochastic cooling. They are then transferred to the Accumulator before being injected into the main ring, now moving in the opposite direction as the protons. Along with the protons, the antiprotons are transferred into the Tevatron and accelerated to 900 GeV. Additional information regarding the Fermilab Tevatron can be found in [4].

During collider operation, six p and six  $\bar{p}$  bunches occupy the Tevatron. Their

<sup>&</sup>lt;sup>†</sup>Other metals are sometimes used, but nickel is the most common.

orbits are slightly perturbed such that they collide at six distinct points in the ring. The DØ detector exists around one of these points. During the data taking for the data used in this analysis, collisions occurred with a frequency of  $(3.5\mu sec)^{-1}$  and ran for approximately 15 months<sup>‡</sup>. Most collisions involved only soft<sup>§</sup>, "uninteresting" collisions. The system for distinguishing these uninteresting interactions from the interesting ones is called a *trigger*. The trigger, the rest of the data taking software and hardware along with the DØ detector itself is described in the next section.

### 3.2 The DØ Detector

DØ is an all-purpose detector which is used for many different kinds of physics. It has excellent calorimetry, or measurement of hadronic particles, however, it has no central magnetic field and the Main Ring accelerator runs through the detector. These properties will present special challenges while interpreting data from the detector. The detector is large, even by particle physics standards; it weighs 5500 tons and stands over 40 feet high. The DØ detector is comprised of several different sub-detectors, each used for measuring a certain type of particle. We will introduce the device, concentrating on those detector sub-systems relevant to the Triple Differential. For detailed descriptions of any of the sub-systems, or the detector as a whole, the reader is directed to [13].

Before introducing the detector however, it is necessary to introduce the coordinate system used to define the physical space covered by the detector, shown in

<sup>&</sup>lt;sup>‡</sup>This period of data taking is referred to as Run 1B.

<sup>§</sup>Soft describes an interaction in which little momentum was transferred.

Figure 3.2. The three quantities most commonly used to define an object in the DØ detector are the particle's  $E_T$ , pseudo-rapidity, or  $\eta$ , and azimuth,  $\phi$ .  $\eta$  is defined by

$$\eta = -log(tan(rac{ heta}{2})).$$

 $\eta$  is used because in the high energy limit,  $\eta \sim y$ , where y is the rapidity, introduced in Chapter 2,

$$y = \frac{1}{2}log(\frac{E - P_z}{E + P_z}).$$

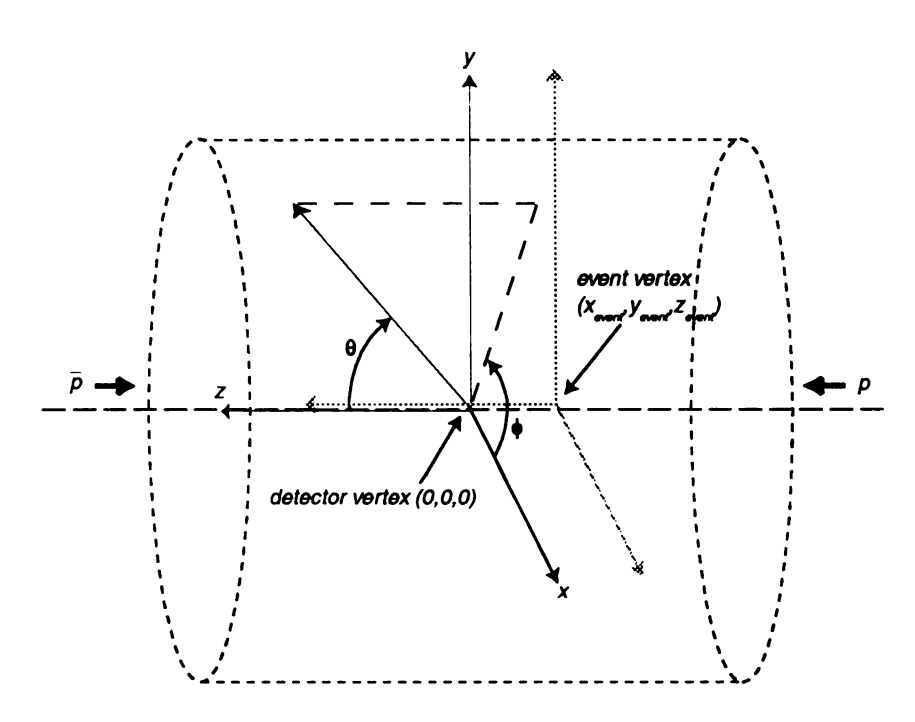


Figure 3.2: Coordinates used in the DØ detector, the event vertex is at the  $p\bar{p}$  interaction point, which can be different from Z=0.

### 3.2.1 Tracking

Charged particle tracking is accomplished at DØ through the use of three detectors, a central tracking chamber and two forward tracking chambers. A track, the trajectory of a charged particle, is made up of many individual hits in one of the tracking detectors. A hit occurs when a charged particle ionizes the gas in a tracking chamber and produces a shower of charge.

### 3.2.2 The DØ Muon System

It is necessary to distinguish particles from the interaction point from particles that enter the detector from elsewhere. The largest component of this sort of contamination is particles from cosmic showers which are primarily made up of muons. Additionally, good measurement of muons that result from  $p\bar{p}$  interactions is also useful. The DØ muon system provides information about muon position and momentum. The muon system employs a toroidal magnet to deflect muons; the muon position is measured before and after the bend, to determine the particle momentum.

### 3.2.3 Level Zero

The least complicated detector at DØ is the Level Zero detector. This detector is used to provide crude information about the vertex position of a  $p\bar{p}$  interaction. Furthermore, it is used to determine if an interaction occurred at all.

The beams are focused at DØ in an effort to have them collide at the center of the detector. However, it is possible that the interactions occur away from Z = 0,

sometimes as far as  $Z=\pm 100cm$ . In fact, the events in this analysis have a vertex distribution of width  $\sigma_Z\approx 30cm$ . The Level Zero detector employs two scintillating hodoscopes surrounding the beampipe, on either side (north and south) of the interaction point. If the remnant from the  $p\bar{p}$  interaction, that is the proton (or  $\bar{p}$ ) fragment, hits both the north and south Level Zero concurrently, it indicates that an inelastic interaction took place. Additionally, by looking at the timing information from the north and south detectors, it can be roughly determined where the interaction took place. A Level Zero hit is a condition required on many types of event selection at DØ as will be discussed later. Level Zero can is also used to estimate the intensity of the beam, called the Luminosity, the number of particles in the beam, per unit area, per unit time.

### 3.2.4 Luminosity Calculation

Luminosity ( $\mathcal{L}$ ) at DØ is measured in two incarnations, instantaneous and integrated. Instantaneous refers to the number of  $p\bar{p}$  crossings per second. Integrated is, as the name suggests, integrated over time. The luminosity calculation hinges on a quantity which represents the probability of a  $p\bar{p}$  interaction and the probability of the DØ detector to observe the interaction. The quantity is referred to as the luminosity monitor constant. Expressed as  $\sigma_{L\beta}$ , it is calculated by combining measurements of the world average  $p\bar{p}$  cross section with measurements of the acceptance of the DØ Level Zero detector. The total  $p\bar{p}$  cross section is determined by combining information from many different experiments. This number is combined with a Monte Carlo

<sup>¶</sup>An inelastic collision is one where the proton and/or  $\bar{p}$  breaks up.

study which determines the acceptance of the DØ detector; that is, what fraction of the total  $p\bar{p}$  cross section is visible to the DØ detector. The luminosity monitor constant for the data in this analysis was determined as  $\sigma_{L\emptyset} = 44.53 \pm 2.37$  mb[14].

Once  $\sigma_{L,\emptyset}$  is known, the luminosity  $(\mathcal{L})$  is calculated via:

$$\mathcal{L} = \frac{\mathcal{R}}{\sigma_{\mathcal{L}\boldsymbol{\mathcal{D}}}} \tag{3.1}$$

where R is the number of events seen per second by the Level  $\emptyset$  detector. The total integrated luminosity seen by  $D\emptyset$  during run 1B data taking was  $\approx 92 \text{ pb}^{-1}$ .

### 3.2.5 The DØ Calorimeter

The events in this analysis are measured primarily in the calorimeter, therefore it will be given special attention. The calorimeter provides a measurement of hadron position and energy, as far forward as  $|\eta| = 4.1$ .

Recall that a jet is largely made up of hadrons which deposit their energy primarily in the calorimeter. The DØ calorimeter is divided into three separate calorimeters, one central (CC) and two forward, endcap, calorimeters (EC). The calorimeter is pictured in Figure 3.3. The calorimeters are composed of uranium, used as an absorber, and liquid argon, the ionization medium. They are composed of thousands of cells, one of which is pictured in Figure 3.4. As a particle passes through a calorimeter cell, a shower of particles is created as the uncharged particle interacts with the absorber plate. The shower then ionizes the liquid argon; an electric potential draws these ions toward the pad. The resulting current is proportional to the energy of the incident particle. To calibrate the cells, a test beam measurement

was performed where hadrons of known energy were directed into a calorimeter cell.

In this way, the sampling calorimeter cells could be calibrated to measure hadron energy.

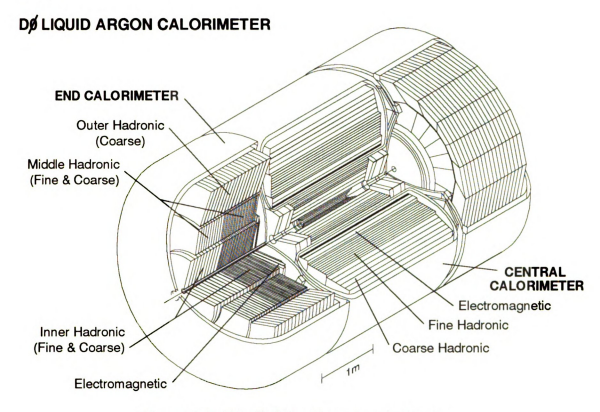


Figure 3.3: The DØ liquid argon calorimeter.

The central calorimeter subtends a rapidity interval of  $|\eta| \le 1.1$ . It has different modules to measure different kinds of particles as one moves outward radially from the interaction region. Closest to the center of the detector is the electromagnetic (EM) calorimeter, used for measuring electromagnetic showers, which uses thinner uranium plates. After the EM calorimeter, is the fine hadronic (FH) calorimeter which uses thicker uranium plates and finally the coarse hadronic (CH) calorimeter which uses copper or stainless steel as absorbing material. The EM calorimeter is closer to the center of the detector because electromagnetic objects tend to develop showers earlier than hadronic objects. Each cell in the CC has an area of  $0.1 \times 0.1$ 

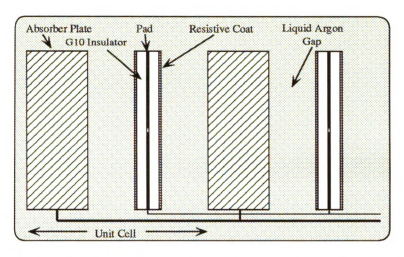


Figure 3.4: A DØ calorimeter cell.

in  $\eta - \phi$  space. The cells are stacked into towers which point back to the interaction region. The forward calorimeters extend the coverage to  $|\eta| = 4.1$  and with a few exceptions are very similar to the CC. The calorimeter towers are seventeen cells deep and number approximately 50,000. A cross section of the calorimeter is shown in Figure 3.5.

Calibrating the calorimeter to exactly measure the energy of a particle, or eventually a jet; determining the *energy scale* of the calorimeter, is a difficult challenge which will be discussed in detail in later chapters.

In Figure 3.6, we present an event as seen by the DØ detector. The various subdetectors are represented; energy is visible in the calorimeter. Two distinct regions of energy deposition are in fact visible; this event finds its way into the same side cross section in the bin  $1.5 \le |\eta| \le 2.0$ , as two forward jets were found.

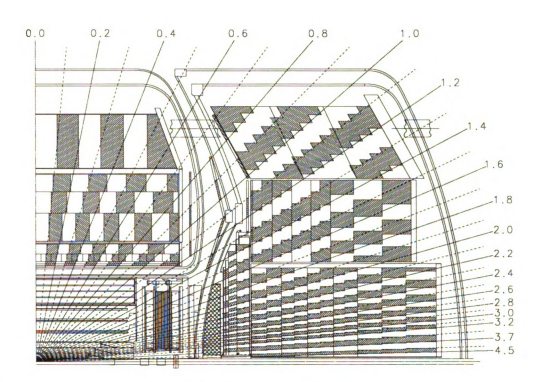


Figure 3.5: A cross section of the DØ calorimeter, the numbers have units of pseudorapidity.

Figureside avera

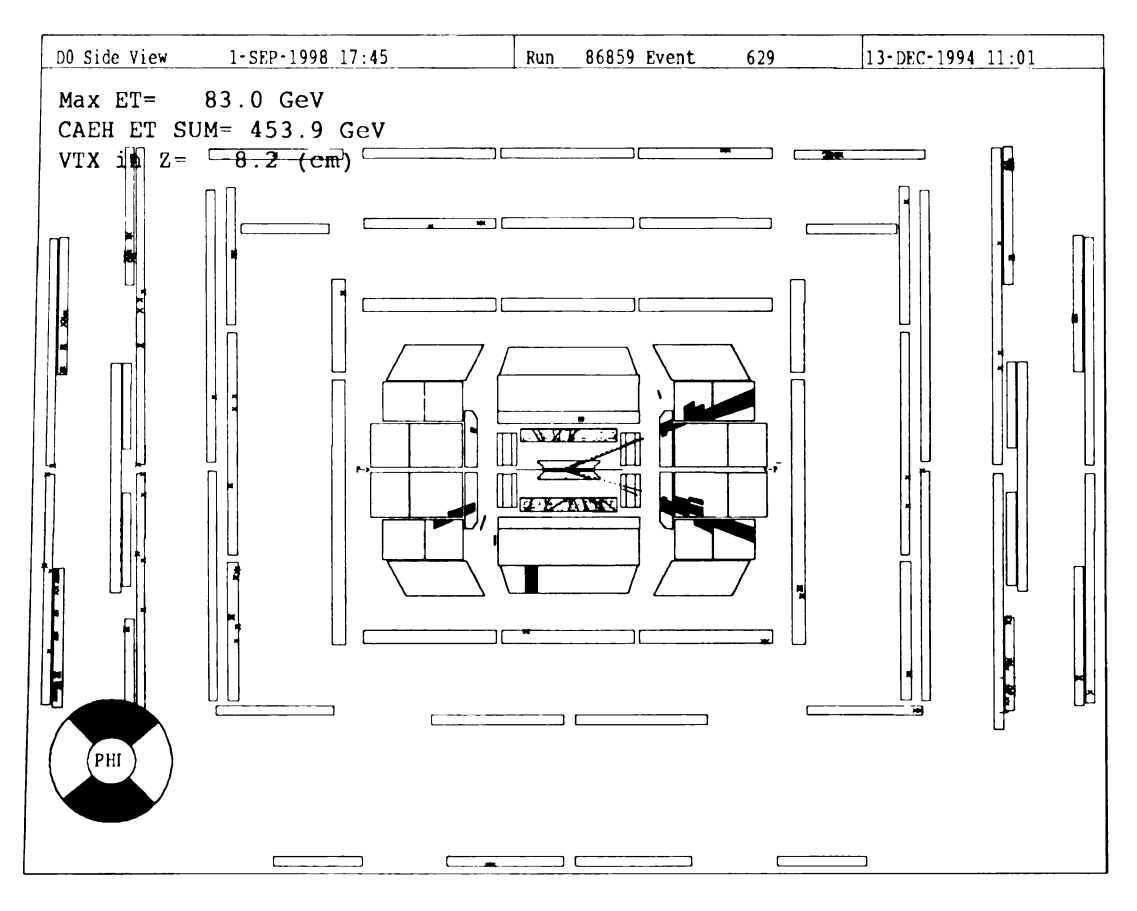


Figure 3.6: An event as seen by the DØ detector. This event is part of the same side forward cross section. The z axis defines left to right; the information has been averaged in  $\phi$ .

The the

6.6 26.8

du

3.

Ti tin

Ze

tha

â۲ę at

ęχ

tri,

þr

 $\pi_{ij}$ jet,

of

is no

## 3.3 Data Filtering and Reconstruction

The crossing time for  $p\bar{p}$  bunches at the Fermilab Tevatron during the run in which the data used in this analysis was taken was 3.5  $\mu sec$ . Relatively few of these bunch crossings result in an interaction with considerable momentum exchange. A trigger system was designed to reduce the event rate recorded by discarding uninteresting events during data taking. Events are further streamed offline after data taking during event reconstruction.

## 3.3.1 The DØ Trigger System

The DØ trigger system, pictured symbolically in Figure 3.7 $^{\dagger}$ , consists of three distinct levels, level Ø, level 1 and level 2. Level Ø uses the previously described Level Zero detector to determine only if an interaction took place. If level Ø determines that there was an interaction, the event is passed on to level 1. Calorimeter towers are  $0.2 \times 0.2$  areas in  $\eta - \phi$  space, directly linked to the level 1 system. Level 1 looks at the energy detected in these towers to decide if a jet of appreciable energy may exist. In this way, level 1 determines if any of the interactions detected by level Ø produced anything interesting. What is interesting is determined by a trigger list. A trigger list for jet events, for example, might require only that one jet was detected with energy above some threshold. Level 1 has very little time to reconstruct the jet, so it doesn't do a complete job. Level 1 simply determines a rough estimate of the jet energy to see if it should be passed to level 2. For example, assume,

<sup>&</sup>lt;sup>†</sup>in Figure 3.7, level 1.5 is an intermediate trigger used to reduce the rate of electron events, it is not used in jet triggers.

in constructing a trigger list, it is desired to measure 100 GeV jets. The trigger list should be designed with a level 1 threshold lower than 100 GeV so that events which fluctuate below the cut are not lost. After full reconstruction, the jet energy can be more accurately determined and the decision to keep the event can be made again. If an event passes level 1, it is passed to level 2. Level 2 is a collection of 48 Digital processors running identical executables. Level 2 takes in information from all detectors in an attempt to fully reconstruct the event. If, after study by level 2, the event is still interesting, it is written to a disk buffer and eventually written to tape. The information on the tape is usually referred to as raw data.

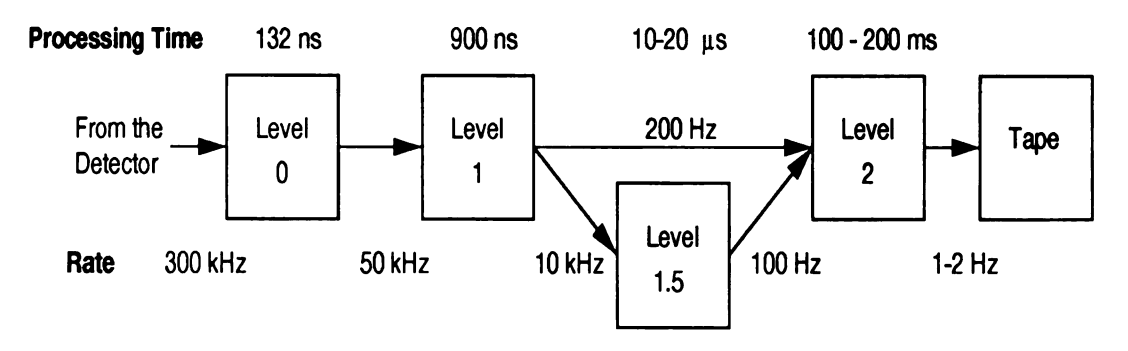


Figure 3.7: Block diagram of the DØ trigger system.

### 3.3.2 Offline Reconstruction

Raw data are taken, in tape form, to another physical location at Fermilab for offline processing. A large and complicated reconstruction package runs though the raw data and produces the final event lists. This package has access to test beam information in addition to data taken during surveys of the DØ detector. Additionally, the reconstruction package allows each physics group to access the interesting data without sorting through all the collider data taken during the run. Usually, as in the case of this analysis, the data are compressed even further, so that

only the events of interest to a particular analysis are kept.

### 3.3.3 Triggers

The combination of level  $\emptyset$ , level 1, and level 2 restrictions collectively define a trigger list. One trigger list can have many different triggers, designed for different physics analyses. The events in this analysis were taken using four QCD jet triggers, named  $Jet_{-}30$ ,  $Jet_{-}50$ ,  $Jet_{-}85$ , and  $Jet_{-}max$ .  $Jet_{-}30$ , for example, is designed to take events with at least one jet roughly at or above 30 GeV. Due to imperfect level 1 and level 2 energy resolution, jets are taken well below this cutoff. Additionally, due to a preponderance of jet final states in the data relative to other sorts of physics, jet triggers were subject to various levels of prescaling to reduce their rates. Prescaling involves writing out a fraction of events which pass the triggers; jet events were prescaled at level 2 depending on the luminosity at the time. See Table 3.2 for more details on the triggers used in this analysis.

Name	L1 Threshold (GeV)	L2 Threshold (GeV)
Jet 30 Jet 50 Jet 85 Jet max	15	30
Jet 50	35	50
Jet 85	60	85
Jet max	60	115

Table 3.2: Jet triggers used in the Triple Differential.

After reconstruction, when the jet energy is better understood, one can consider the *efficiency* of the filters, that is the fraction of events which were read out by the trigger system compared to the total number of events which occurred. In this analysis, the triggers were used only where they were 100% efficient[9].

Two additional triggers which should be introduced are the zero bias and the minimum bias triggers. These triggers are used during the derivation of the energy scale correction described in Chapter 4. The minimum bias trigger only requires an interaction in order to read out the detector. It therefore does not usually contain a hard partonic interaction, just a soft proton-antiproton collision. The zero bias trigger essentially requires nothing except a bunch crossing. It reads out the detector during running regardless of what else is going on at the time. As long as timing information from the accelerator indicates that there is a beam crossing, the detector is read out; it is not necessary for there to be a  $p\bar{p}$  interaction to fire the zero bias trigger. The zero bias trigger is useful to study electronic noise and other effects which introduce energy into the detector not associated with the partonic interaction.

## 3.4 Jet Definitions

As described above, a jet is a collection of highly collimated particles resulting from a hard parton-parton scatter. In this analysis, as in particle physics in general, a jet in not uniquely defined. During data taking, the position that a jet occupies in space was determined using one jet definition, after the jet's position was determined, its quantities were re-calculated using a different jet definition. These definitions are presented below.

There are two different algorithms for defining a jet that are relevant to this analysis. The first is called the *Snowmass Accord*, as it was named during the Summer Study on High Energy Physics, in Snowmass Colorado, in 1990. The

second, is referred to as the  $D\emptyset$  algorithm. Each is defined below.

In both cases, one starts with a list of particles or calorimeter cells. Both algorithms are referred to cone algorithms in that they draw a cone around some central point to determine which particles in the list belong in the jet. In the Snowmass Accord, a reasonably high energy particle is chosen as a beginning, usually called a seed. A cone of radius R is drawn around the seed and the energy of each particle or cell in this circle is considered in the following calculations:

$$E_T = \sum_{i=1}^{ncells} E_{Ti} \tag{3.2}$$

$$\eta = \frac{\sum_{i=1}^{ncells} \eta_i E_{Ti}}{E_T} \tag{3.3}$$

$$\eta = \frac{\sum_{i=1}^{ncells} \eta_i E_{Ti}}{E_T}$$

$$\phi = \frac{\sum_{i=1}^{ncells} \phi_i E_{Ti}}{E_T}.$$
(3.3)

A new jet axis is drawn and the procedure is repeated until a stable jet axis is found. This  $E_T$  weighting scheme is alleged to be the desired method for cone jet definition[15].

The DØ definition then takes the cells in the physical space defined by the Snowmass Accord and recalculates  $E_T$ ,  $\eta$ , and  $\phi$  according to

$$E_T = \sum_{i=1}^{ncells} \sqrt{(P_{X_i}^2 + P_{Y_i}^2)}$$

$$\theta = asin(\frac{E_T}{E})$$

$$\eta = -log(tan(\theta/2))$$

 $<sup>^{\</sup>ddagger}R$  is in  $\eta - \phi$  space; the jets in this analysis have R = 0.7. That is,  $R = \sqrt{(\Delta\phi^2 + \Delta\eta^2)} \le 0.7$ .

$$\phi = atan(\frac{P_X}{P_Y}).$$

To state the problem, there is a claim that this definition is not the best one to use when comparing to theoretical predictions; this claim is the subject of a recent theory paper[15].

The effect of this ambiguity on the Triple Differential will be discussed in Chapter 4. The DØ definition was the result of early Monte Carlo studies in which the DØ algorithm was seen to more closely reproduce the angles of the Monte Carlo jets before detector simulation.

Now that the detector has been introduced and we have a good understanding of the theory, we move on to the measurement of the Triple Differential itself.

# Chapter 4

# The Data

In this chapter we introduce the experimental form of the measurement and the methods necessary to calculate the *raw* cross section. The raw cross section has been energy scale corrected and subject to different cuts and variable corrections. It has not been completely corrected, the final steps are presented in Chapter 5.

## 4.1 The Measurement

As discussed in Chapter 2, a cross section defines the space for a specific type of initial and final state process. The Triple Differential is a measurement of the  $E_T$  and  $\eta$  distributions of 2 or more jet final states. The experimental differential cross section is expressed as:<sup>†</sup>

$$\frac{\partial^3 \sigma}{\partial \eta_1 \partial \eta_2 \partial E_T} = \frac{\Delta N}{\mathcal{L} C V \Delta \eta_1 \Delta \eta_2 \Delta E_T \epsilon_{cut}}.$$
 (4.1)

<sup>&</sup>lt;sup>†</sup>Another useful representation is:  $p\bar{p} \rightarrow 2$  jets + anything.

In Equation 4.1, N is the number of events that pass our cuts,  $\Delta \eta$  is the width of pseudorapidity bin considered,  $\Delta E_T$  is the width of the  $E_T$  bin, C is the unsmearing correction,  $\mathcal{L}$  is the luminosity, V is the vertex resolution correction, and  $\epsilon_{cut}$  is the efficiency of all of our cuts. These cuts are defined below, the corrections are defined in Chapter 5. We require each event to have at least two jets. The binning of the cross sections is as defined in Chapter 2, each cross section is represented as a one dimensional plot; the Triple Differential for a specific  $\eta$  bin vs  $E_T$ . Cartoon representations of two jet topologies for two slices of the Triple Differential appear in Figure 4.1.

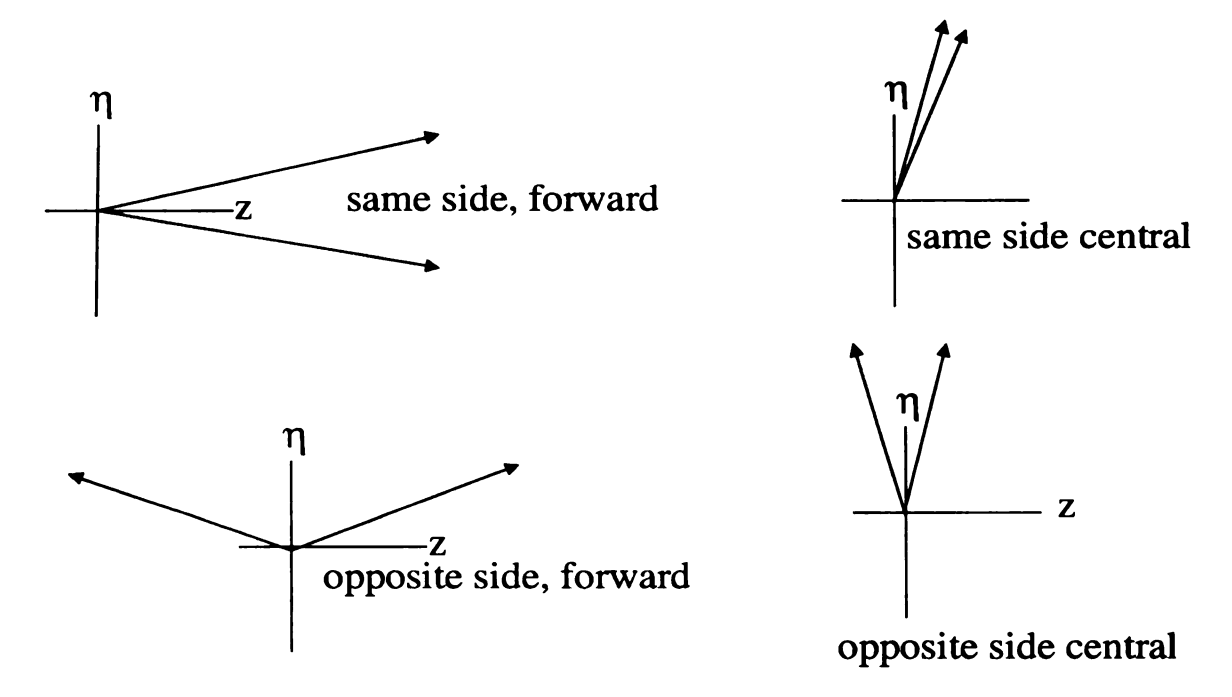


Figure 4.1: Cartoon representation of jets for two slices of the Triple Differential.

This analysis uses the four jet triggers introduced in Chapter 3;  $Jet_30$ ,  $Jet_50$ ,  $Jet_85$  and  $Jet_max$ , with a total integrated luminosity of 0.339, 4.61, 54.7, 91.9 pb<sup>-1</sup> respectively. The triggers are used only where fully efficient in  $E_T$  as defined in [9] and discussed in Chapter 3.

The theoretical prediction to which we will eventually compare the cross sections is pure in the sense that it doesn't reflect any detector effects. We will correct the measured cross sections for all known detector effects for eventual comparisons to theory.

A jet, once defined, is by no means uniquely defined. In a complicated detector many effects can falsely be reconstructed as a jet. *Jet quality cuts* are applied to the data set to remove ill-defined jets from the sample. Additionally, bad events can fool the trigger system; careful consideration of select variables can remove these events from the sample as well.

# 4.2 Quality Cuts

Two separate event quality cuts are considered in this analysis. Events must satisfy a cut involving missing  $E_T(E_T)$  and vertex position.

## **4.2.1** Missing $E_T$ cut

Due to conservation of momentum, the total vector  $E_T$  of an event equals zero in an ideal case. In the event of a cosmic shower or other energy in the calorimeter that is not a result of an interaction, the sum of vector  $E_T$  can differ from zero.

The missing  $E_T$  ( $E_T$ ) is defined as the total unbalanced  $E_T$  in the event and is calculated from the vector sum  $E_T$  of all calorimeter cells. Additionally, muon energy is added to the total vector  $E_T$  in the event. The quantity to which we apply a cut is  $E_{T \, lead}/E_T^{\dagger}$  which approaches one in the case of a cosmic shower. The cut is chosen to require that missing  $E_T$  is not greater than 70% of the leading jet  $E_T$ . In Figure 4.2, the  $E_{T \, lead}/E_T$  distribution for the SS slice 1 is presented. Note the bump at  $E_{T \, lead}/E_T = 1.0$ . Events must satisfy  $E_{T \, lead}/E_T \geq 1.43$  in order to be considered in the analysis. §

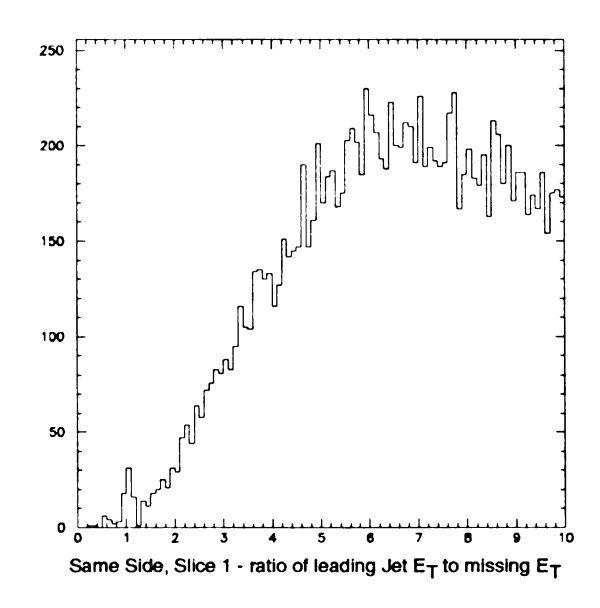


Figure 4.2:  $E_{Tlead}/E_{T}$  for Same Side central jets.

The  $\not\!\!E_T$  cut was designed for previous analyses of jet data, these analyses did not necessarily require two jets in every event. With regard to the Triple Differential therefore, the  $\not\!\!E_T$  cut should be slightly rethought. Events in this analysis are defined such that there are always at least two jets present. For this reason, it is unlikely

 $<sup>^{\</sup>ddagger}E_{T \text{ lead}}$  is the  $E_{T}$  of the most energetic jet in the event.

 $<sup>^{\</sup>S}1/1.43 = 70\%.$ 

that an event would be included in the sample which contained only one energetic jet. It is worth considering within the context of this argument whether a  $\not\!\!E_T$  cut is needed at all. By looking at the  $E_{T\,lead}/\not\!E_T$  distributions for each slice, (Figure 4.3) it was decided to make a  $\not\!\!E_T$  cut on only the SS slice 1 and 2 and the OS slice 1. All other distributions are not subject to a  $\not\!\!E_T$  cut.

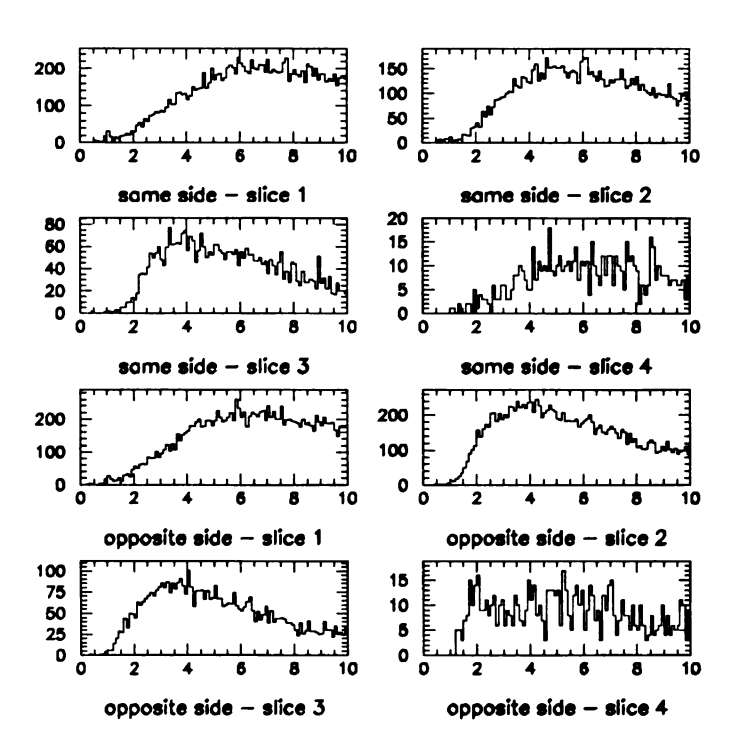


Figure 4.3:  $E_{Tlead}/E_{T}$  for all slices.

When making a cut that removes events from the data sample, care must be taken to account for events that were cut out that did in fact belong in the data set. That is, events which fluctuate below the cut, but are otherwise perfectly good. A correction of this nature is called an *efficiency* and is calculated, along with a corresponding error, for all the cuts described here.

In the case of the  $E_T$  cut, the efficiency is calculated by finding a function that fits the  $E_T$  distribution above the cut and extrapolating this function past the cut.

The integral of this function over the entire  $\not\!E_T$  space is compared to the integral above the cut. The ratio of these two integrals is equal to the ratio of the events included in the cross section measurement above the cut, to the total number of events that belong in the sample; this is the efficiency of the  $\not\!E_T$  cut. In practice, a fit is performed not to the  $\not\!E_T$  distribution, but to  $E_{Tlead}/\not\!E_T$ , as this highlights the region of interest and is the variable we actually cut on. Furthermore, due to the shape of the distribution, the function is fit to a subset of the entire distribution. The integral over the entire  $E_{Tlead}/\not\!E_T$  space is determined by integrating the function over the region of the fit, and adding to the integral the number of events contained in the rest of the distribution. This formalism is presented schematically in Figure 4.4. Two fits are performed and integrated, one which extrapolates below the cut, represented in Figure 4.4 by a solid line, and one which stops at the cut. We define the integrals of this function  $I_1$  and  $I_2$  respectively. Beyond the dashed line, the integrals are determined numerically. The efficiency of the cut is defined as  $I_1/I_2$ .

The error on the  $E_T$  cut is conservatively estimated at  $\pm 0.5\%$ . The  $E_T$  cut efficiency results are presented in Table 4.1.

rapidity range	same side	opposite side
0.0-0.5	0.99	0.99
0.5-1.0	0.99	1.0
1.0-1.5	1.0	1.0
1.5-2.0	1.0	1.0

Table 4.1:  $E_T$  efficiency for the 8 slices considered in the Triple Differential. The entries 1.0 correspond to the slices where no  $E_T$  cut is made.

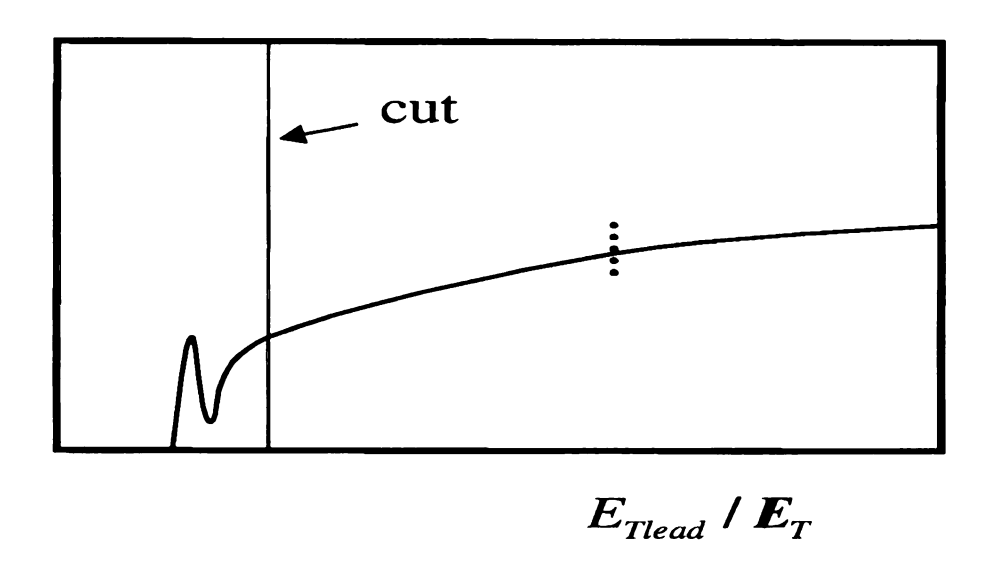


Figure 4.4: Schematic of the calculation of the efficiency associated with the  $\not\!\!E_T$  cut.

### 4.2.2 Vertex Position

The vertex distribution along the z axis in the data set used for this analysis is approximately Gaussian; for the events considered in this analysis the width is approximately 30.0cm. Events with a vertex far from the center of the detector are in principle completely usable. However, due to the projective nature of the DØ calorimeter, good jet reconstruction is difficult if the vertex is too far from Z=0. Therefore, events in this analysis are subject to the restriction  $|Z| \leq 50.0cm$ . As stated above, all the events contained in the vertex distribution are usable events. For this reason, the efficiency can be calculated without differentiation of events that

failed the cut because they were 'bad' and events that failed due to some fluctuation. All events in the vertex distribution are assumed to be 'good' events. They have, in fact, passed all other good jet and event cuts. Therefore the vertex cut efficiency is defined as the ratio of the total number of events with  $|Z| = \pm 50.0cm$  to the total number of events in each slice before the cut. Figure 4.5 is the vertex distribution for two representative slices. No systematic differences in vertex distributions were observed between same side and opposite side events. The error associated with the vertex cut efficiency is assumed to be binomial and is defined as

$$\delta Z_{eff} = \sqrt{rac{(1 - N_{pass}/N) * N_{pass}/N}{(N-1)}}$$

where  $Z_{eff}$  is the vertex cut efficiency,  $N_{pass}$  is the number of events that satisfied the vertex cut and N is the total number of events in the slice. The vertex efficiency is determined separately for all 8 slices, the results are tabulated in Table 4.2.

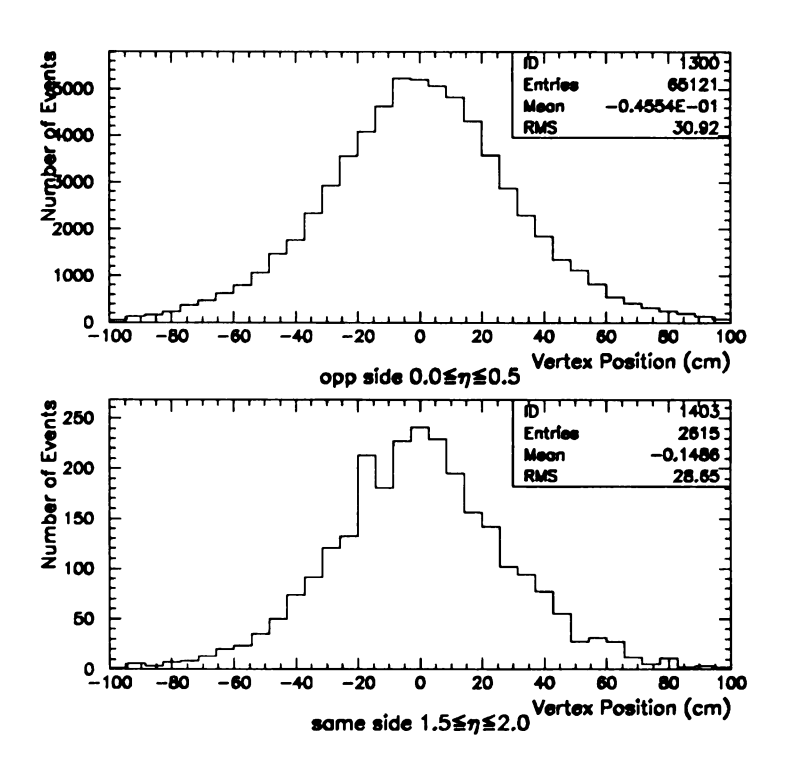


Figure 4.5: Vertex Distribution (before cuts) for two slices of the Triple Differential.

rapidity range	same side	opposite side
0.0-0.5	$0.89 \pm 0.001$	$0.89 \pm 0.001$
0.5-1.0	$0.90 \pm 0.002$	$0.90\pm0.001$
1.0-1.5	$0.90 \pm 0.003$	$0.89 \pm 0.002$
1.5-2.0	$0.90 \pm 0.006$	$0.92 \pm 0.004$

Table 4.2: Vertex cut efficiency and errors for 8 slices of the Triple Differential.

An additional concern exists regarding vertexing at  $D\emptyset$ . The reconstruction package applied to the raw data determines the longitudinal position of the interaction, usually referred to as Z. During high luminosity running, when the number of protons and anti-protons in the bunches is large, there is likely to be additional interactions, which could results in additional vertecies detected. The energy deposited by these additional interactions is usually small and corrected for by the

energy scale correction described later in this chapter. However, the jet quantities,  $E_T$  and  $\eta$ , are calculated with respect to the vertex position. These quantities are referred to as *physics* quantities as opposed to *detector* quantities as they are referred to when they are calculated with respect to Z=0; physics  $E_T$  and  $\eta$  are used in measuring the Triple Differential. A mis-measurement of the vertex position can affect the physics quantities. The reconstruction package usually chooses the right vertex, however, a different algorithm for vertex selection in jet events is seen to do better. The quantity  $\vec{H_T}$  is defined as the vector sum of the energy of each calorimeter cell. This quantity is expected to be at a minimum when calculated with respect to the correct vertex. This vertex selection method chooses the correct vertex more often than the reconstruction package, therefore, in the event that more than one vertex is found during reconstruction, the vertex is chosen with this method.

## 4.2.3 Jet Quality Cuts

In addition to the event quality cuts, cuts are applied to the two leading jets in the event, designed to remove spurious jets. These "unreal" jets, which due to some fluctuations are included in our sample, are removed with these jet quality cuts which have been studied exhaustively[10]. We include a brief description of the cuts together with their efficiencies and errors below.

<sup>¶</sup>In high energy jet physics masses are usually neglected; the assumption is made that  $E \approx P$ .

This conclusion is supported by event scanning.

### **Electromagnetic Fraction Cut**

Three separate quality cuts are applied to the jets in the data set used in this analysis. The first is primarily designed to remove electromagnetic objects falsely reconstructed as jets. As described in Chapter 3, the DØ calorimeter contains an electromagnetic and then a hadronic calorimeter; jets are expected to deposit their energy in both. The EM fraction (EMF) is the fraction of the total jet energy deposited in the electromagnetic calorimeter. A cut on the jet EMF is applied as defined in Table 4.3.

### Coarse Hadronic Fraction Cut

The coarse hadronic calorimeter surrounds the main ring accelerator above the Tevatron. The main ring houses low energy proton and anti-proton bunches. These bunches can interact and create a shower of energy in the coarse hadronic calorimeter which could be mis-interpreted as a jet. To protect against this, a cut is placed on the fraction of the jet energy deposited in the coarse hadronic calorimeter (CHF). This cut is also defined in Table 4.3.

### Hot Cell Fraction Cut

The calorimeter is made up of many cells connected by complicated electronics. It is possible that a single cell may light up<sup>†</sup> due to an electronic fluctuation or other noise. If a jet is found to contain one cell with much more energy than its immediate neighbors, it is suspected to be a bad jet. A cut is placed on the hot cell fraction

<sup>†</sup>appear to detect energy

(HCF), the ratio of the next to most energetic (hottest) cell energy to the hottest cell energy. This HCF cut is defined below in Table 4.3.

We include sample distributions in Figure 4.6 which contains the EM fraction and CH fraction distributions (on a log scale) for the central same side cross section. The complete set of distributions is presented in reference[10]. As can be seen in Figure 4.6, the EM fraction and CH fraction cuts are very efficient; they do not remove many jets from the data set.

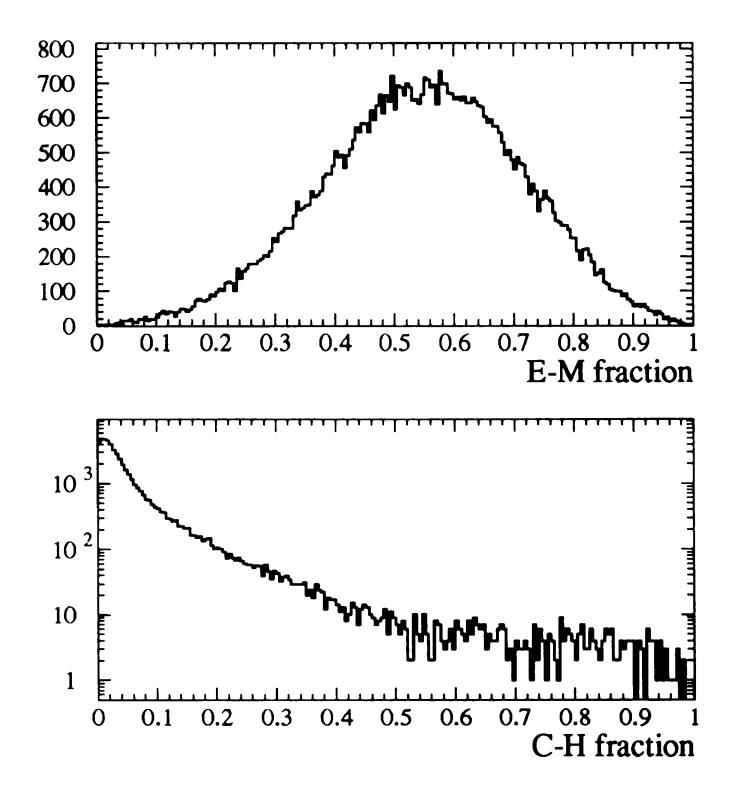


Figure 4.6: Representative electromagnetic and coarse hadronic fraction distributions.

The net efficiency of all the jet quality cuts is > 98% for all slices considered. The errors on the efficiency corrections are corresponding small. In Figures 4.7-4.10, we include the jet quality cut efficiencies for all slices along with the corresponding

Cut name	Cut value	Region applied
E-M fraction	0.00 < EMF < 0.95	ICR
E-M fraction	0.05 < EMF < 0.95	elsewhere
C-H fraction	CHF < 0.6	ICR
C-H fraction	CHF < 0.4	elsewhere
hot cell fraction	HCF < 0.05	everywhere

Table 4.3: Jet quality cuts applied in the Triple Differential. ICR refers to the inter-cryostat region of the calorimeter defined by  $1.0 \le |\eta| \le 1.4$ .

errors on the efficiency corrections. Additionally, we include the total jet + event efficiency errors for completeness, as well.

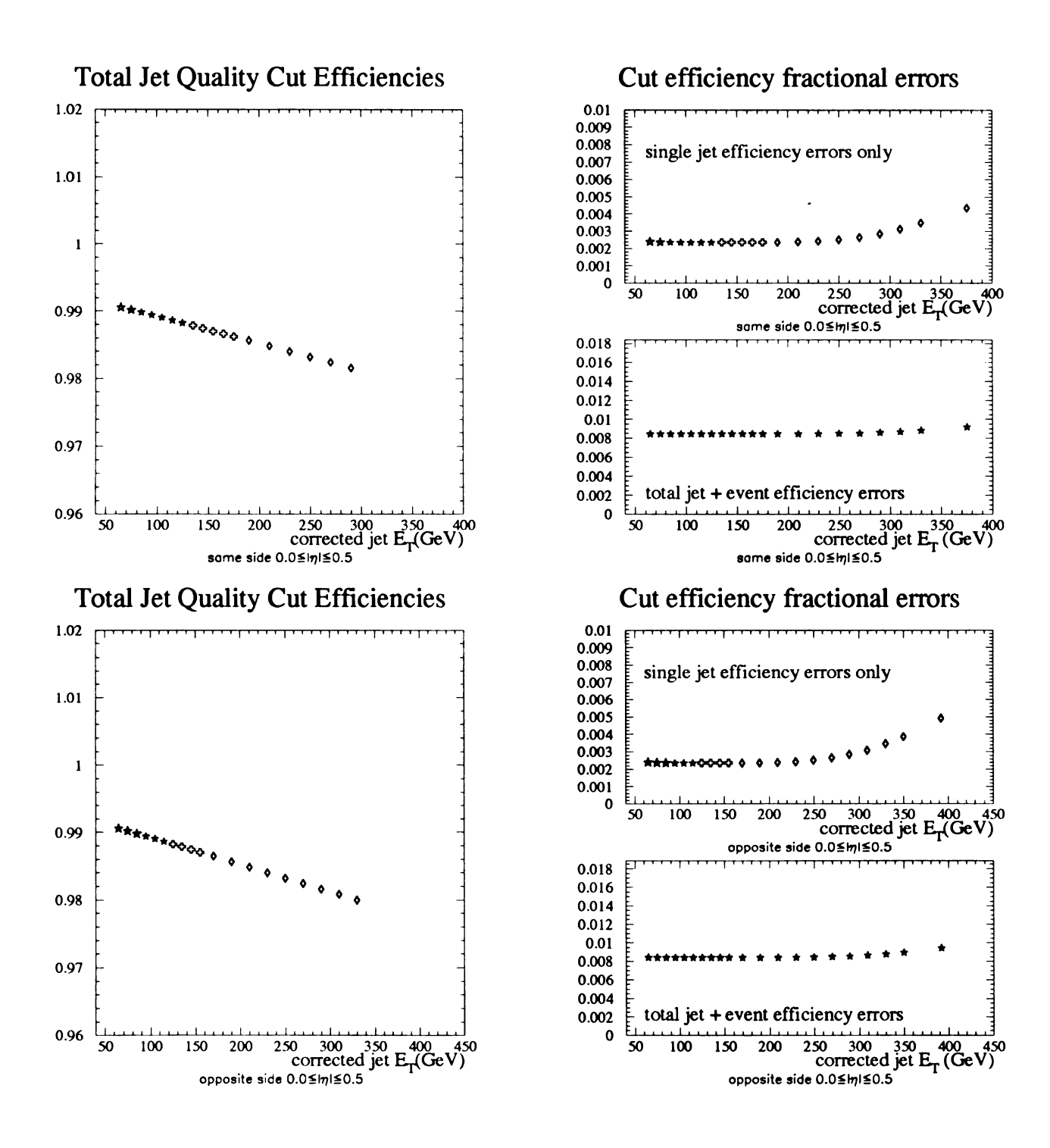


Figure 4.7: Jet and event quality cuts efficiencies and errors for slice 1 of the Triple Differential.

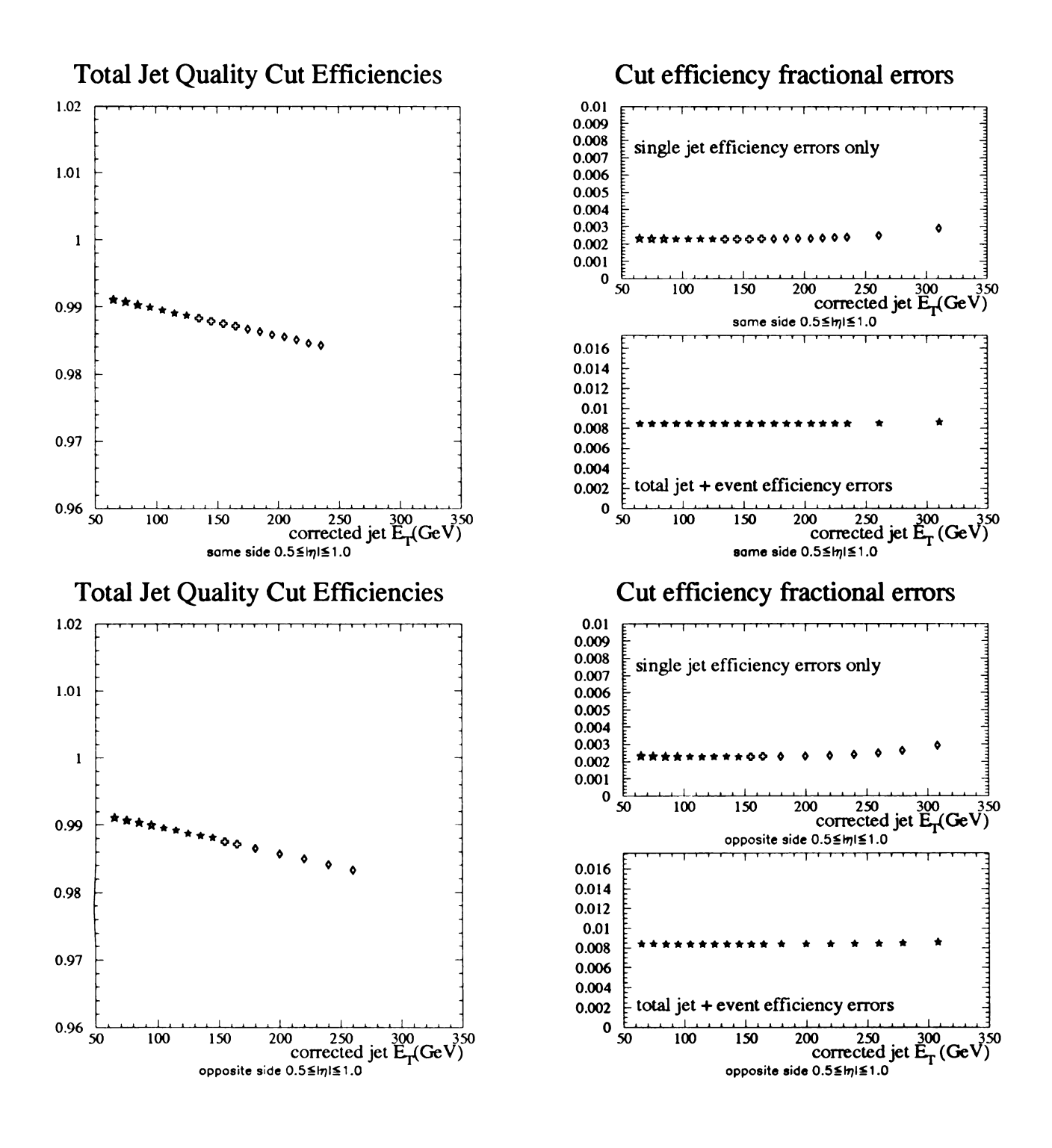


Figure 4.8: Jet and event quality cuts efficiencies and errors for slice 2 of the Triple Differential.

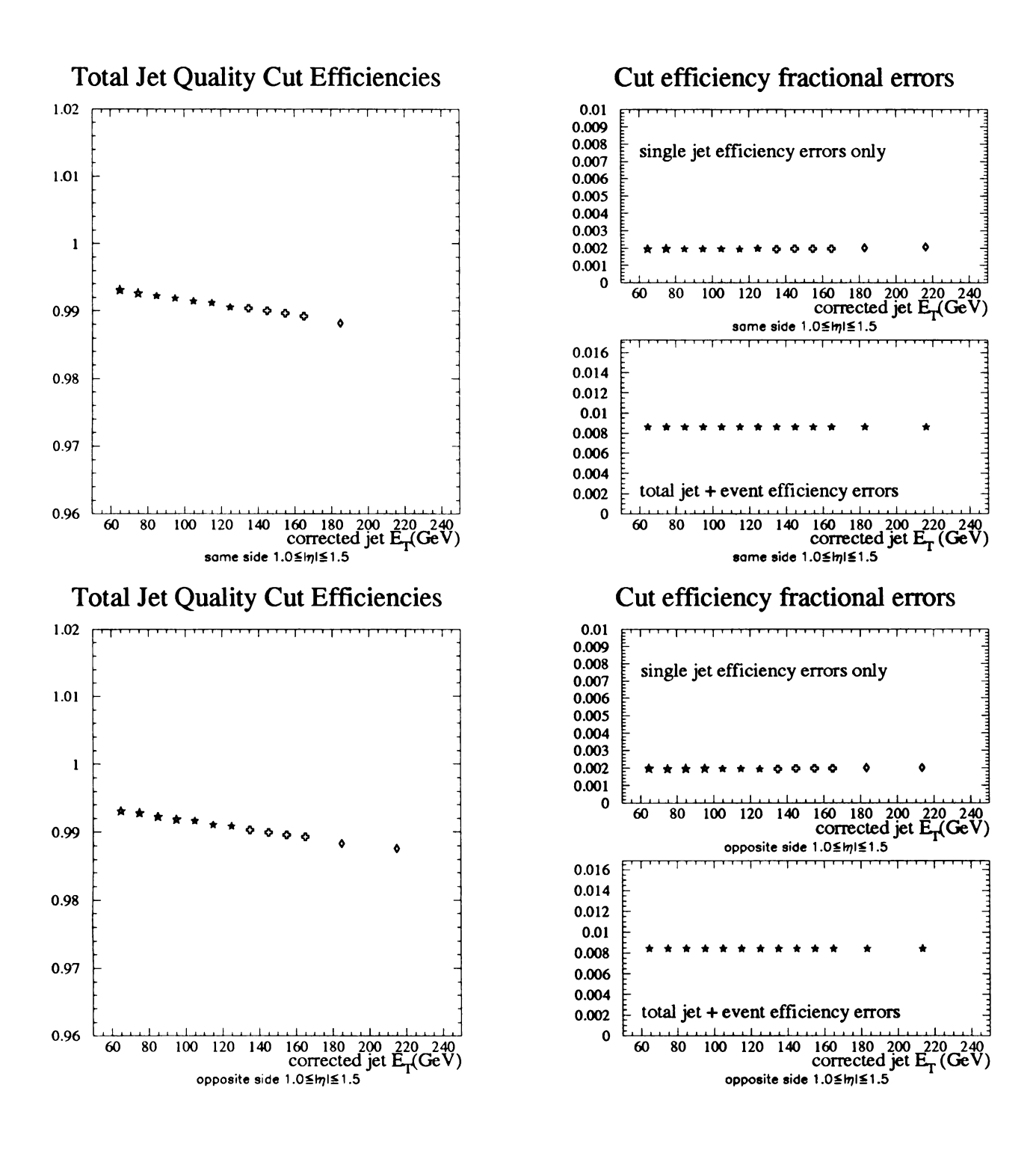


Figure 4.9: Jet and event quality cuts efficiencies and errors for slice 3 of the Triple Differential.

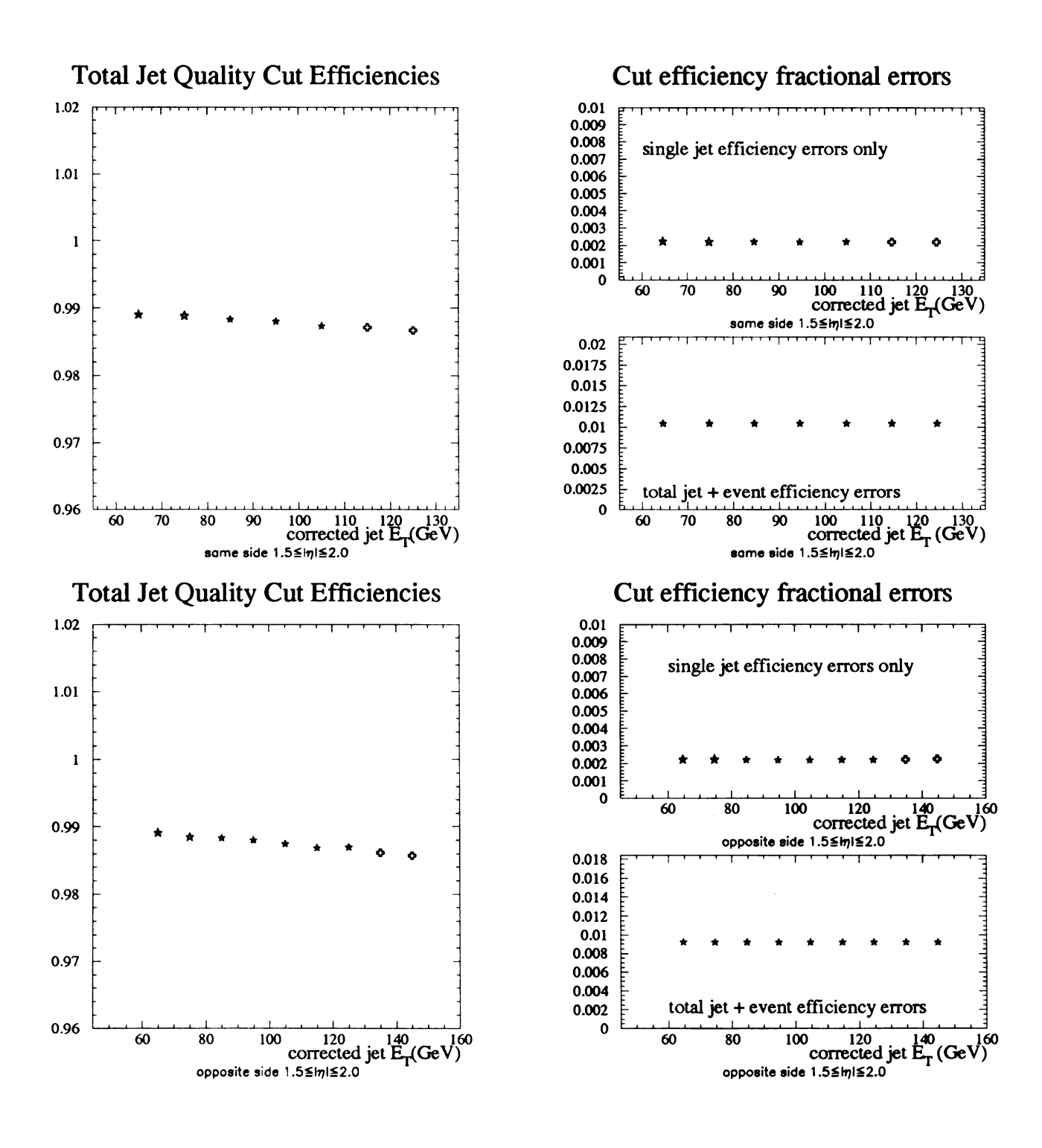


Figure 4.10: Jet and event quality cuts efficiencies and errors for slice 4 of the Triple Differential.

#### 4.3 Corrections to the Data

The goal of this analysis is to report a cross section with all detector effects removed. The detector effects we account for are: jet energy scale, jet energy resolution, vertex position resolution, and the  $\eta$  bias. The  $\eta$  bias refers to the difference in position of the fully reconstructed jet compared to the same jet at the particle level. The jet energy scale corrects the measured jet energy back to the particle jet energy. The jet energy resolution refers to the effect of imperfect energy measurement of the DØ calorimeter: if many particle jets all of energy E, are sampled by the DØ calorimeter, and all other effects are accounted for, a Gaussian distribution centered on E will result. The mean of this distribution is equal to E so one might expect the net effect of the imperfect energy resolution, on average, not to present a problem. However due to the steeply falling nature of the energy distribution of jets from  $p\bar{p}$  collisions, the cross section is "smeared" as a result. We present, in Chapter 5, a method of correcting for this effect, or unsmearing the cross section. Vertex position resolution arises from the study of energy resolution, we will discuss the effect and the corresponding correction in detail in Chapter 5 as well.

#### 4.3.1 Jet $\eta$ Definition

The position of a jet measured by the DØ detector is defined by two quantities:  $\eta$  and  $\phi$ . In this analysis the cross sections are averaged in  $\phi$  so jet  $\eta$  uniquely determines the position of the jet. We consider two disparate effects with regard to jet  $\eta$  definition.

In a Monte Carlo study it can be observed that the reconstructed jet is pref-

erentially more central<sup>‡</sup> than the corresponding particle jet. This  $\eta$  bias has been studied previously [19, 20]. An additional complication arises because the jets in this analysis have been reconstructed with the DØ jet algorithm. A claim has been made that this algorithm is not completely desirable for comparison with QCD theoretical predictions[15]; instead the Snowmass Accord[16] is preferred. These two algorithms produce nearly identical values for jet energy and also for jet  $\eta$ . Any difference in jet  $\phi$  is not considered. The energy difference will be shown to be small enough that it doesn't warrant consideration. However, the difference in jet  $\eta$ , though small, could produce reasonable differences in the final measured cross sections. We use the Snowmass Accord while reconstructing jets in the NLO QCD theory.

To study these two effects, we look at the difference between Herwig jets reconstructed at the particle level with the Snowmass Accord and the same jets reconstructed with the DØ algorithm at the fully simulated calorimeter level. If the difference between particle jets constructed with the Snowmass Accord and calorimeter jets constructed with the DØ algorithm is well behaved, a correction to apply to the jets in our cross section can be derived.

The quantity of interest is  $\eta_{cal}^{D\emptyset} - \eta_{part}^{snow}$ , where  $\eta_{cal}^{D\emptyset}$  is the jet  $\eta$  as defined at the calorimeter level by the DØ algorithm and  $\eta_{part}^{snow}$  is the jet  $\eta$  at the particle jet level as defined by the Snowmass Accord. This quantity will henceforth be referred to as the total  $\eta$  bias. We study this quantity as a function of uncorrected jet energy and DØ calorimeter jet  $\eta$ . Figure 4.11 is the total  $\eta$  bias as a function of DØ jet  $\eta$  for

Herwig jets subject to a cut requiring  $E_T \ge 60.0~GeV$  as in the data. The  $E_T$  and  $\eta$  distributions in Herwig are known be in good agreement with DØ data. From this plot we can see that the effect of the total  $\eta$  bias for  $|\eta| < 1.5$  is negligible. Therefore, no  $\eta$  bias corrections are applied in this region. However, we can see a larger effect in the most forward bin, and indeed it is here we apply a correction. The data within  $|\eta| > 1.5$  are fit to a straight line to derive the total  $\eta$  bias correction. This procedure is followed for several different  $E_T$  bins to derive a correction as a function of  $E_T$  and  $\eta$ . However, no significant  $E_T$  dependence is observed (Figure 4.12). For this reason the correction is applied only as a function of DØ calorimeter jet  $\eta$ . The total  $\eta$  bias, before and after the correction is applied, is shown in Figure 4.13.

To estimate an uncertainty on the total  $\eta$  bias correction, the deviation of the total corrected  $\eta$  bias from zero is used. An uncertainty on jet  $\eta$  of  $\pm 0.005^{\P}$  is assumed and the cross sections are re-derived with this uncertainty applied to jet  $\eta$ . This results in an error on the forward cross sections as demonstrated in Figure 4.14. For completeness, an error due to the total  $\eta$  bias is applied to all slices, however the effect becomes very small in the central region as observed also in Figure 4.14. The total  $\eta$  bias correction error is on the order of 2-4% in the most forward bins and becomes smaller in the central region. The errors are tabulated in Table 4.4. The effect of the total  $\eta$  bias correction can be observed in Figure 4.15 which contains the forward cross sections before and after the corrections are applied and a linear comparison of the cross sections. These figures show a total effect of the correction which depends on the specific  $E_T$  bin considered, but is on the order of 5%.

<sup>¶</sup>See Figure 4.13.

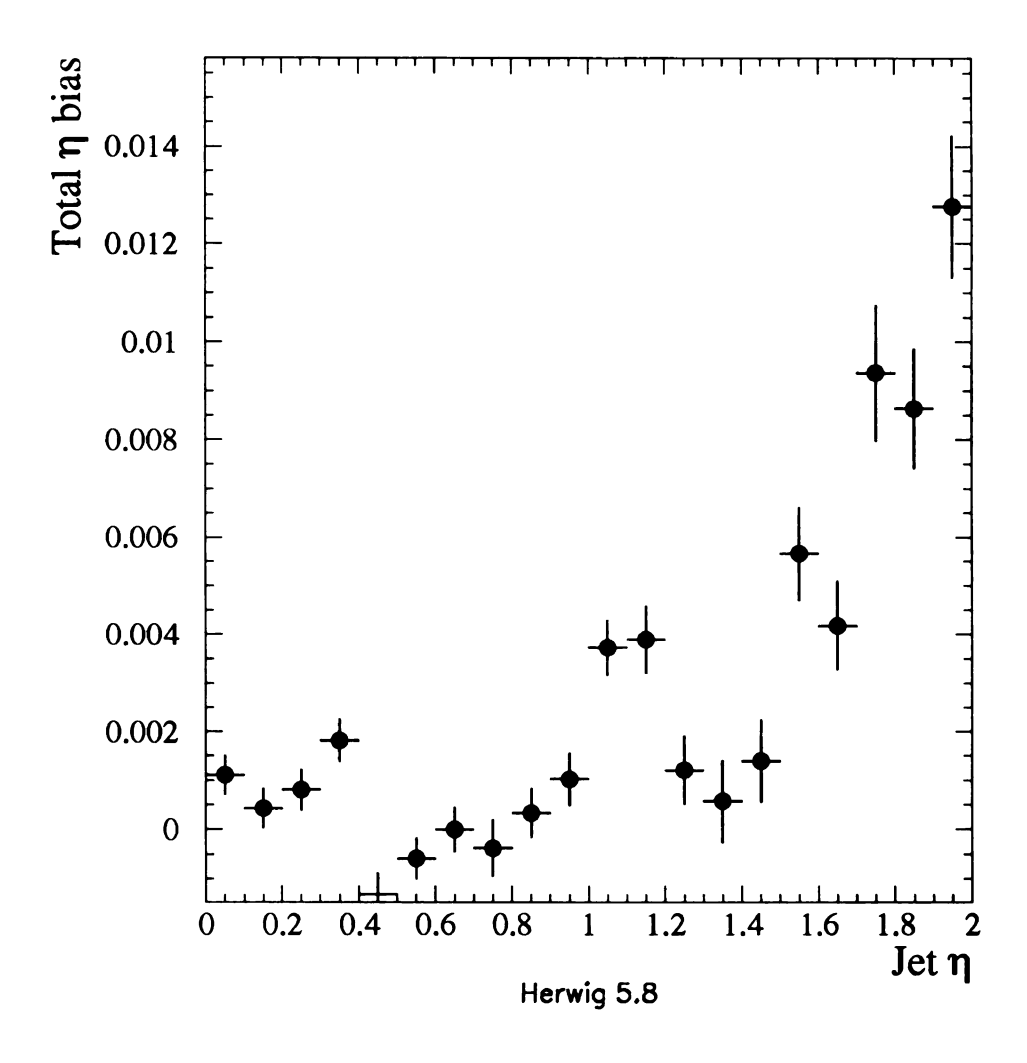


Figure 4.11: Total  $\eta$  bias as measured in Herwig as a function of jet  $\eta$ .

Slice	Topology	$\eta$ bias error
1	SS	< 1%
1	OS	< 1%
2	SS	0 - 2%
2	OS	0.5 - 1%
3	SS	0 - 3.5%
3	OS	0-2%
4	SS	2-6%
4	SS	0.5 - 2%

Table 4.4: Errors on the cross sections due to the total  $\eta$  bias.

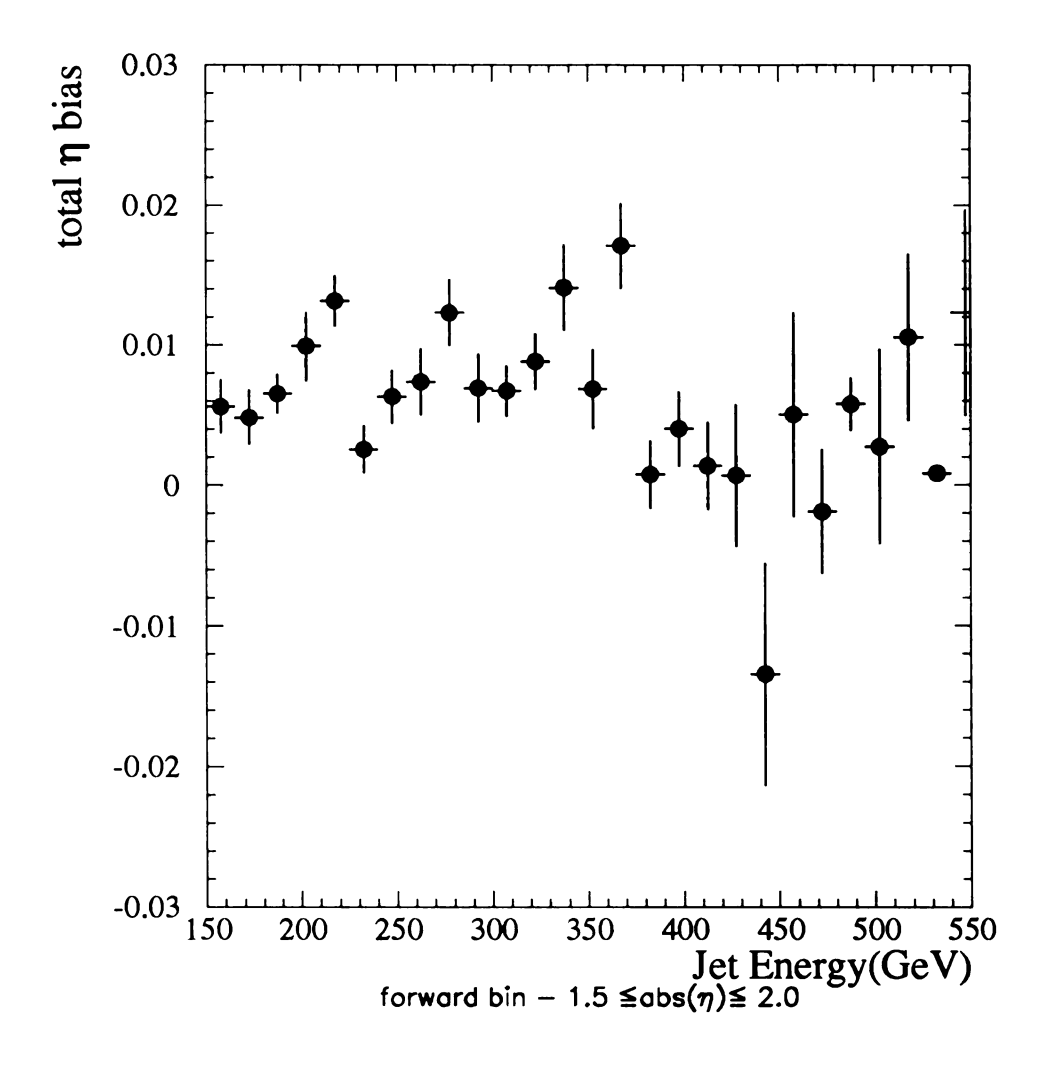


Figure 4.12: Total  $\eta$  bias as measured in Herwig as a function of jet energy.

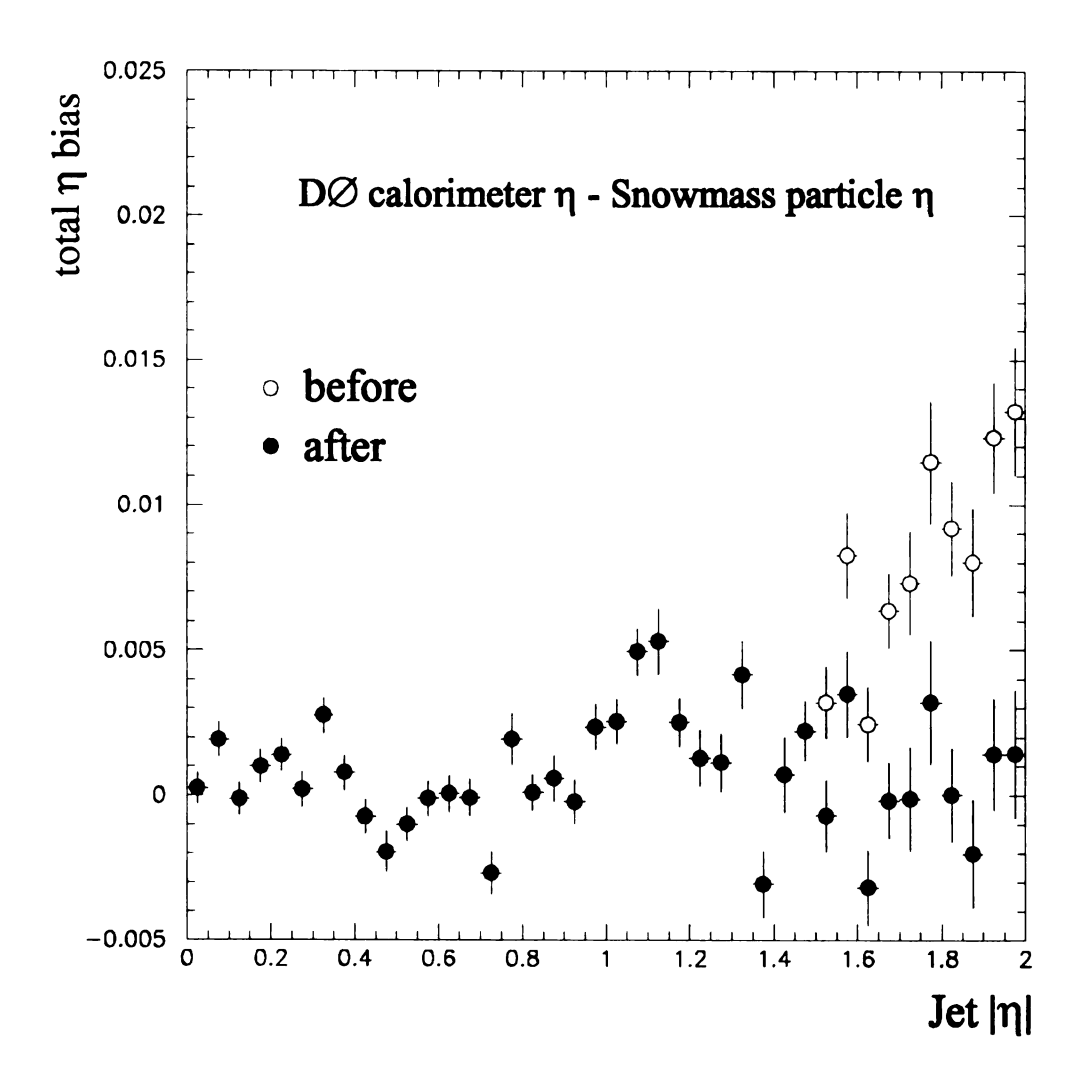


Figure 4.13: Total  $\eta$  bias before and after the total  $\eta$  bias correction.

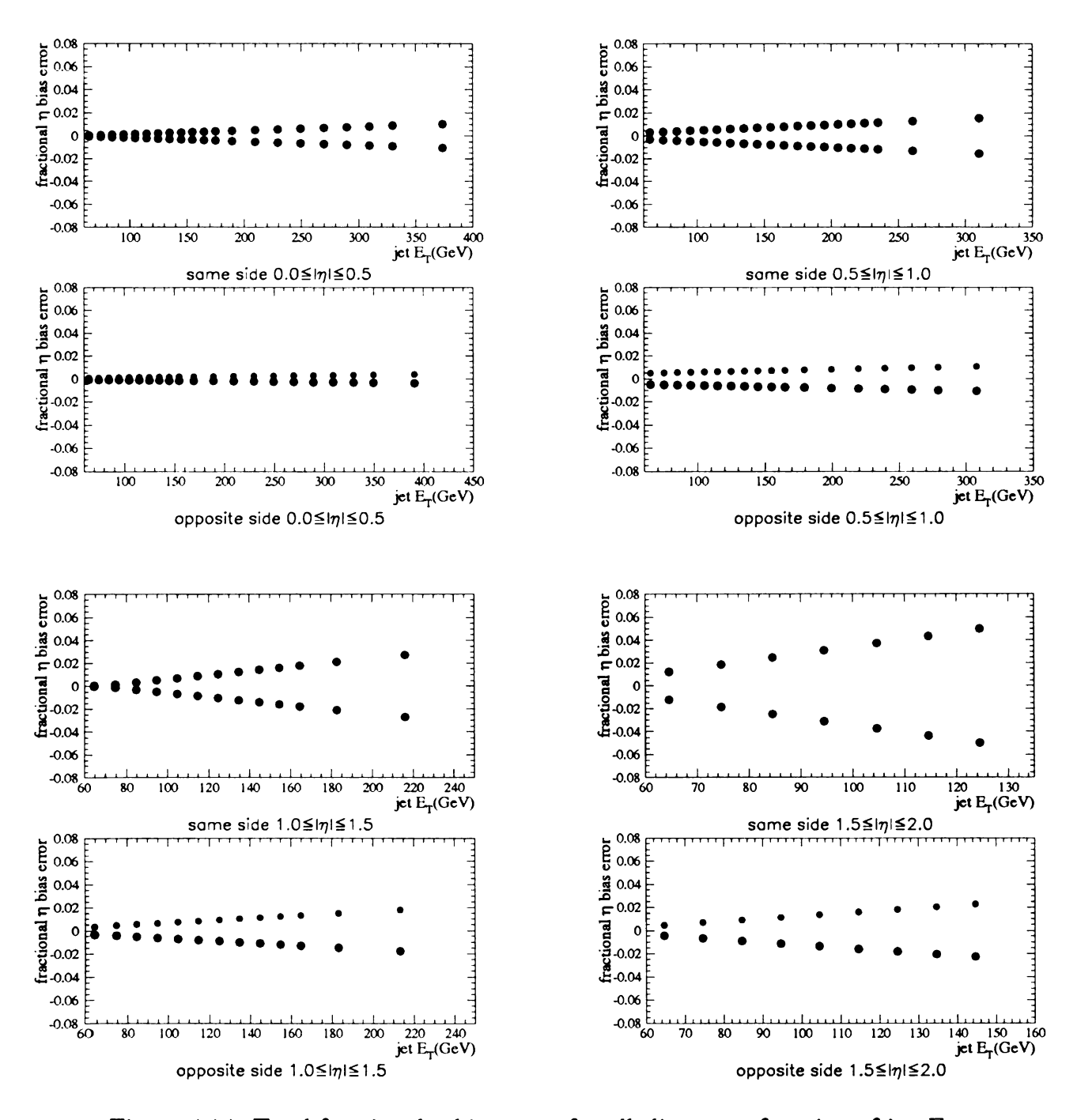


Figure 4.14: Total fractional  $\eta$  bias error for all slices as a function of jet  $E_T$ .

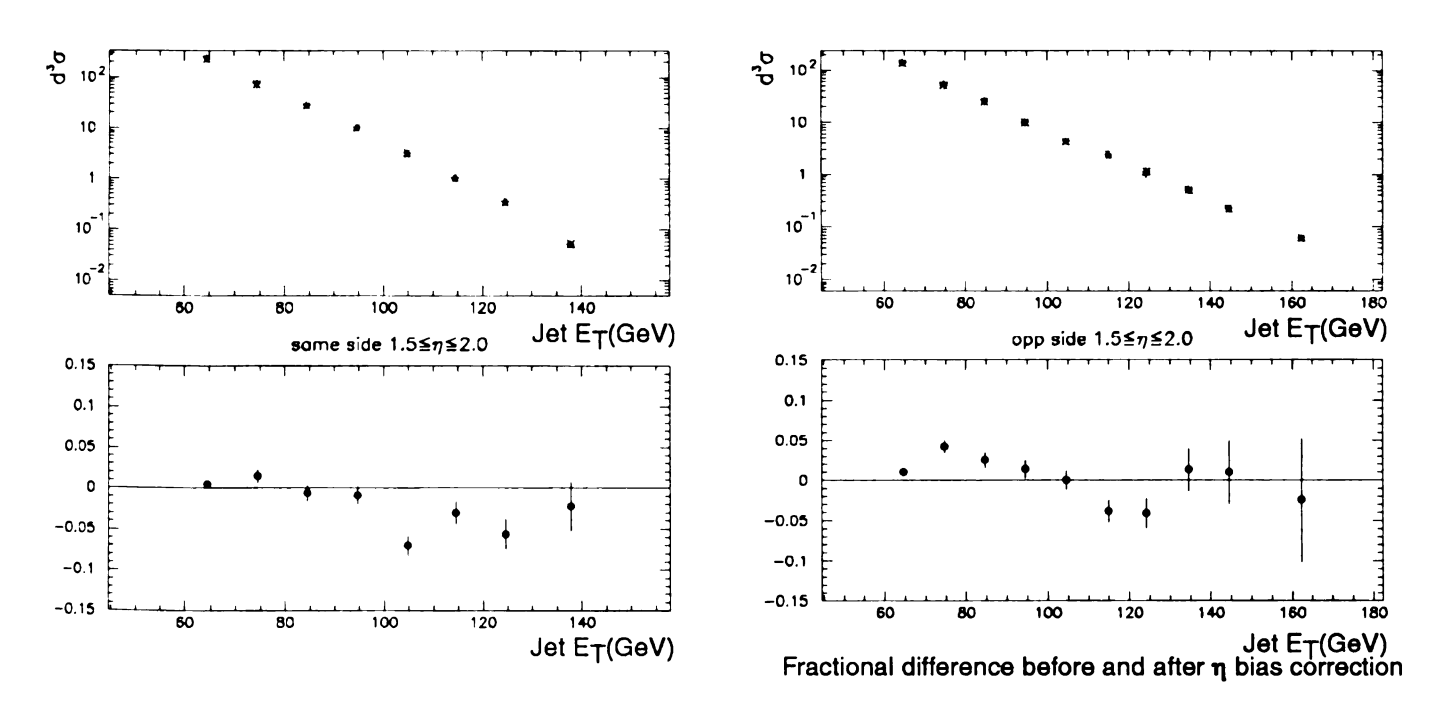


Figure 4.15: The effect of the total  $\eta$  bias corrections on the forward cross sections.

# 4.4 Jet Energy Scale Corrections

As described in Chapter 3, the energy of an object in the DØ calorimeter is not necessarily exactly defined. As hadronic objects deposit energy in the calorimeter, small charge deposits are detected in the individual calorimeter cells. The conversion of this charge to particle energy is determined by enlisting test beam data. However, this is not enough to accurately define the energy of a jet. Other effects not modeled during test beam running can affect the measured jet energy. For example, the test beam did not model the high luminosity environment which exists during data taking. The calorimeter modules used during test beam data taking may not exactly mimic the actual calorimeter. There are different levels of instrumentation in different regions of rapidity not modeled during test beam running. Additionally, during the test beam, single particle response was measured; there is no reason to expect the exact same response for a jet as for a single particle.

The energy scale is a prescription for determining the energy of a jet given its measured energy from the reconstruction package. It depends upon, among other things, the type of jet algorithm applied. DØ has undertaken a significant effort to understand the jet energy scale for cone jets; we will summarize the procedure and the results below.

The jet energy scale correction applied in this analysis is referred to as CAFIX 5.1 and is described in extensive detail elsewhere[11]. The goal of the energy scale correction is to provide a prescription to go from measured jet energy to the corresponding particle jet energy. As described in Chapter 2, a particle jet is a collection of particles in a jet cone, with all detector effects removed.

The jet energy scale correction takes the form

$$E_{ptcl}^{jet} = \frac{E_{meas}^{jet} - O(\Delta R, \eta, \mathcal{L})}{R(\Delta R, \eta, \mathcal{L}, E)S(\Delta R, \eta, \mathcal{L}, E)}$$
(4.2)

In Equation 4.2,  $E_{ptcl}^{jet}$  is the particle jet energy,  $E_{meas}^{jet}$  is the measured jet energy, O is the offset correction, P is the calorimeter energy response, and P is the showering correction, P and P are luminosity and energy, respectively. P is the cone size, 0.7 for the jets in this analysis. Each component is defined below.

#### 4.4.1 The Offset Correction

The offset[12] corrects the measured jet energy for additional energy (energy offset) due to additional interactions, electronic noise and energy introduced by zero suppression which does not belong to the jet. Additionally, a correction is applied to correct the measured jet energy for energy due to additional partonic interactions that occur during the proton break-up; the so-called underlying event. These corrections are explained below.

#### Zero Suppression

During data taking it is not efficient to read out all calorimeter cells. Cells that do not contain any energy other than background electronic noise are not read out. In order to determine a baseline for comparison, a calibration run is taken during which the average energy, and the width of the energy distribution, for each calorimeter cell is recorded. During the calibration run, no protons are in the Tevatron. During

data taking, the energy in each cell is compared to the data from the calibration run and if the energy is within  $2\sigma$  of its average value during the calibration run, the cell is not read out. Unfortunately, the distribution of energy in a cell during the calibration run is not symmetric. Consequently, a  $2\sigma$  cut introduces some energy, on average, into the jet (see Figure 4.16). In order to correct for this, special runs which were not zero suppressed were studied. These runs were taken only with min and zero bias triggers active; in order to determine how zero suppression affects jets, more information is necessary. There is a small probability that a jet will exist in an event that fired the min bias trigger, but clearly there are not very many jets of this type present, and they are likely to be at low energy. Therefore, a correction for zero suppression was derived by studying zero bias data, and a method for scaling this correction to apply to jet events was derived. This scaling is necessary because the amount of energy present in a jet due to zero suppression is a function of how many cells in that jet were suppressed. In the extreme case, a jet with all cells read out would have no zero suppression correction. We define the fraction of cells read out in a jet as the occupancy. We additionally define the fraction of cells read out in a eta slice of the calorimeter over the total number of cells in that slice as the occupancy of a zero or min bias data set. These occupancies for zero bias, min bias, and jet data are presented in Figure 4.17. We can see that jet events have almost twice as many cells read out as the other data sets which implies that the suppression correction for jet events is likely to be smaller than is measured in zero or min bias data.

The energy in a quiet calorimeter cell is caused by (among other things) uranium decay.

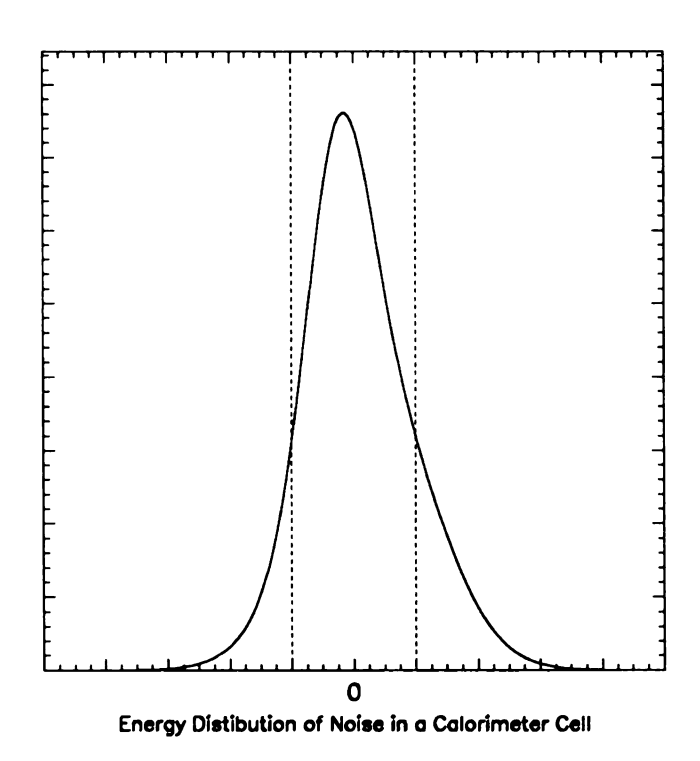


Figure 4.16: Mock plot of energy in a calorimeter cell due to uranium decay and the  $2\sigma$  cut, represented by the dashed lines. Notice the net effect of the cut is positive.

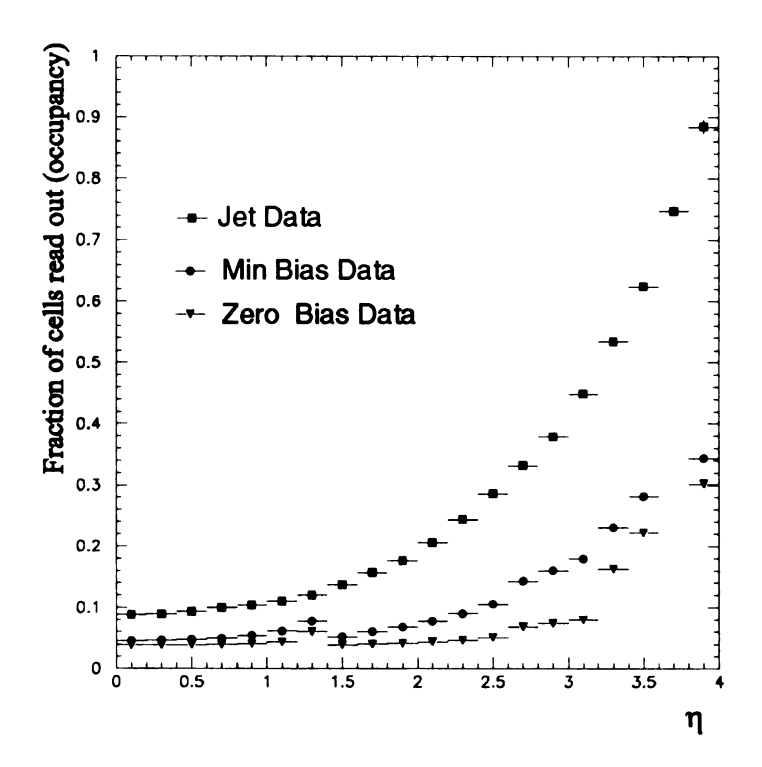


Figure 4.17: Occupancies for the different data sets used in the derivation of the suppression correction.

To study the energy introduced due to zero suppression during zero bias data taking, the quantity  $E_T$  density is introduced. This is the energy measured in a calorimeter tower divided by the area of the tower in  $\eta - \phi$  space. We represent  $E_T$  density as D in this discussion. This quantity is studied for zero bias data which has been zero suppressed and zero bias data which has not been zero suppressed. The difference between these two quantities, is the energy introduced into a zero bias data set due to zero suppression. This quantity is presented in Figure 4.18. Notice that the effect of suppression is luminosity dependent, this is because more cells, on average, are read out at higher luminosity.

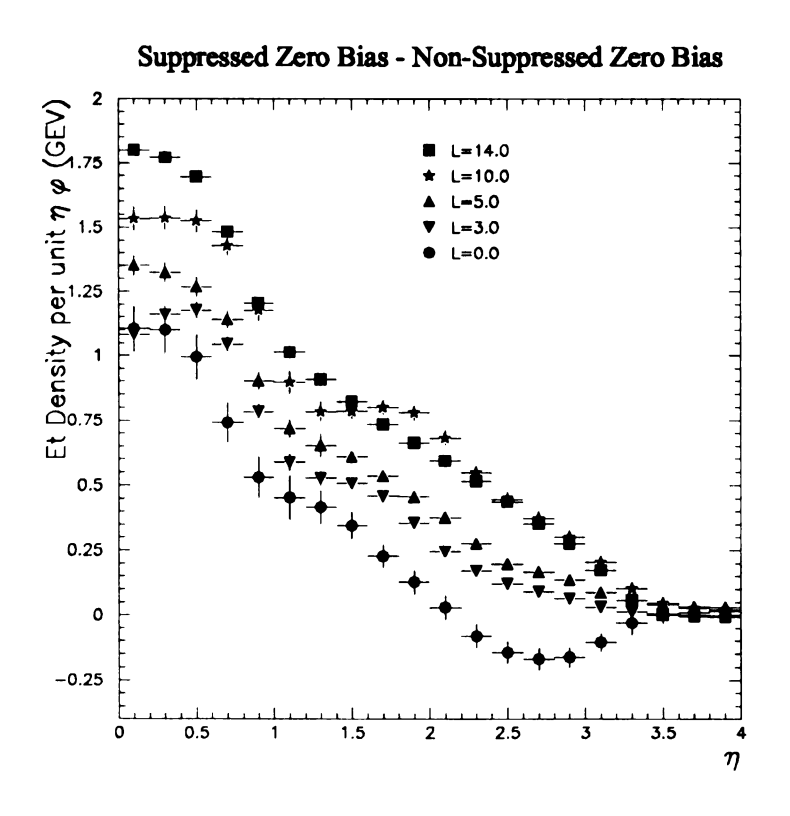


Figure 4.18: Energy introduced into zero bias data due to zero suppression.

The offset correction, however, is applied to jets, so it is necessary to understand

the effect of zero suppression on jet data. We define the following:

$$\delta_{jet} = D_{jet}^{supp} - D_{jet}^{non-supp}$$

and,

$$\delta_{zero} = D_{zero}^{supp} - D_{zero}^{non-supp}.$$

So  $\delta_{jet}$  is the effect of zero suppression on jet data and likewise for  $\delta_{zero}$ . We have observed that the following relationship holds for these data sets:

$$\delta_{jet} = \delta_{zero}(\frac{occ_{zero}}{occ_{jet}})$$

where  $occ_{jet(zero)}$  is the measured occupancy for jet (zero bias) data, as pictured in Figure 4.17. We can use this observation to predict the suppression correction to apply to jet data, measured from zero bias data. Recall that we cannot directly measure  $\delta_{jet}$  except for a small sub-set of data where jets are present in non-suppressed form. This prediction, together with  $\delta_{jet}$  measured from the small set of data where it exists, (for comparison) is presented in Figure 4.19.

The zero suppression correction is derived and applied as a function of jet  $\eta$  and luminosity.

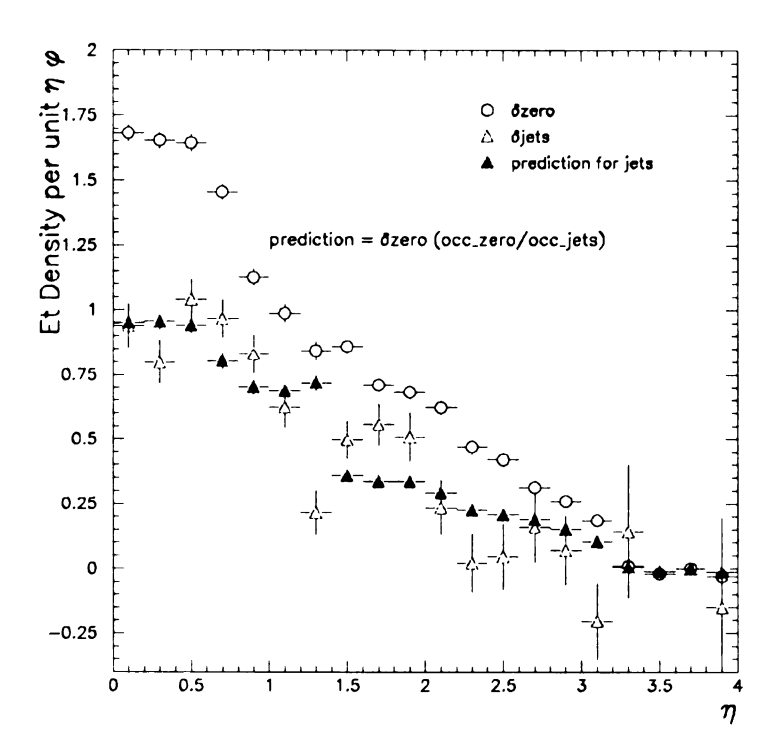


Figure 4.19: Energy due to zero suppression in zero bias and jet data together with prediction based on occupancy, units of  $E_T$  density are  $\text{GeV}/(\eta\phi)$ .

Now that the effect of zero suppression is understood and a mechanism exists for deriving a correction from zero bias data and applying it to jet data, the properties of zero bias data can be further exploited. During a zero bias run, the calorimeter electronics are all active and beam is, in general, circulating; the energy due to additional interactions is present in zero bias data as well. The average number of additional interactions, other than the one that produced the jet in an event that fires a jet trigger, at a given luminosity, is equal to the average number of events in a zero bias data set at the same luminosity. The energy, therefore, in a jet event due to additional interactions is equal to the energy in the calorimeter, appropriately corrected for zero suppression, taken at the same luminosity. This concept is at the core of the offset correction.

The total offset is measured by recording the  $E_T$  density in the calorimeter, as a function of  $\eta$  and luminosity during zero bias triggers. This density is corrected by the suppression correction and then applied to jet data. The area of the jet is determined and the correction takes the form:

$$Offset = (D_{zero}^{supp} + supp\_corr + D_{pue}) \times area.$$
 (4.3)

In Equation 4.3, supp\_corr is the suppression correction defined above and  $D_{pue}$  is the *physics underlying event* correction defined below.

#### 4.4.2 Physics Underlying Event Correction

To study physics underlying event, min bias data is studied. The assumption is made that at sufficiently low luminosity, a min bias event is a soft  $p\bar{p}$  scatter which roughly corresponds to the type of interaction associated with underlying event. The energy density measured in this type of data also reflects electronic noise, although low luminosity assures that most other types of noise are not present. In order that the noise is not counted twice, it is subtracted from the underlying event data. The noise is modeled in this case by low luminosity zero bias data. The  $E_T$  density due to physics underlying event in this model is presented in Figure 4.20. The measured physics underlying event is not smooth with respect to jet  $\eta$  as one might expect. This is due to the non-continuous nature of the DØ calorimeter, not the physics process itself. However, this is effect of the physics underlying event as seen by the DØ calorimeter, therefore it is the correction we wish to apply.

Figure 4.21 shows the total offset correction for the different luminosity bins considered in its derivation. During actual data correction, the correction applied to a jet is taken from the luminosity bin closest to the jet event. The fits shown are used to facilitate implementation.

#### Physics underlying event measured from min bias data

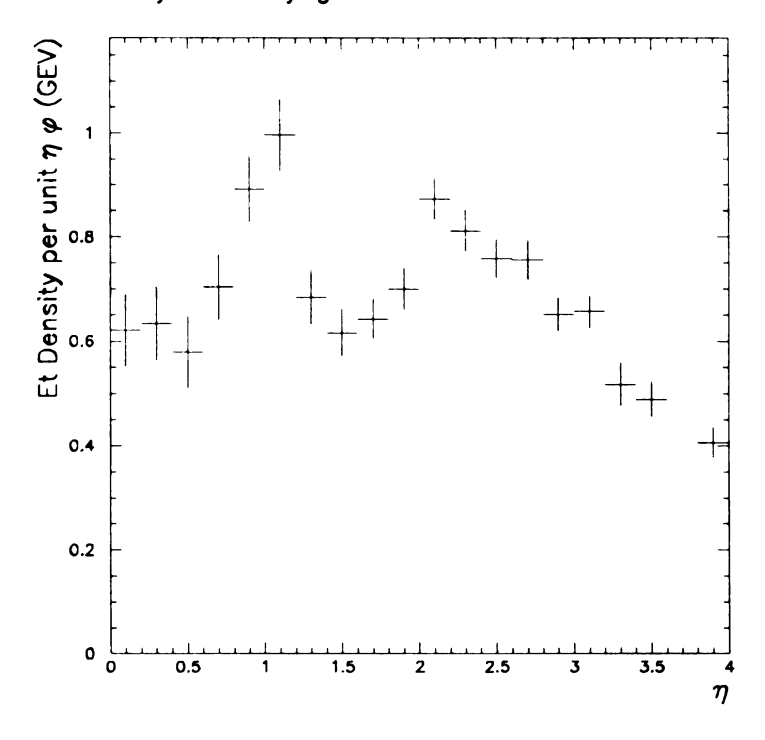


Figure 4.20: Energy density due to physics underlying event.

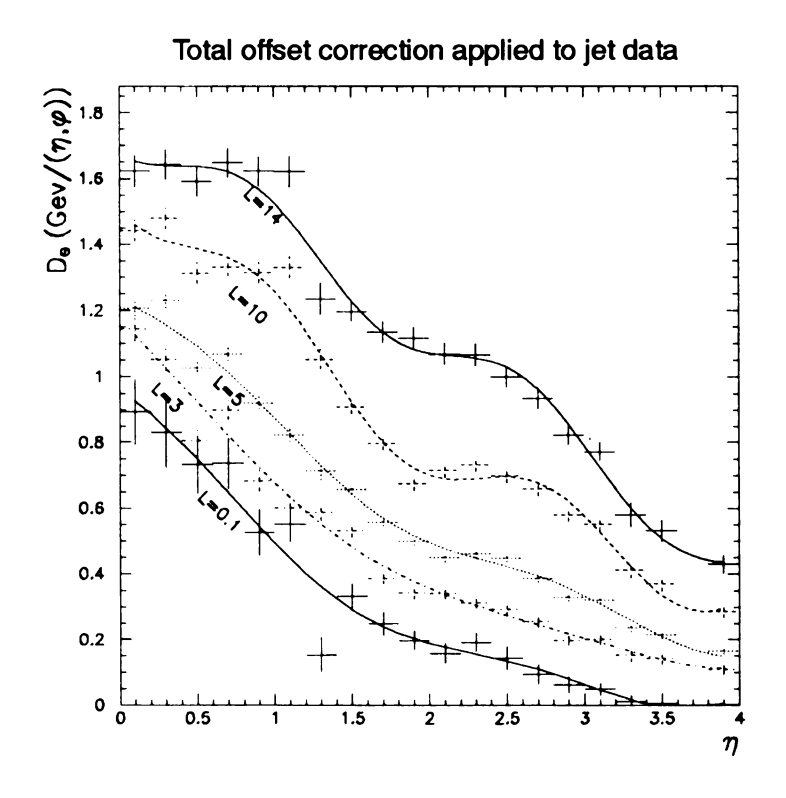


Figure 4.21: The total offset correction for different luminosity bins.

#### 4.4.3 Out of Cone Showering Correction

When a collimated stream of particles interacts with the calorimeter, some fraction of them, near the boundary which defines the jet cone, can shower outside (or inside) the jet. In order to understand this effect, actual jet data were studied. The energy between the 0.7 cone boundary and R = R' (for R' > R) is associated with, among other things, out of cone showering. R' is chosen carefully depending on the  $\eta$  bin considered. The energy measured in this annulus is due to jet out of cone showering and from particles from the jet that weren't in the jet cone to begin with. To determine the magnitude of the latter component, which has been called *physics* out of cone, Herwig Monte Carlo data are studied. The energy in the same annulus in Herwig is entirely due to physics out of cone because at the particle level, there has been no interaction with the calorimeter. Once these measurements are made, the out-of-cone showering is parameterized as a function of jet energy for different rapidity regions. A generous error is associated with the showering correction, especially in the forward region where the physical space spanned by a R=0.7 cone is smaller than in the central region. More details regarding the showering correction can be found in [11]. We present the results of the showering correction in Figure 4.22 in which we plot the out-of-cone showering energy correction factor (S) applied to a cone jet with radius R = 0.7. The error band is the total error associated with the correction. The correction has a larger effect in the forward region, with a larger error. We present results for jets of pseudo-rapidity between  $\eta=0$  and  $|\eta|=3.0,$ though the jets in this analysis are all within  $|\eta| = 2.0$ , for completeness.

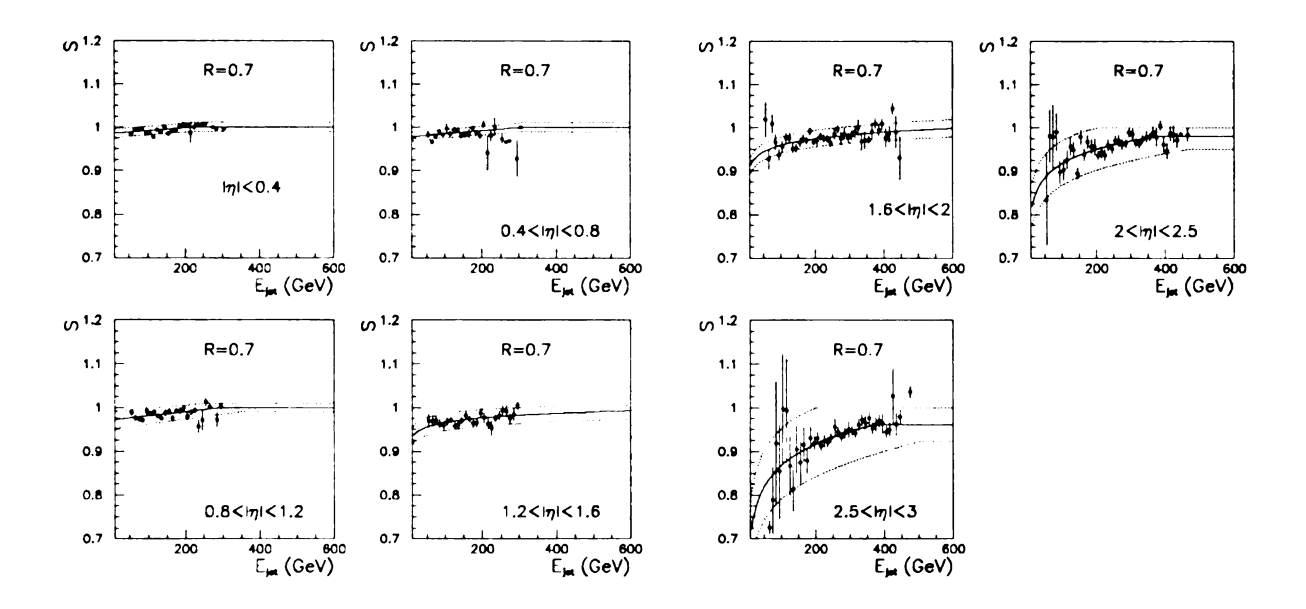


Figure 4.22: The out-of-cone showering energy correction factors (S) and errors for different  $\eta$  bins.

### 4.4.4 The Response Correction

The largest component of the energy scale correction is the response correction. Test beam data were studied in order to provide a mapping between single particle energies of known energy and the energy measured in the DØ calorimeter. The single particle response therefore, is expected to be close to unity. The response for jets however, can deviate from unity due to many effects. The average response for the actual calorimeter is not necessarily the same as the cells used during the test beam, or the jet could deposit its energy in a poorly instrumented region of the calorimeter. In any event, one cannot assume jet response of unity. In order to measure the jet response of the DØ calorimeter, photon + jet events were studied. The photon response of the DØ detector is quite good\*\*; we make use of  $P_T$  conservation in photon-jet events to study jet response. However, in an actual photon+jet event,

<sup>\*\*</sup>The photon energy scale is set by the Z mass.

imperfect jet response is responsible for introducing missing  $E_T$  into the event. To properly account for this, the missing  $P_T$  fraction (MPF) method, defined below, is employed.

In an ideal detector, during a photon + one jet event, the vector sum of the photon and the jet energy would be zero.

$$\vec{E}_{T\gamma} + \vec{E}_T^{jet} = 0 \tag{4.4}$$

However if imperfect response and the resulting  $\not\!\!E_T$  is considered, Equation 4.4 takes the form

$$R_{em}\vec{E}_{T\gamma} + R_{iet}\vec{E}_{T}^{jet} = -\vec{E}_{T}. \tag{4.5}$$

Where  $R_{jet}$  is the jet response and  $R_{em}$  is the electromagnetic response. Solving Equation 4.5 for the jet response yields<sup>††</sup>

$$R_{jet} = 1 + \frac{E_T \cdot \hat{n}_{T\gamma}}{E_{T\gamma}}.$$
 (4.6)

The response error is correlated between  $E_T$  points because the response is measured at several different  $E_T$  values, and is then fit with a function; the errors associated with this fit are correlated among  $E_T$  points. This correlation matrix is presented in the Cafix 5.1 documentation[11]. The response was fit with a variety of functions and the fits were studied to determine the error and the  $E_T$  correlations of the response correction. The response together with the nominal fit and error band is presented in Figure 4.23. Response data are included from the central calorimeter

<sup>&</sup>lt;sup>††</sup>After photon energy scale correction,  $R_{em} = 1.0$ 

(CC) the end-cap calorimeters (EC) and inter-cryostat region (IC).

The different corrections and errors associated with the energy scale are applied to the jets in this analysis; the net effect of the energy scale correction is to increase the measured jet energy by 15 - 20%.

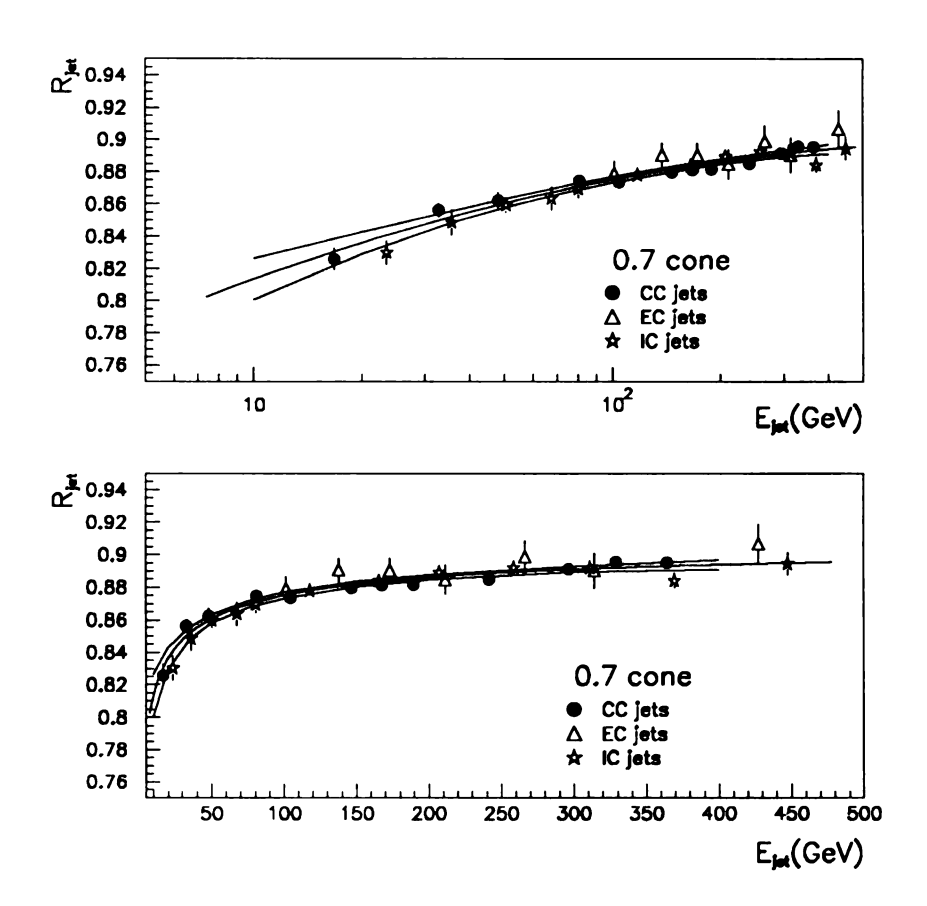


Figure 4.23: The jet response for jets in the DØ calorimeters, the fits and error bands are discussed in the text. The data are identical, the top plot has a log(x) axis to highlight the low  $E_T$  region.

## 4.4.5 Energy Scale Closure Tests

To test the effectiveness of the energy scale correction, Herwig jet events are again studied. The ratio of calorimeter jet energy,  $E_{jet}$ , to particle jet energy,  $E_{part}$ , is

studied as a function of particle jet  $\eta$ . The entire energy scale correction is derived from and re-applied to, the same Monte Carlo sample. The results, Figure 4.24, show good closure and enforce the energy scale results to  $|\eta| = 2.5$ .

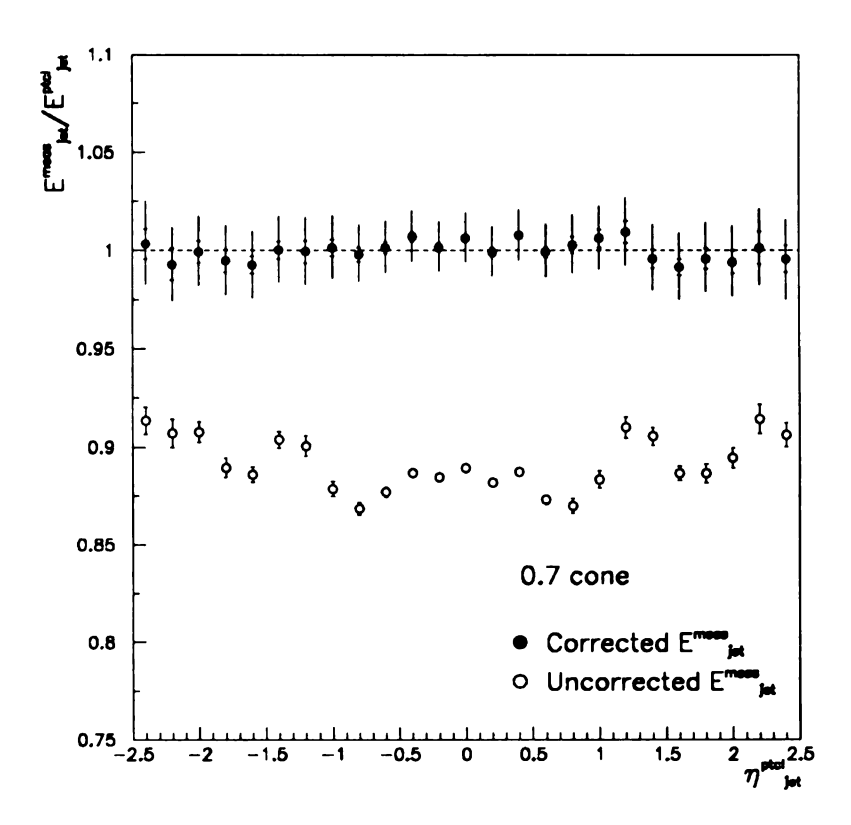


Figure 4.24: Energy scale Monte Carlo closure test.

## 4.4.6 Energy Scale Error

A full treatment of the energy scale errors is left until Chapter 6. However, we introduce the various sources of error associated with the energy scale correction and present one method of estimating the magnitude of the total energy scale error on the measured cross sections. Each component of the energy scale correction introduces some error. The offset correction incorporates an error associated with underlying event measurement and the effect of zero suppression on the data. The

showering correction has slightly larger error associated with it. Jets at DØ are required to have a minimum of 8 GeV  $E_T$ , this requirement introduces a bias in the measurement of the MPF (described earlier in this chapter) at low  $E_T$ , this introduces an error as well. Additionally, the MPF introduces other errors, an error associated with the photon energy scale, an error associated with the photon background subtraction, and additional systematic biases associated measurement of the response. These errors are tabulated in Chapter 6 and described in detail in the CAFIX 5.1 documentation[11]. We present a summary of the sources of error associated with the energy scale correction in Tables 4.5 through 4.7.

source	magnitude	comment
offset correction	.5  o 0%	decreases with $E_T$
showering correction	1.0%	essentially flat in $E_T$
low $E_T$ bias	$10 \rightarrow 0\%$	zero above 20 Gev
photon selection+background	.5 %	flat in $E_T$
response correction	2 - 3%	largest at low and high $E_T$

Table 4.5: Sources of energy scale correction errors for central ( $\eta \sim 0.0$ ) jets. The fractional errors are with respect to jet  $E_T$ .

source	magnitude	comment
offset correction	.5  o 0%	decreases with $E_T$
showering correction	2.0%	essentially flat in $E_T$
low $E_T$ bias	$10 \rightarrow 0\%$	zero above 20 Gev
photon selection+background	.5 %	flat in $E_T$
response correction	~ 2%	largest at low and high $E_T$

Table 4.6: Sources of energy scale correction errors for central ( $\eta \sim 1.2$ ) jets. The fractional errors are with respect to jet  $E_T$ .

source	magnitude	comment
offset correction	$.5 \rightarrow 0\%$	decreases with $E_T$
showering correction	4.0%	essentially flat in $E_T$
low $E_T$ bias	$10 \rightarrow 0\%$	zero above 20 Gev
photon selection+background	.5 %	flat in $E_T$
response correction	0 - 3%	largest at high $E_T$

Table 4.7: Sources of energy scale correction errors for forward ( $\eta \sim 2.0$ ) jets. The fractional errors are with respect to jet  $E_T$ .

We include the total energy scale jet energy correction factors and errors for central ( $\eta \sim 0.0$ ), inter-cryostat, ( $\eta \sim 1.2$ ) and forward ( $\eta \sim 2.0$ ), jets in Figure 4.25. These errors are with respect to jet  $E_T$ . The errors this introduces into the c ross section is discussed next.

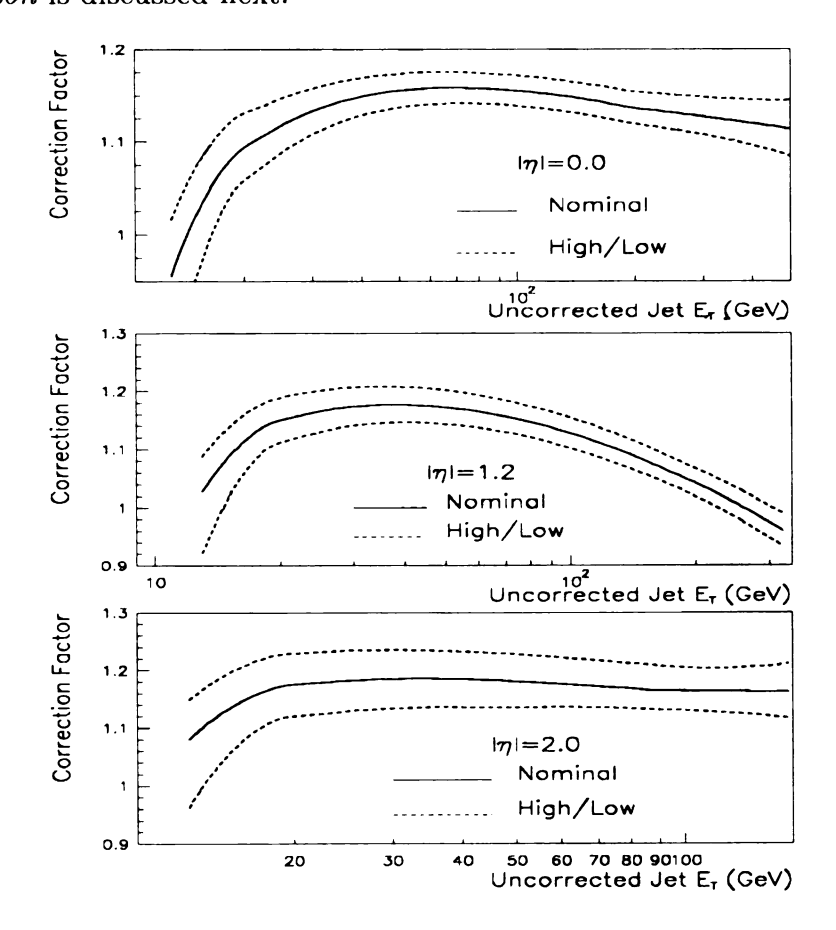


Figure 4.25: Energy scale energy correction factors for jets of different rapidity.

# 4.4.7 Cross Section Energy Scale Error Estimation from Data

We have presented the error associated with the energy scale correction on the energy of a jet. For purposes of this analysis, the error on the cross section associated with the energy scale is needed. One estimation of the error associated with the energy scale corrections is defined by allowing each correction to deviate  $1\sigma$  up and down from its nominal value. The cross sections are re-derived with these components to define the total energy scale error on the cross section. We recast the Triple Differential with these high and low energy scale corrections to determine the error on the analysis associated with the energy scale. We fit the data points with a second degree polynomial in order to smooth the statistical fluctuations and ease implementation. This approach assumes the components of the energy scale error due to each individual correction are not correlated. We present the error on the measurement of the Triple Differential associated with the energy scale derived in this manner, along with the energy scale correction factors in Figures 4.26 and 4.27.

This result will be compared with the full treatment of the errors discussed in Chapter 6.

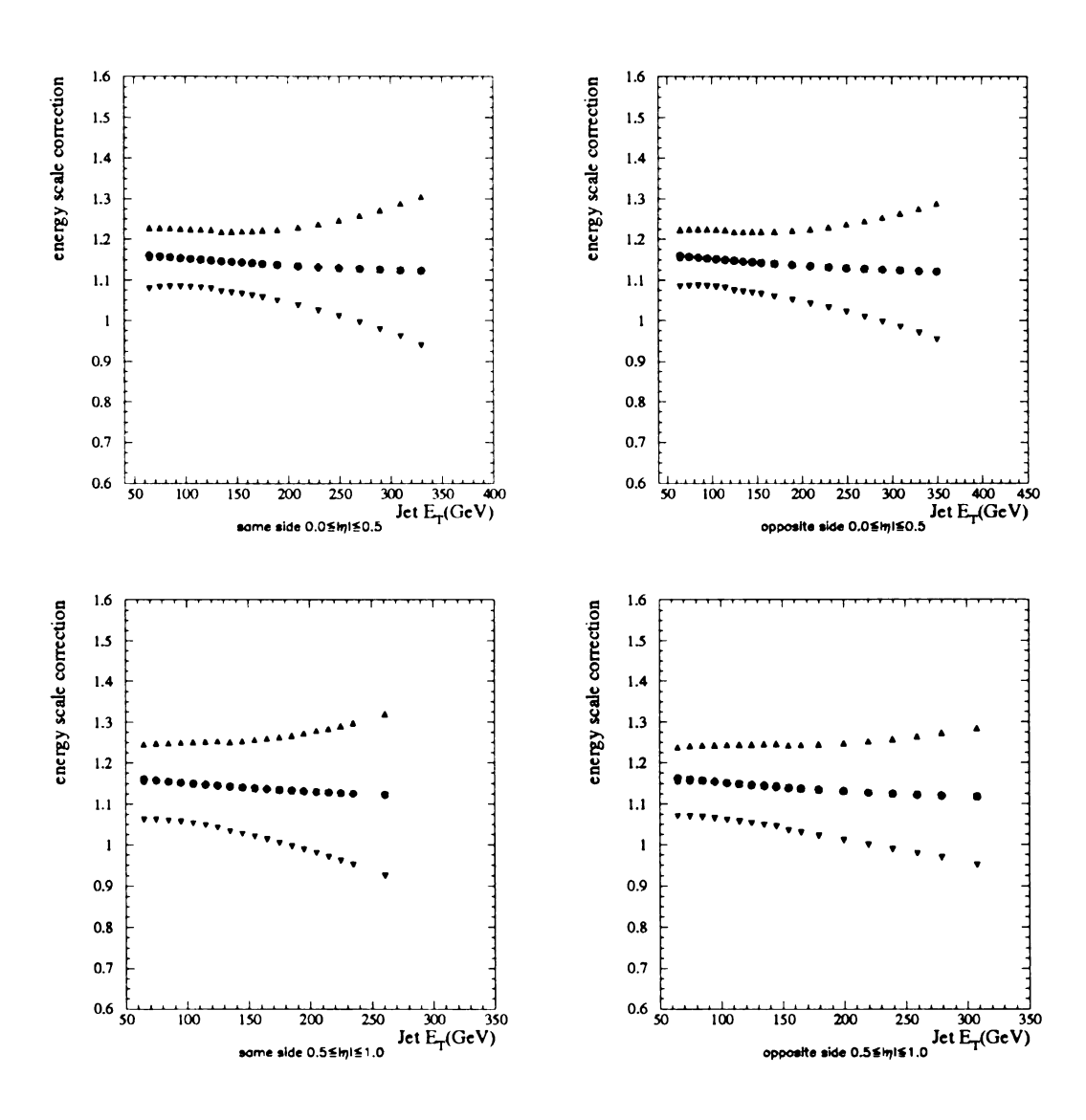


Figure 4.26: Energy scale factors to the cross sections and errors for slices 1 and 2.

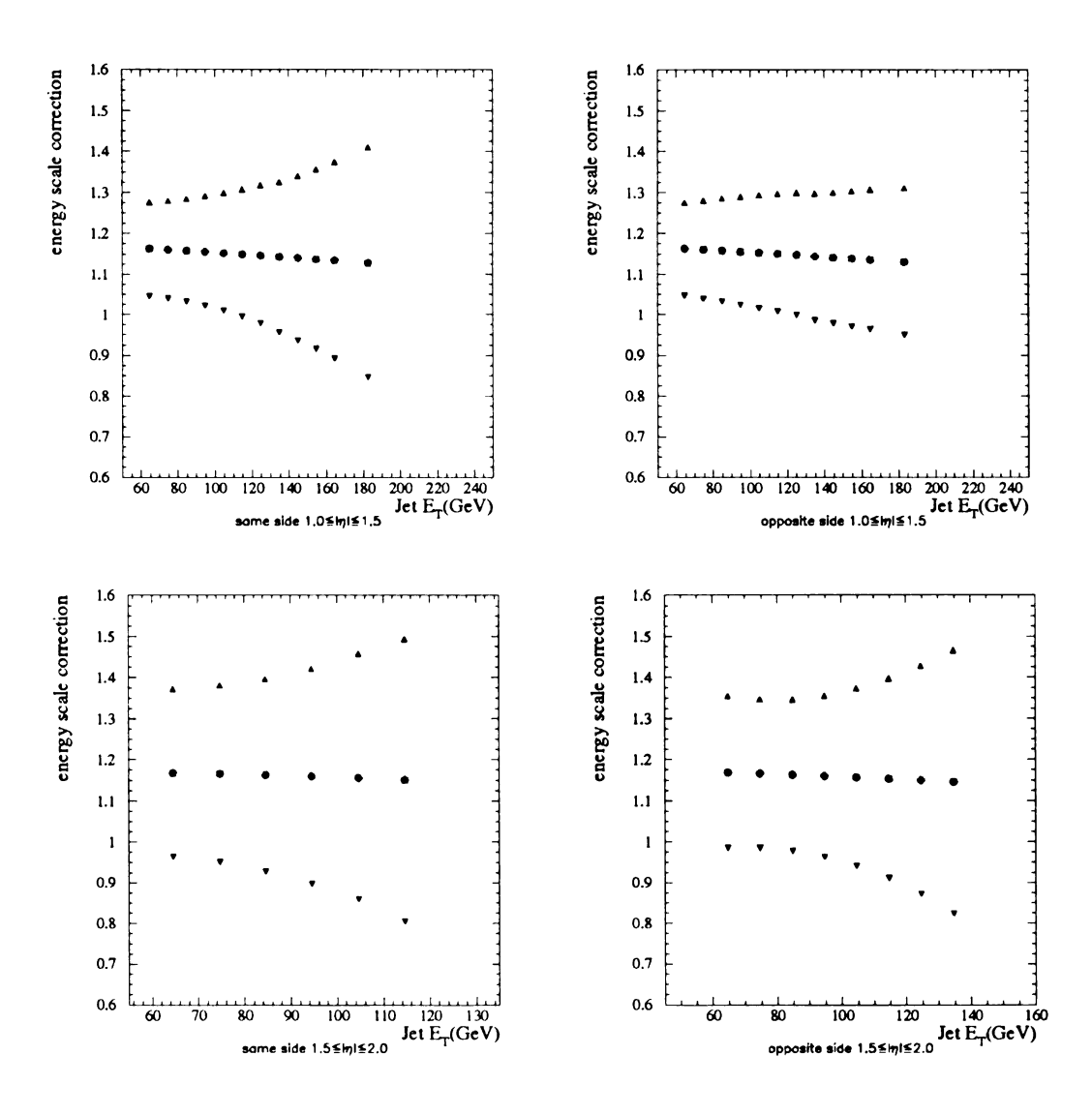


Figure 4.27: Energy scale factors to the cross sections and errors for slices 3 and 4.

Now that we have an energy scale corrected collection of good jet events, we proceed with measuring the cross sections. The next obstacle involves the imperfect energy resolution of the DØ calorimeter and its effect on the measurement of the cross sections. The jet energy scale correction assures that the average value for a measured jet is equal to the energy of the particle jet. However, due to statistical fluctuations, the measured jet energy is sometimes higher or lower than the actual value. If one were to look at the difference between the particle and calorimeter jet energy after energy scale corrections, a Gaussian distribution, centered on zero, would result. We refer to the fact that there are many more low energy jets than high energy jets as a steeply falling characteristic of the jet cross section. Because of this steeply falling nature, it is not enough that the average measurement of the energy produces the right result, the width of the  $E_T$  distributions, the jet energy resolutions, affects the measured cross sections. We present a method to correct the measurement for this effect, based on a measurement of these resolutions, in the next chapter. We will also see another detector effect while measuring the resolutions and present a method to correct for that as well.

At this stage, we present the raw cross sections, Figure 4.28, which have been energy scale corrected, additionally the corrections derived thus far have been applied.

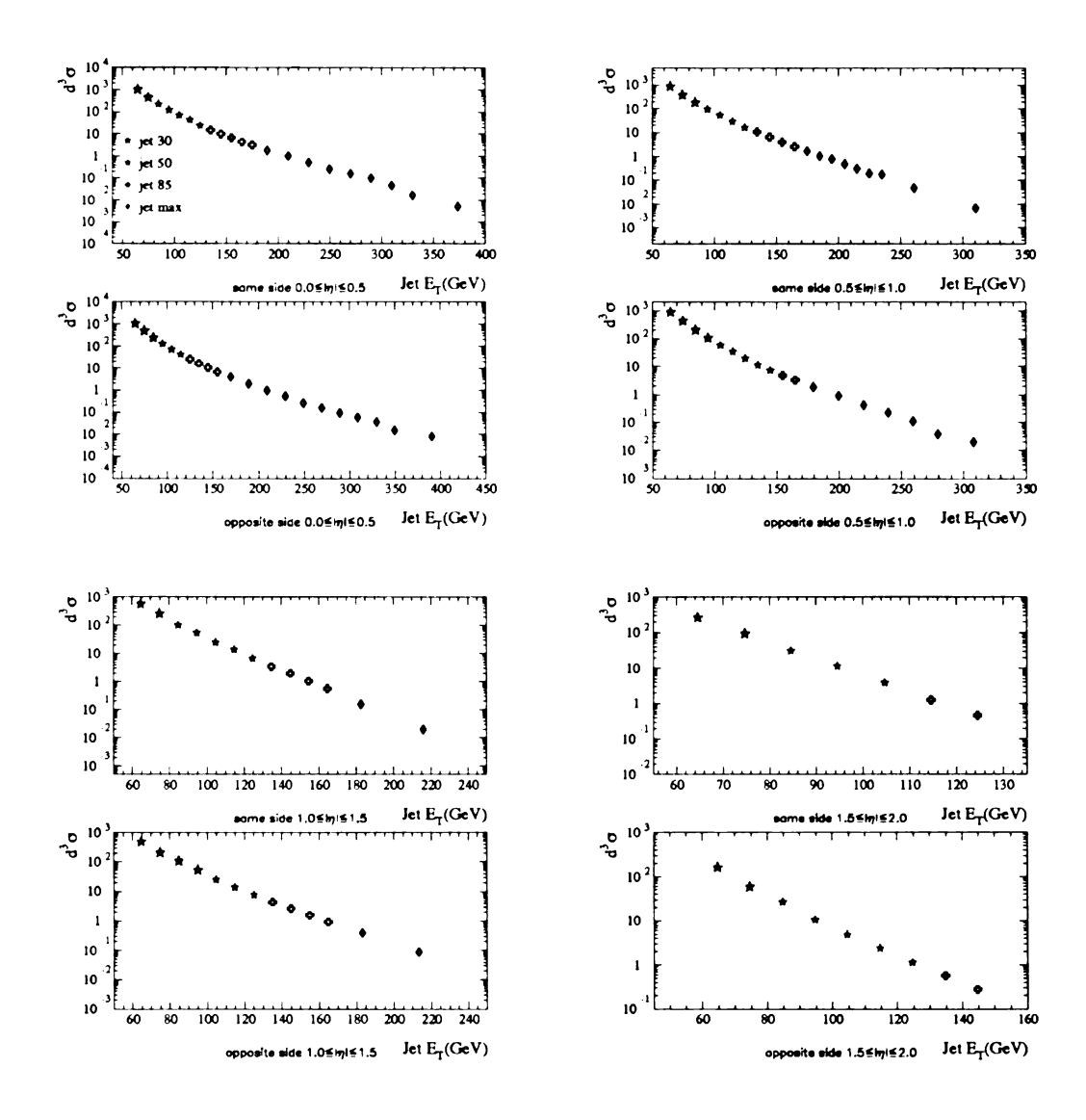


Figure 4.28: The eight slices that make up the raw Triple Differential cross section, the units of the cross sections are picobarns.

# Chapter 5

# Resolutions and Unsmearing

As described in Chapter 4, imperfect jet energy resolution changes the shape of, or smears, the measured cross section. In the cross sections measured here, there are many more jets at low  $E_T$  than at higher  $E_T$ . Let us consider one bin of a cross section at  $E_T^0$ , called bin a, and the bin immediately to its right at  $E_T^{1\dagger}$ , bin b. The fact that the jet energy resolution of the DØ calorimeter is not perfect means that some fraction of events in bin a will fall into bin b and vice-versa. However, because of the steeply falling nature of jet cross sections, there are many more events in bin a than in bin b. Therefore, though the fraction of each bin that falls into the other is the same for both, many more events will migrate from bin a to b than the other way around. The net effect is to increase, or smear up, the cross section in bin b. Since every bin in a cross section has a bin to the left of it<sup>‡</sup>, every bin is affected by  $E_T$  smearing.

<sup>&</sup>lt;sup>†</sup>Here we assume  $E_T^1 > E_T^0$ .

<sup>‡</sup>This assumes that the bin at  $E_T = 0$  is not counted as part of the cross section, a valid assumption for the Triple Differential which begins counting events at  $E_T = 60.0 \ GeV$ .

In this chapter, we describe the process of correcting for this effect, referred to as unsmearing.

# 5.1 Jet Energy Resolutions

The main experimental ingredient needed during the unsmearing procedure is an understanding of the jet energy resolution. That is, the width of the distribution defined by

(actual jet 
$$E_T$$
- measured jet  $E_T$ ),

which we define as  $\sigma_{E_T}$ , vs. measured jet  $E_T$ . Historically, what is usually measured are the fractional energy resolutions, defined as  $\frac{\sigma(E_T)}{E_T}$ .

This number is determined using the di-jet asymmetry method outlined in [17].

The asymmetry is measured from actual di-jet data and is defined as

$$A = \frac{E_{T_1} - E_{T_2}}{E_{T_1} + E_{T_2}}. (5.1)$$

The jets in the sample used to define the asymmetry have been corrected using Cafix 5.1.

A little algebra convinces us that we can use the asymmetry to get the jet energy resolutions, that is that [17]

$$\frac{\sigma_{E_T}}{E_T} = \sqrt{2}\sigma_A. \tag{5.2}$$

Where  $\sigma_A$  is the width of the asymmetry distribution and  $\sigma_{E_T}$  is the width of the jet

energy resolution and we have assumed  $E_{T_1} = E_{T_2}$ . These asymmetries are studied as a function of  $E_T$  separately for all the pseudo-rapidity bins considered in this analysis. We include one actual asymmetry distribution in Figure 5.1, overlaid with a Gaussian fit, for illustration.

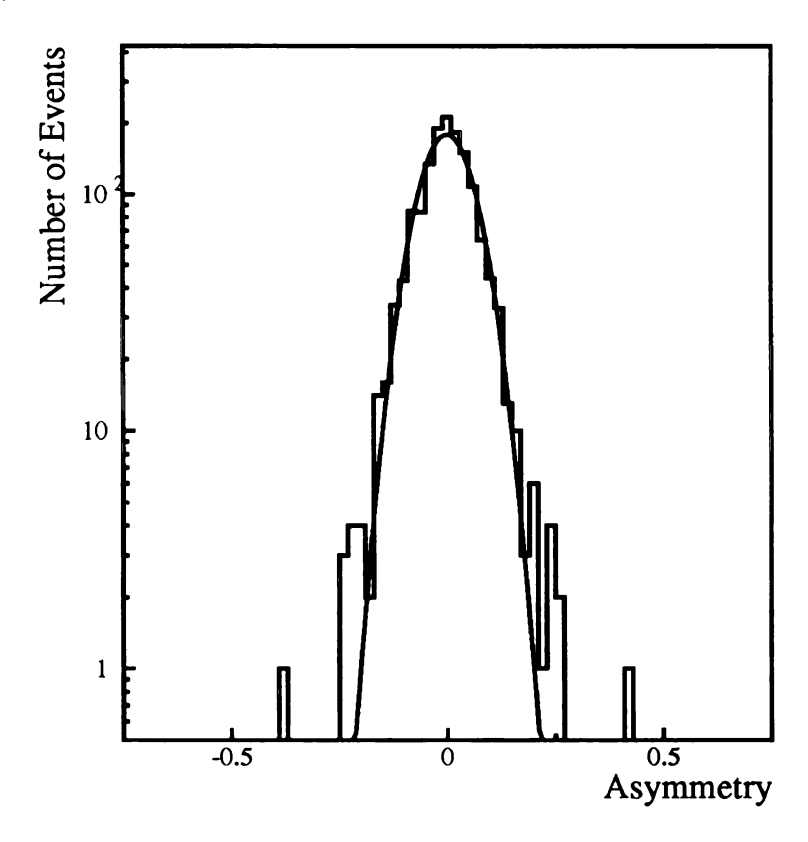


Figure 5.1: An example of an asymmetry distribution, together with a Gaussian fit.

#### 5.1.1 Soft Third Jet and Particle Out of Cone Corrections

The data from which the di-jet asymmetry is measured contain many events with more than two jets. To deal with this, the asymmetry variable is calculated for a variety of data sets with increasingly restrictive cuts on the  $E_T$  of the third jet in the event. The result is extrapolated to the ideal case in which the  $E_T$  of the third jet is equal to zero to measure the resolution of an ideal two jet system. Examples of this extrapolation for four different  $E_T$  bins are presented in Figure 5.2 in which

the measured resolutions for the bin  $1.0 < |\eta| < 1.5$  are presented for 4 soft third jet cuts together with the point extrapolated to  $E_{T_3} = 0$ .

Because of particles not contained in the jet cone,  $\sigma_A$  may be non-zero even at the particle level. To remove this effect, the asymmetry variable is calculated for particle level Monte Carlo jets as well; this number is then subtracted from the calorimeter level asymmetry measured from jet data. In this manner, the method is sensitive only to the detector energy resolution of the two jet system.

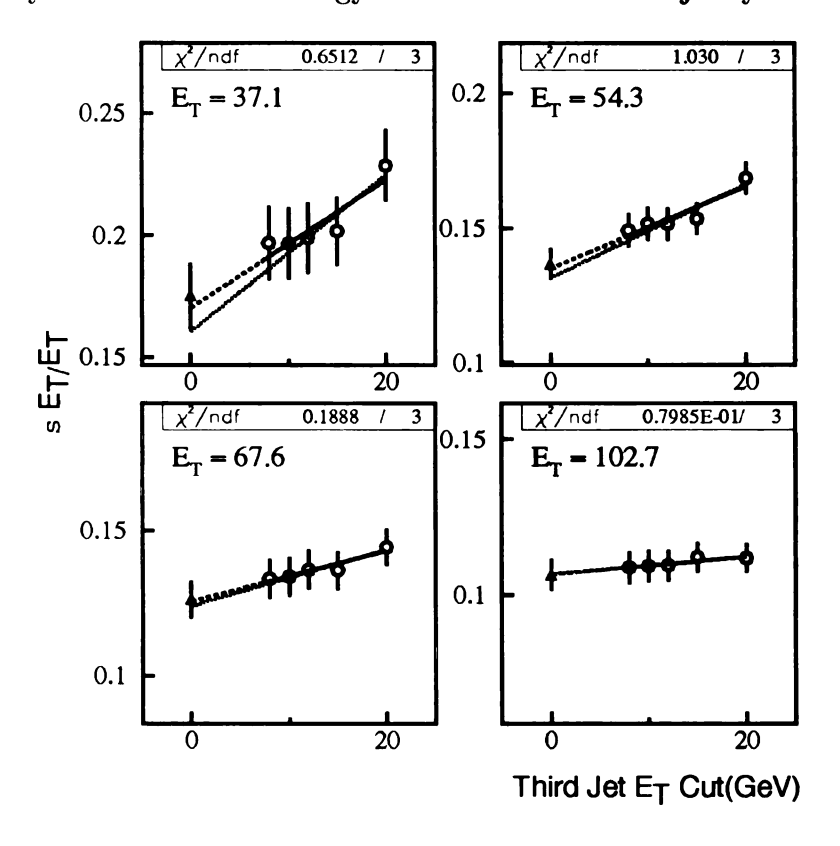


Figure 5.2: Example of the third jet cut extrapolation.

The resolutions before the particle corrections together with the measured particle jet resolutions are presented in Figures 5.3 and 5.4, for central and forward jets, same and opposite side. The data are fit to a second order polynomial; the results of these fits appear in the figures. The three fit parameters are historically called C, S and N.

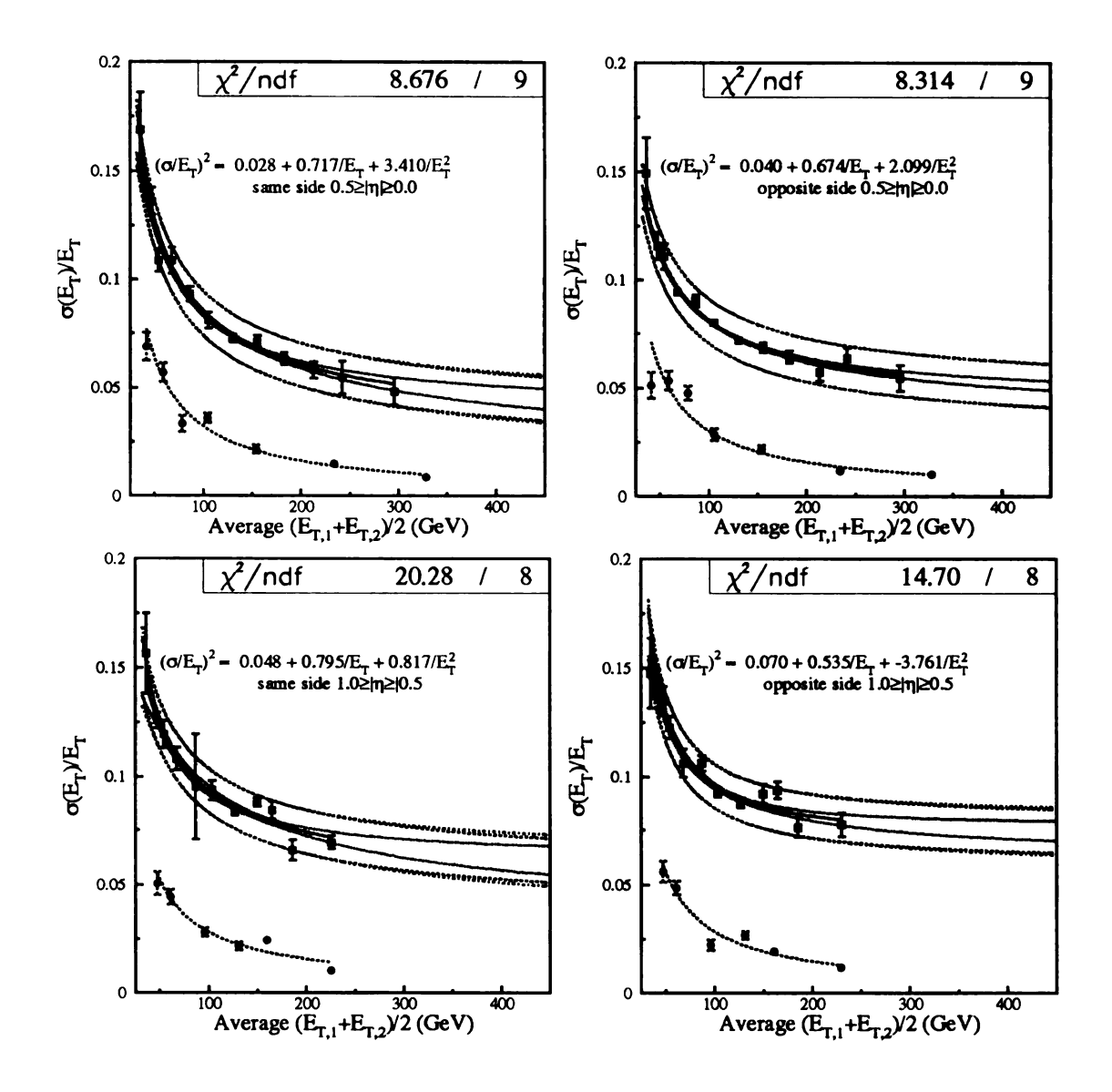


Figure 5.3: Fractional jet energy resolutions for two central slices, same and opposite side, before the particle correction, together with the particle level resolutions (the lower curve). The outer error bands define the systematic error due to closure, the inner bands are due to fitting errors. These errors are discussed in detail later in this chapter.

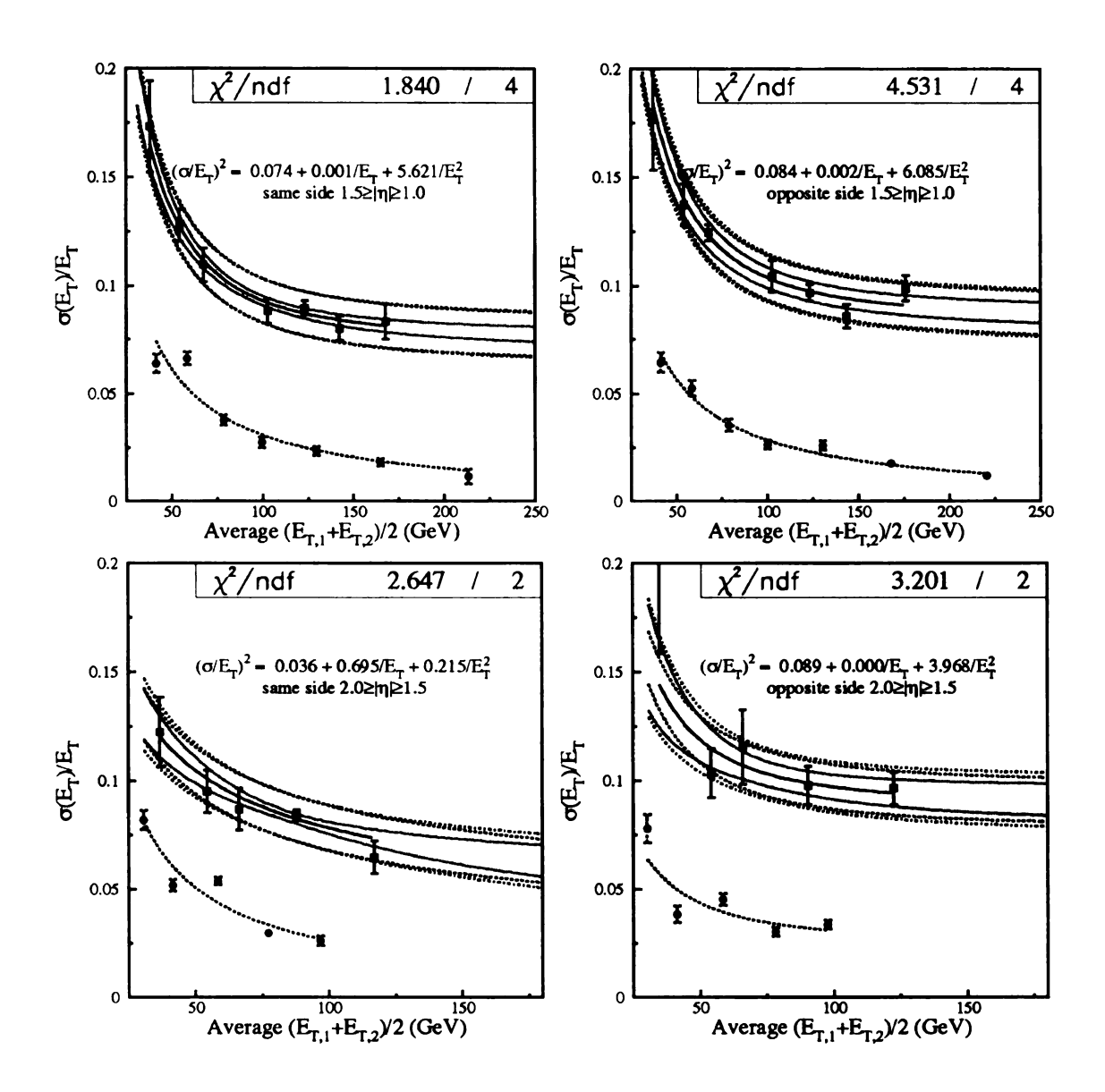


Figure 5.4: Fractional jet energy resolutions for two forward slices, same and opposite side, before the particle correction, together with the particle level resolutions (the lower curve). The outer error bands define the systematic error due to closure, the inner bands are due to fitting errors. These errors are discussed in detail later in this chapter.

These resolutions, shown in Figures 5.3 and 5.4, are studied as a function of  $E_T$  separately for all the pseudorapidity bins considered in this analysis. It should be noted that the di-jet events used in the resolution study, like the events in the triple differential cross section, can be divided into two classes: events with two jets on the same side of the detector and events with two jets on opposite sides of the detector. While measuring the asymmetry from di-jet events it was observed that the asymmetry from the opposite side distributions was wider than the corresponding same side resolutions. The asymmetry is sensitive to the jet energy resolution, but it can, in principle be sensitive to other effects as well. The conclusion is that there is another effect present.

#### 5.1.2 Vertex Position Resolution and Di-Jet Asymmetry

It has been shown[21] that while measuring the resolution with the asymmetry from a same side sample produces the correct relation between asymmetry and jet energy resolution, the opposite side configuration is sensitive to the effect of vertex position resolution as well. The DØ detector has vertex position resolution on the order of 1cm which is not large enough to account for the differences seen between the same and opposite side asymmetries. However, for some events in the sample, the reconstruction software finds more than one vertex. From the distributions of the distance between the two vertices for the case when more than one is found (Figure 5.5) it can be observed that the difference is very rarely less than 10cm. The conclusion is that the DØ detector together with the DØ reconstruction software cannot distinguish vertices if they are too close together. This leads to the idea of

effective vertex position resolution; the effect observed in the measurement of the di-jet asymmetries. In Table 5.1, we present the fraction of events with 1 vertex found to all events in each slice. We can see as one moves forward, it is less likely to find more than one vertex. However, there is no physics reason to expect more events with only one vertex which produce jets in the forward region. This being the case, it is expected that the effective vertex position resolution is worse in the forward region as it is more likely that two different vertices are not resolved there.

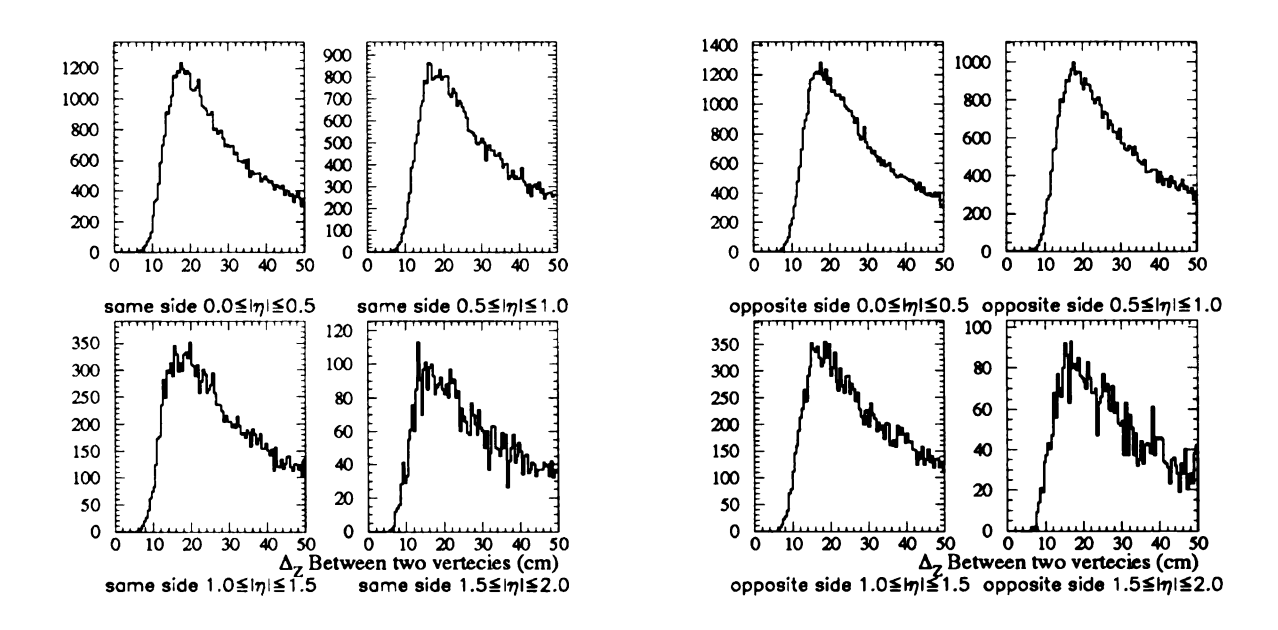


Figure 5.5: The difference between vertices in events where more than one is found, for all slices of the Triple Differential.

Fortunately, the effect manifests itself in the measurement of the asymmetries in a predictable way. We begin with the asymmetry:

$$A = \frac{E_{T1}^{meas} - E_{T2}^{meas}}{E_{T1}^{meas} + E_{T2}^{meas}}. (5.3)$$

In Equation 5.3,  $E_T^{meas}$  is the measured jet energy which we can express as the true

$\eta$ bin	SS or OS	fraction of single vertex events
0.0 - 0.5	SS	0.57
0.0 - 0.5	OS	0.57
0.5 - 1.0	SS	0.57
0.5 - 1.0	OS	0.57
1.0 - 1.5	SS	0.62
1.0 - 1.5	OS	0.59
1.5 - 2.0	SS	0.70
1.5 - 2.0	OS	0.66

Table 5.1: Fraction of single vertex events for all slices.

jet energy  $E_T^{true}$  affected by imperfect resolution. That is:

$$E_T^{meas} = E_T^{true} \left(1 + \frac{\sigma_{E_T}}{E_T}\right). \tag{5.4}$$

We now recall  $E_T = Esin(\theta)$  so that

$$A = \frac{E(1+r_1)sin(\theta_1) - E(1+r_2)sin(\theta_2)}{E(1+r_1)sin(\theta_1) + E(1+r_2)sin(\theta_2)}.$$
 (5.5)

In Equation 5.5,  $\theta_1$  and  $\theta_2$  are the two jet angles and we have defined  $r = \frac{\sigma_{E_T}}{E_T}$ , the jet energy resolution. If the vertex is now displaced by some small amount,  $\delta z$ ,  $\theta_1$  and  $\theta_2$  will be affected. We start with:

$$tan\theta_T = R/Z \tag{5.6}$$

where  $\theta_T$  is the *true* angle, Z is the position of the jet along the z axis, and R is the distance between the jet and Z axis.

For central jets, R is considered a constant;  $R_{cc} \approx 91 \text{ cm}^{\S}$ . For forward jets, the

<sup>§</sup>These variables are pictured in Figure 5.6.

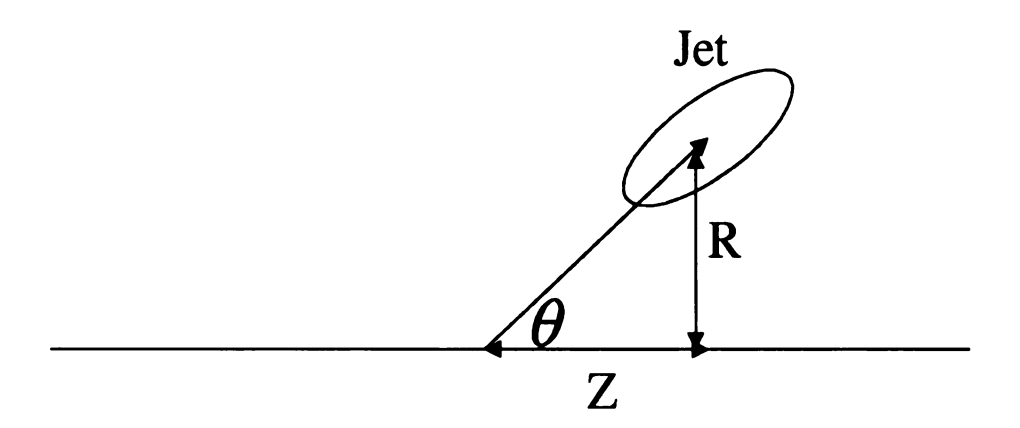


Figure 5.6: Variables used in the calculation of the effect of vertex resolution.

hypotenuse in the figure is a constant, equal to  $\approx 178 \, cm$ , however,  $R_{ec}$  is not, it depends on the jet angle.

Now if we modify Z by  $\pm \delta(Z)$ , Equation 5.6 takes the form:

$$tan\theta_{M} = \frac{1}{\cot\theta_{T} - \frac{\delta Z}{R_{cc}}} \tag{5.7}$$

for jets in the CC and:

$$tan\theta_M = \frac{1}{\cot\theta_T (1 - \frac{\delta Z}{R_{ec}})} \tag{5.8}$$

**for** jets in the EC. In Equations 5.7 and 5.8,  $\theta_M$  refers to the *measured* angle. If we

solve for  $sin\theta$  and expand in  $\frac{\delta Z}{R}$ , we obtain  $\P$ :

$$sin\theta_M \approx sin\theta_T (1 + cos\theta_T sin\theta_T (\frac{\delta Z}{R_{cc}}))$$
 (5.9)

and

$$sin\theta_M \approx sin\theta_T (1 + cos^2 \theta_T (\frac{\delta Z}{R_{ec}})).$$
 (5.10)

For the same side case, where  $\theta_1 \sim \theta_2$  the asymmetry now reduces to [21]

$$A = \frac{(r_1 - r_2)}{(1 + r_1) + (1 + r_2)}$$

from which one can extract[17]

$$\langle A_{SS}^2 \rangle = \frac{r^2}{2}.$$
 (5.11)

In the case of opposite side jets, the algebra is much more complicated. If we use Equation 5.10 and 5.9 for  $sin\theta$ , we obtain,

$$\langle A_{OS}^2 \rangle = \frac{r^2}{2} + (\frac{\sigma_z}{R_{ec}})^2 cos^4 \theta$$
 (5.12)

for the jets in the EC and

$$\langle A_{OS}^2 \rangle = \frac{r^2}{2} + \frac{1}{4} (\frac{\sigma_z}{R_{cc}})^2 sin^2 2\theta$$
 (5.13)

for jets in the CC.

<sup>¶</sup>Different results are obtained in the central region and the forward region because  $R_{ec}$  is a constant with respect to the jet angle while  $R_{cc}$  is not.

In Equations 5.12 and 5.13,  $\sigma_z$  is the width of the effective vertex position resolution, it is not the vertex position resolution of the DØ calorimeter. It is the net effect of the inability of the DØ reconstruction software to distinguish between two vertices if they are sufficiently close together. It is essentially the effect of the reconstruction package choosing the wrong vertex some fraction of the time, as seen in Figure 5.5.

Fortunately, we will not need to take these results (Equations 5.11 - 5.13) at face value, we can use this prediction together with a Monte Carlo study to *introduce* a vertex position resolution into the Monte Carlo, where the vertex is known perfectly, and attempt to *extract* the vertex position resolution via Equations 5.11 - 5.13. If the input and output vertex position resolutions are in good agreement, it will check the calculations and assumptions presented above.

Figures 5.7 - 5.8 show the fractional jet energy resolution measured, using the asymmetry formalism, from SS and OS events for the four  $\eta$  bins defined in this analysis. Figure 5.9 contains the SS and OS resolutions overlaid together with their fit and systematic error bands. The systematic error band was obtained from another Monte Carlo study using Herwig with DØ zero bias data *overlaid* as discussed in appendix A.  $\sigma_Z$  is extracted by considering the difference between the two sets of resolutions, and consideration of the relation

$$< A_{OS}^2 > - < A_{SS}^2 > = (\frac{\sigma_z}{Z_{cal}})^2 cos^4 \theta$$
 (5.14)

for the CC case and

$$\langle A_{OS}^2 \rangle - \langle A_{SS}^2 \rangle = \frac{1}{4} (\frac{\sigma_z}{R_{cal}})^2 sin^2 \theta$$
 (5.15)

for the EC case.

For the case of the central  $(0.0 \le |\eta| \le 0.5)$  region, the measured asymmetries are not distinguishable. This does not imply that the effective vertex position resolution is zero there, only that the asymmetry variable is not sensitive to it. In order to estimate the effective vertex position resolution in the central bin, the results for the effective vertex position resolution were studied as a function of  $\eta$  and the measurement was extrapolated into the central bin. To estimate an error on this central measurement, the error on the measurement of the effective vertex position resolution from slice 2 is used. This result for the effective vertex position resolution together with its error analysis is included for the four slices in Figure 5.10. The effective vertex position is between 2-7.5 cm, increasing with pseudo-rapidity, with errors of 2-4 cm.

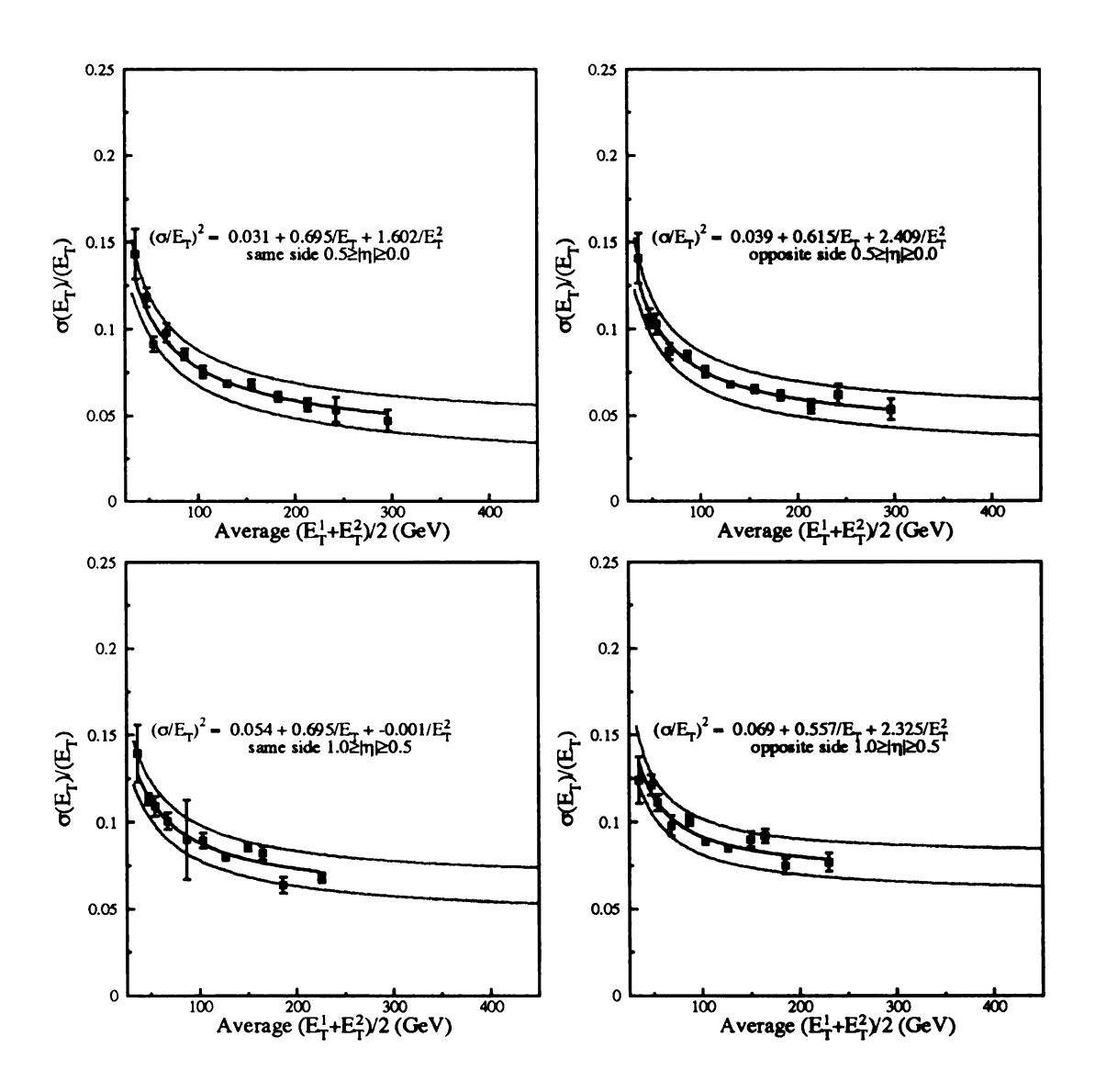


Figure 5.7: Fractional jet energy resolutions for the first two slices same and opposite side with their total fit + systematic errors.

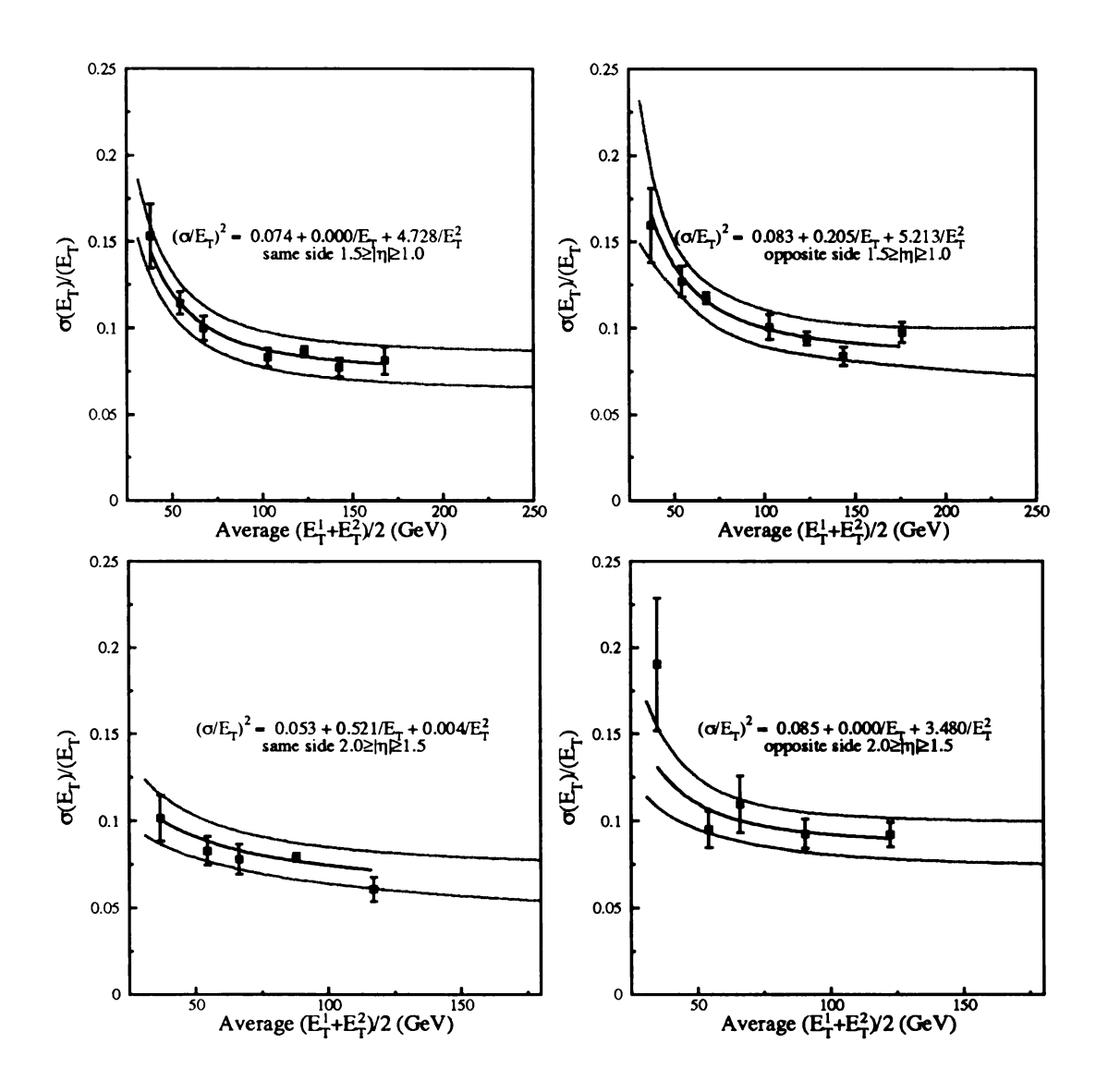


Figure 5.8: Fractional jet energy resolutions for two forward slices, same and opposite side with their total fit + systematic errors.

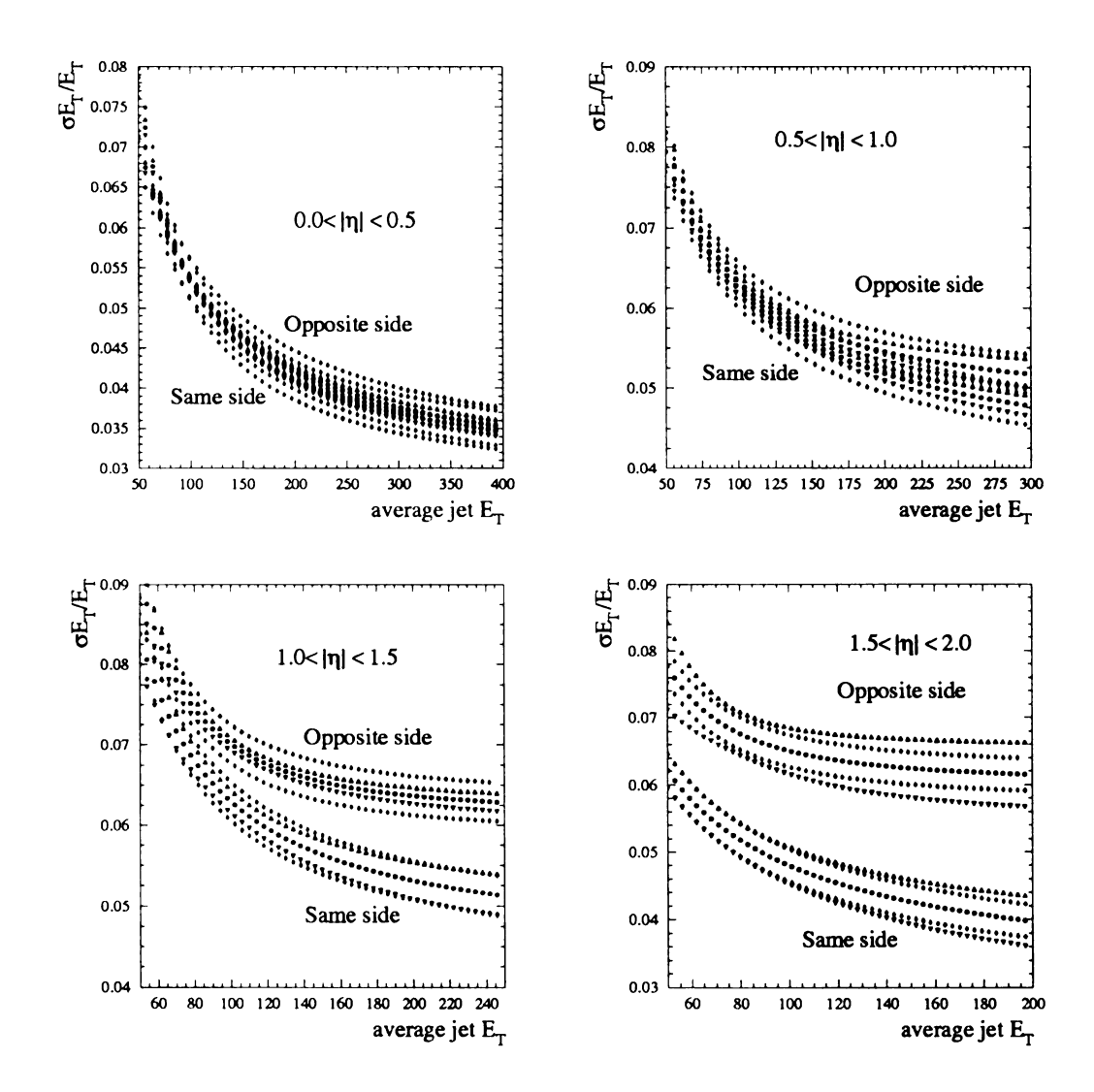


Figure 5.9: Same Side and Opposite side resolutions, with systematic(inner) and fit(outer) error bands for the four slices. Note that the central resolutions are indistinguishable.

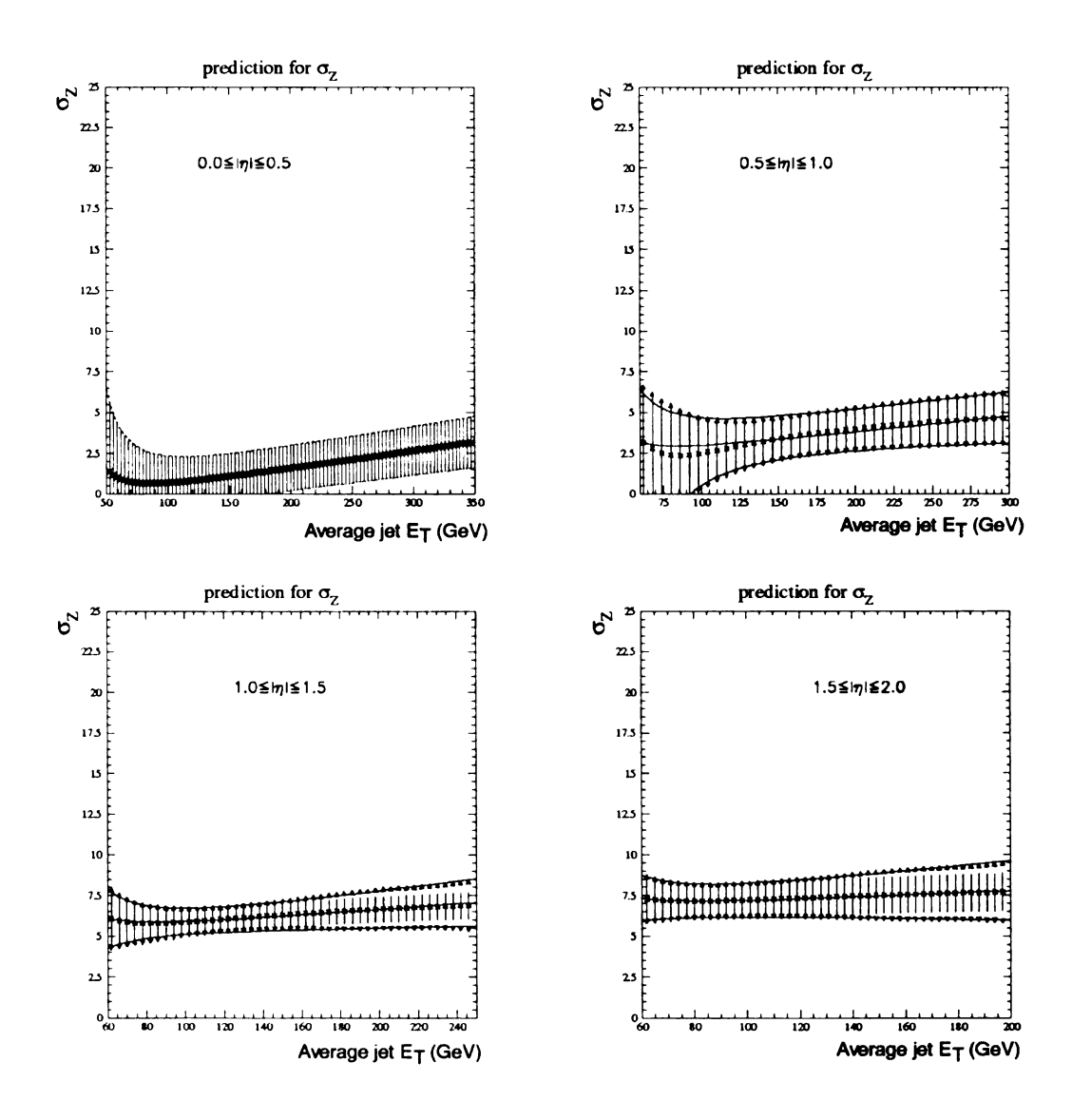


Figure 5.10: Effective vertex position resolution for all slices. The inner error is due to fitting and the outer errors are fit + systematic. The fits shown here are used to implement the vertex position resolution and its error during derivation of the Monte Carlo correction, described next.

## 5.1.3 Monte Carlo Closure of the Vertex Position Resolution Measurement

The measurement of the effective vertex position resolution can be tested with a Monte Carlo study. A Herwig sample of jet data overlaid with DØ zero bias data was studied. These data exist only in the central ( $|\eta| < 0.4$ ) and forward ( $|\eta| > 1.6$ ) regions. To test closure, the measured forward vertex position resolution was input into the most forward  $\eta$  bin defined by  $1.5 \le |\eta| \le 2.0$ . After the vertex position resolution was inserted into the Monte Carlo, the extraction described above was performed to measure the effective vertex position resolution. The input and output vertex resolutions are shown in Figure 5.11. These plots show excellent agreement within the errors and lead us to believe we have a good handle on vertex position resolution. In Figure 5.11, the forward closure plot is used as one source of error on the measurement of the effective vertex resolution; an error band is defined to accommodate the small disagreement in the closure, this error is applied to all slices.

The fact that the Herwig data with zero bias overlay only exist in the most forward and central region has presented us with a small dilemma. We have decided to apply the same closure error to all slices although this is probably an overestimate. However, we will see that this closure error is not a significant source of error in the Triple Differential so this small over-estimate is not problematic.

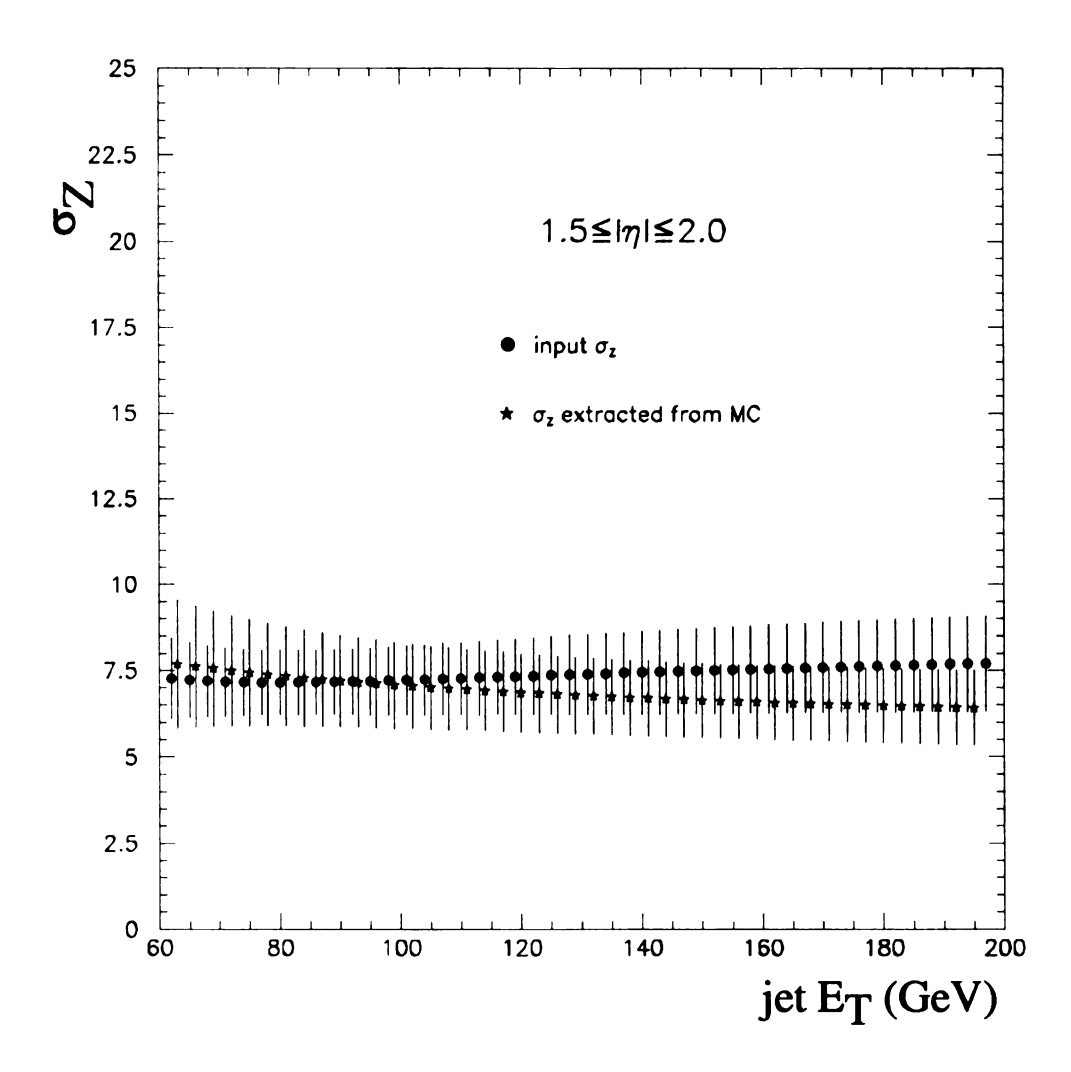


Figure 5.11:  $\sigma_Z$  extracted from MC data shown together with input vertex position resolution distribution. Errors are fit + systematic.

#### 5.1.4 The Plan

Now that the effective vertex position and its effect on the di-jet asymmetry are understood, we proceed as follows. The effect of energy resolution on the cross section (cross section smearing) is treated through use of only the resolutions measured from a sample of data with both jets on the same side of the calorimeter because this has been shown to be sensitive to only the energy resolution of the detector. The measured effective vertex position resolution together with its error is inserted into a Monte Carlo to derive a correction (and error) to apply to the data to account for effective vertex position resolution. In the next section, we outline a procedure for unsmearing the cross sections to correct them for the effect of the energy resolution of the DØ calorimeter after which we will describe the derivation of the vertex position resolution correction derived from Monte Carlo.

### 5.2 Jet Energy Resolution Results

The measured jet energy resolutions for all  $\eta$  bins appear in Figures 5.7 and 5.8. These are fully corrected for soft third jets and particle level resolutions as described in [10] and above. We will proceed by using the same side resolutions to unsmear all of the data as follows. The right hand side of Equation 5.16 is fit to the measured resolutions in order to parameterize the resolution data. The errors on C, S, and N together with the covariance matrix for these three parameters is recorded for later use in defining the unsmearing error.

$$\frac{\sigma_{E_T}}{E_T} = \sqrt{\frac{N^2}{E_T^2} + \frac{S^2}{E_T} + C^2} \tag{5.16}$$

### 5.3 Unsmearing the Data

The procedure for unsmearing follows the method outlined in a previous DØ analysis of jet data[22]. This method assumes that the unsmeared cross section can be parameterized via a functional form, or ansatz function. We further assume in this analysis that this function is flexible enough to fit all eight of the  $E_T$  distributions that make up the Triple Differential. These assumptions are critical to this approach; the validity of these assumptions will be quantified. For this analysis the ansatz used is of the form

$$F(\alpha, \beta, \gamma, \delta, E_T) = e^{\alpha} E_T^{\beta} (1 + \gamma(\frac{2}{\sqrt{s}}) E_T)^{\delta}.$$
 (5.17)

The ansatz function is convoluted with the measured resolution functions to

determine the functional form of the smeared cross sections. This convolution takes the form:

$$f(\alpha, \beta, \gamma, \delta, E_T') = \int G(E_T' - E_T) F(\alpha, \beta, \gamma, \delta, E_T) dE_T.$$
 (5.18)

Here,  $G(E_T'-E_T)$  is a Gaussian distribution with width equal to the width of the measured jet energy resolutions for jets of transverse energy  $E_T'$ . Finally, the function  $f(\alpha, \beta, \gamma, \delta, E_T')$  is fit to the measured cross sections. After a satisfactory fit is obtained, the smearing correction is defined as

$$R = \frac{f(\alpha, \beta, \gamma, \delta, E_T')}{F(\alpha, \beta, \gamma, \delta, E_T)}.$$
 (5.19)

The cross section is corrected, bin by bin, by this factor.

An error associated with the unsmearing method is derived using the relation

$$(\delta R)^2 = \frac{\partial R}{\partial i} \frac{\partial R}{\partial j} \delta i \delta j M_{ij}. \tag{5.20}$$

In Equation 5.20,  $M_{ij}$  is the correlation matrix for parameters i and j, R is the unsmearing correction factor. The quantity  $\delta i \delta j M_{ij}$  is referred to as the covariance matrix. The sum is over the four parameters that define the ansatz,  $\alpha$ ,  $\beta$ ,  $\gamma$  and  $\delta$ , and the three parameters that are used in the resolutions fits, C, S, and N. The correlations between each set of parameters  $\alpha$ ,  $\beta$ ,  $\gamma$ ,  $\delta$  and C,S, and N are assumed

The fitting is done with a CERN library routine, Minuit, sufficient precision is required such that fits have allowable  $\chi^2$ . Minuit supplies the fits, errors, and correlations between the fit parameters.

to be zero. The correlations among  $\alpha$ ,  $\beta$ ,  $\gamma$  and  $\delta$  and among C, S, and N are determined by Minuit during fitting. The derivative of the correction factor with respect to each of the parameters  $(\frac{\partial R}{\partial t})$  is determined numerically by varying each parameter, after fitting, by a sufficiently small number  $(\epsilon)$  and recalling:

$$\frac{df(x)}{dx} = \lim_{x \to 0} \frac{f(x+\epsilon) - f(x)}{\epsilon}.$$
 (5.21)

Additionally, the error on the unsmearing correction factors due to the systematic errors on the resolution measurement is also included. The resolution closure plots discussed in Appendix A provide an error band on the resolution measurement. This error can be propagated through the unsmearing correction factors by parameterizing the resolutions in the following way. Let the parameterization of  $\sigma(E_T)$  be amended to include its systematic error:

$$\frac{\sigma(E_T)}{E_T} = \sqrt{C^2 + \frac{S^2}{E_T} + \frac{N^2}{E_T^2}} + d_1 + \frac{d_2}{E_T^2}$$
 (5.22)

where  $d_1$  and  $d_2$  are the parameters which define the resolution closure. These parameters can then be treated\*\* exactly as C, S, and N except that they are nominally zero, with errors equal to the values defined in Appendix A.<sup>††</sup>

The unsmearing errors are presented in Table 5.2, notice the error due to the resolution closure is the dominant error. This closure error is fully correlated among  $E_T$  points and is usually as large or larger than the other sources of error, which may have varying degrees of correlation. Therefore the assumption is made that the

<sup>\*\*</sup>i.e. the sum in Equation 5.20 includes  $d_1$  and  $d_2$ .

 $<sup>^{\</sup>dagger\dagger}d_1 = .0024, d_2 = 14.3.$ 

total unfolding error is correlated among  $E_T$  points.

The unsmearing factors and their total systematic errors are included in Figure 5.12. The unsmearing correction factors are on the order of 15% and show a slight  $E_T$  and  $\eta$  dependence. The errors are quite small for most of the slices considered with the possible exception of the opposite side bin between  $|\eta| = 1.0$  and  $|\eta| = 1.5$ . In this bin there is a large statistical fluctuation in the data which makes fitting a smooth curve difficult. The larger fitting error accounts for this.

$\eta$ bin	SS or OS	errors - res. fit	errors - ansatz fit	errors - res. closure
0.0 - 0.5	SS	0.1 - 0.05%	0.2 - 0.7%	1.4 - 1.7%
0.0 - 0.5	OS	0.1103%	0.6 - 0.2%	1.3 - 0.7%
0.5 - 1.0	SS	0.17 - 0.15%	0.3 - 0.7%	1.1 - 1.4%
0.5 - 1.0	OS	0.05 - 0.08%	0.2 - 0.6%	1.5 - 1.1%
1.0 - 1.5	SS	0.4-0.5%	1.6 - 3.4%	1.8 - 4.0%
1.0 - 1.5	OS	0.4 - 0.3%	6.0 - 5.0%	2.0 - 3.0%
1.5 - 2.0	SS	0.9 - 0.6%	0.9 - 3.0%	1.6 - 3.0%
1.5 - 2.0	OS	0.8 - 0.9%	0.7 - 1.6%	0.9 - 1.4%

Table 5.2: Sources and magnitudes of unfolding error.

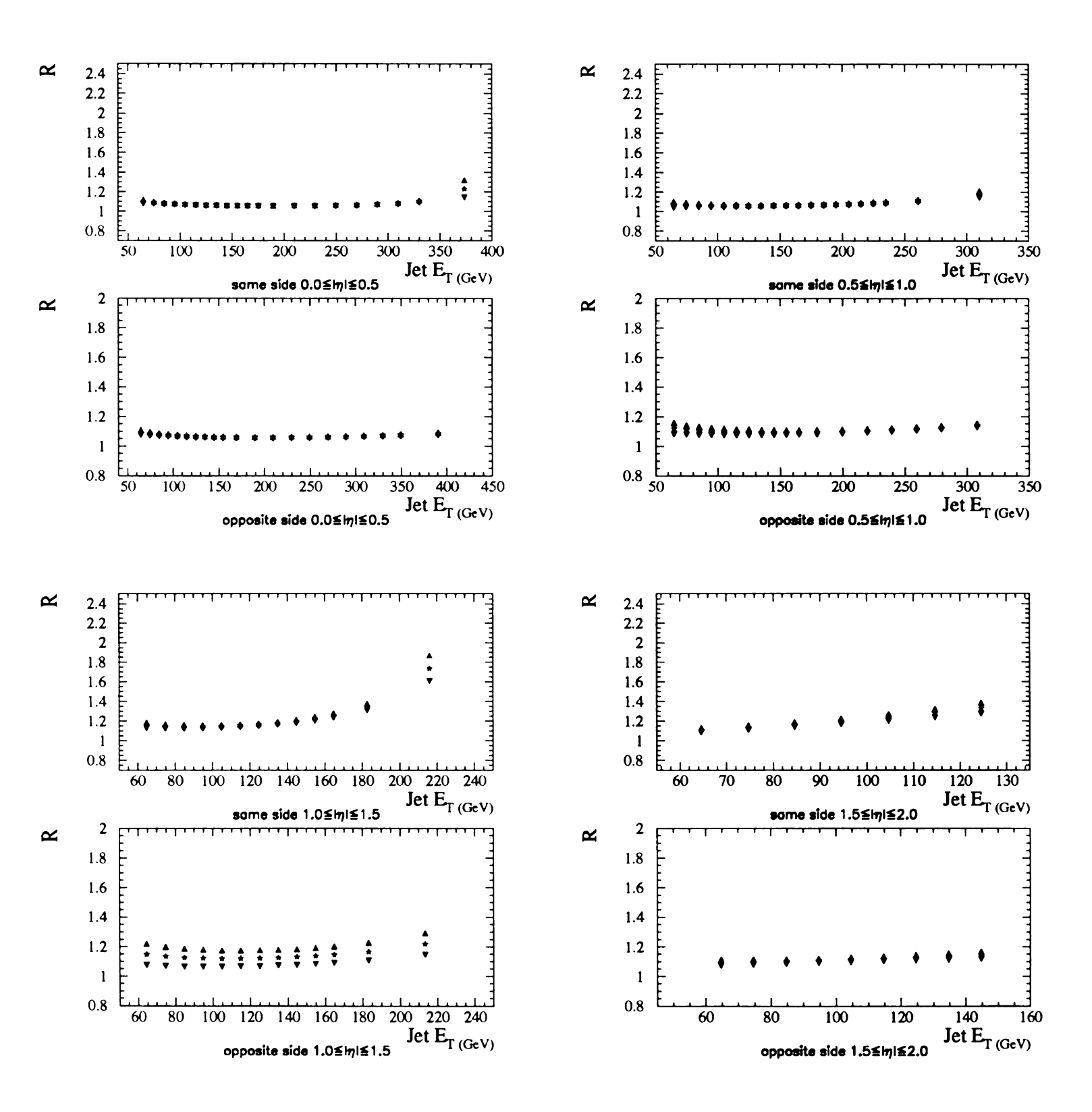


Figure 5.12: Unsmearing correction factors (R) and errors for all slices of the Triple Differential.

# 5.4 Derivation of Vertex Position Resolution Correction

#### 5.4.1 Outline of Assumptions

To derive a method to correct the measured cross sections for the effective vertex position resolution introduced above, a Monte Carlo study was performed. It is not obvious when attempting to correct the measured cross sections for the effects of vertex position resolution, at what stage to apply the correction. An argument can be made for unsmearing the cross sections as described above, but with resolutions which have been contaminated with the vertex position resolution, and in this way correcting for the energy resolution of the calorimeter, and the vertex position resolution simultaneously. It is not clear if this would work. However, it will be shown that this approach is flawed for another reason. The energy resolution of the calorimeter affects only the measured jet energy. Vertex position resolution affects the jet pseudo-rapidity as well. In fact, if the vertex position is mis-measured such that the jet  $E_T$  increases, the angle will always get smaller, and vice-versa. This is equivalent to the statement that as a jet moves further forward, its  $E_T$  decreases. In this way, these variables are highly, in fact completely anti-correlated, therefore a correction for  $\eta$  and  $E_T$  smearing must be derived simultaneously.

In order to investigate this effect, a cross section was generated from NLO jetrad with no smearing effects. Additional cross sections were generated in which only the jet  $E_T$  was recalculated with respect to a vertex distribution of width  $\sigma_Z = 10cm$ , and again with only the jet  $\eta$  recalculated. Finally, cross sections were recast with

both  $\eta$  and  $E_T$  recalculated together. The results of this study are presented in Figures 5.13 and 5.14. In Figure 5.13 we present the ratio of the Jetrad cross sections in which  $E_T$  and  $\eta$  were recalculated separately. This study was performed only for the same side and opposite side forward  $(1.5 \leq |\eta| \leq 2.0)$  bins. Observe that the effect of  $E_T$  smearing seems to dominate. If we were to try to de-couple these effects and add them together, ignoring any correlations that may exist, we would grossly over-estimate the effect. This is apparent in Figure 5.14 which contains the net effect of vertex position resolution smearing assuming no and complete correlations. Clearly, the effect is small when the correlations are properly accounted for. We now proceed with the description of the Monte Carlo based derivation of the vertex position resolution correction

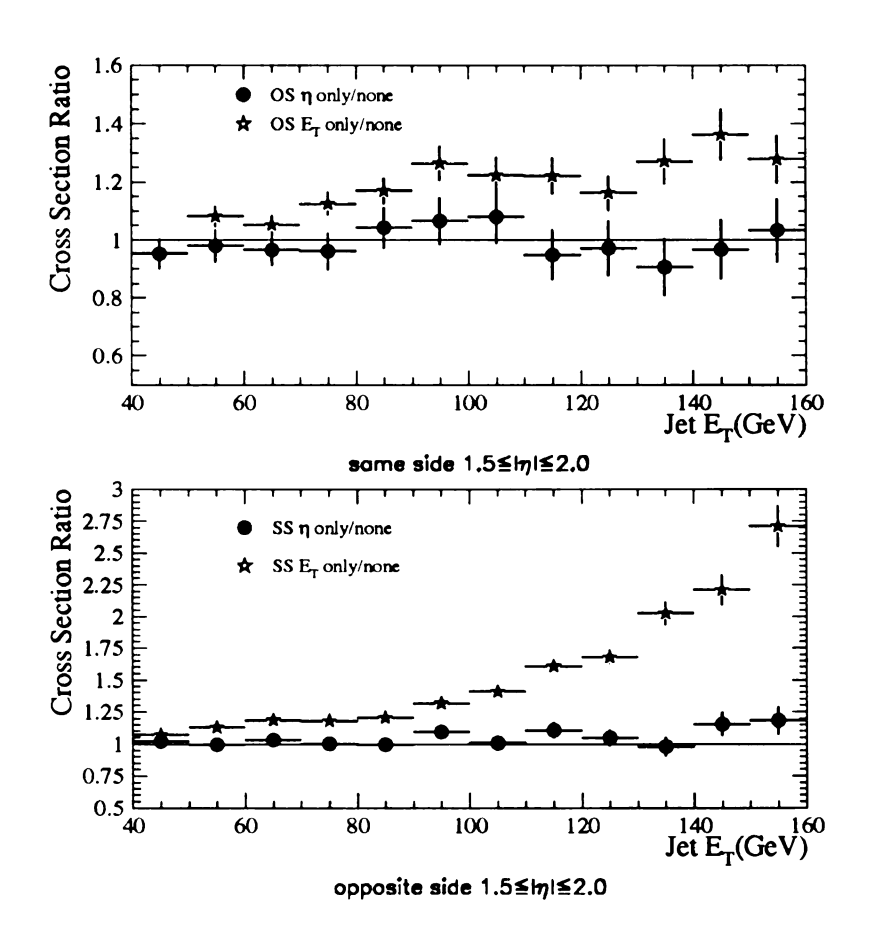


Figure 5.13: Monte Carlo derived effect of vertex smearing if only jet  $E_T$  or jet  $\eta$  are recalculated.

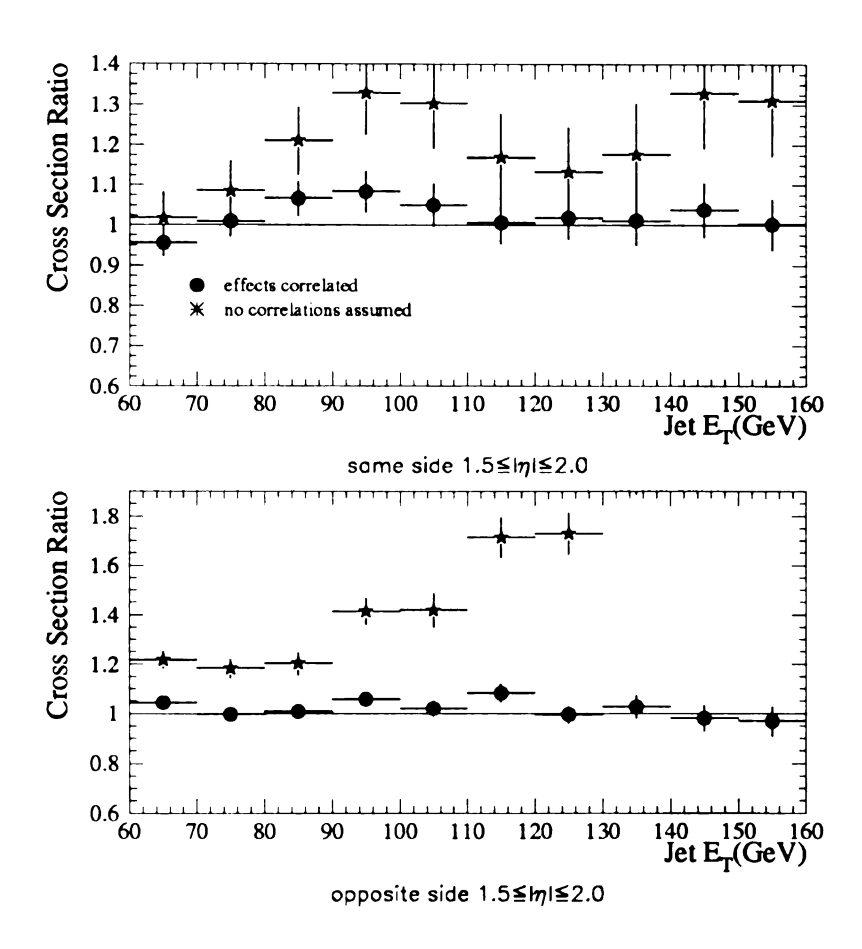


Figure 5.14: Monte Carlo derived effect of vertex smearing if jet  $E_T$  and jet  $\eta$  are recalculated, with different assumptions regarding the correlations between these variables.

#### 5.4.2 Correction Derivation and Implementation

Events in next-to-leading order Jetrad were subjected to vertex smearing based on the vertex position resolutions presented in Figure 5.10. The energies and angles of the jets in the events were recalculated with respect to the generated vertex and the cross sections were calculated before and after the smearing. The ratio of the unsmeared to the smeared cross section is then defined as the correction factor. The smearing was done with the high, nominal, and low vertex position resolutions, defined by the three curves in Figure 5.10. The ratio is fit to a second degree polynomial and a full error analysis is performed on the fit in order to understand any error introduced by fitting the correction factors in this way. The parameters, their errors and correlations are combined with the derivative of the polynomial to determine the error introduced by the fit. The error associated with the correction is defined as the fit error added in quadrature with the difference between the high and low corrections. In the end, the effect of the vertex position resolution appears to be very small. The correction is of the order of 1% for all slices considered. The correction introduces some small shape dependence as well. It may seem odd that the effective vertex position resolution has such a small effect on the measurement of the cross sections described here. It is believed that while  $E_T$  smearing due to effective vertex position resolution results in events smearing into the cross section,  $\eta$  smearing results in events smearing out. These two effects are very correlated, for example if the  $E_T$  of a jet increases due to vertex position resolution, the jet's angle will decrease<sup>‡‡</sup>. It is believed that the relative effects of both smearings, together

<sup>&</sup>lt;sup>‡‡</sup>This can be verified by a simple two jet calculation in which the jet quantities are calculated with respect to a vertex, and to Z=0.

with their correlations, are responsible for the relatively small correction needed to account for effective vertex position resolution.

To assuage the fear that the correction could depend on the theory used to derive it, the correction is derived from three different theories. A sample of leading order jetrad with scale  $\mu=E_T/2$ , an NLO sample with the same scale and a NLO sample with  $\mu=E/2$ . The results of this study for the three theories together with the errors are presented in Figures 5.15 and 5.16. The correction factors applied are derived from the NLO sample with  $\mu=E/2$  as it best represents the data<sup>†</sup>. All Monte Carlo samples used to derive the vertex position resolution correction use the CTEQ3M parton distribution function.

<sup>&</sup>lt;sup>†</sup>See Chapter 6.

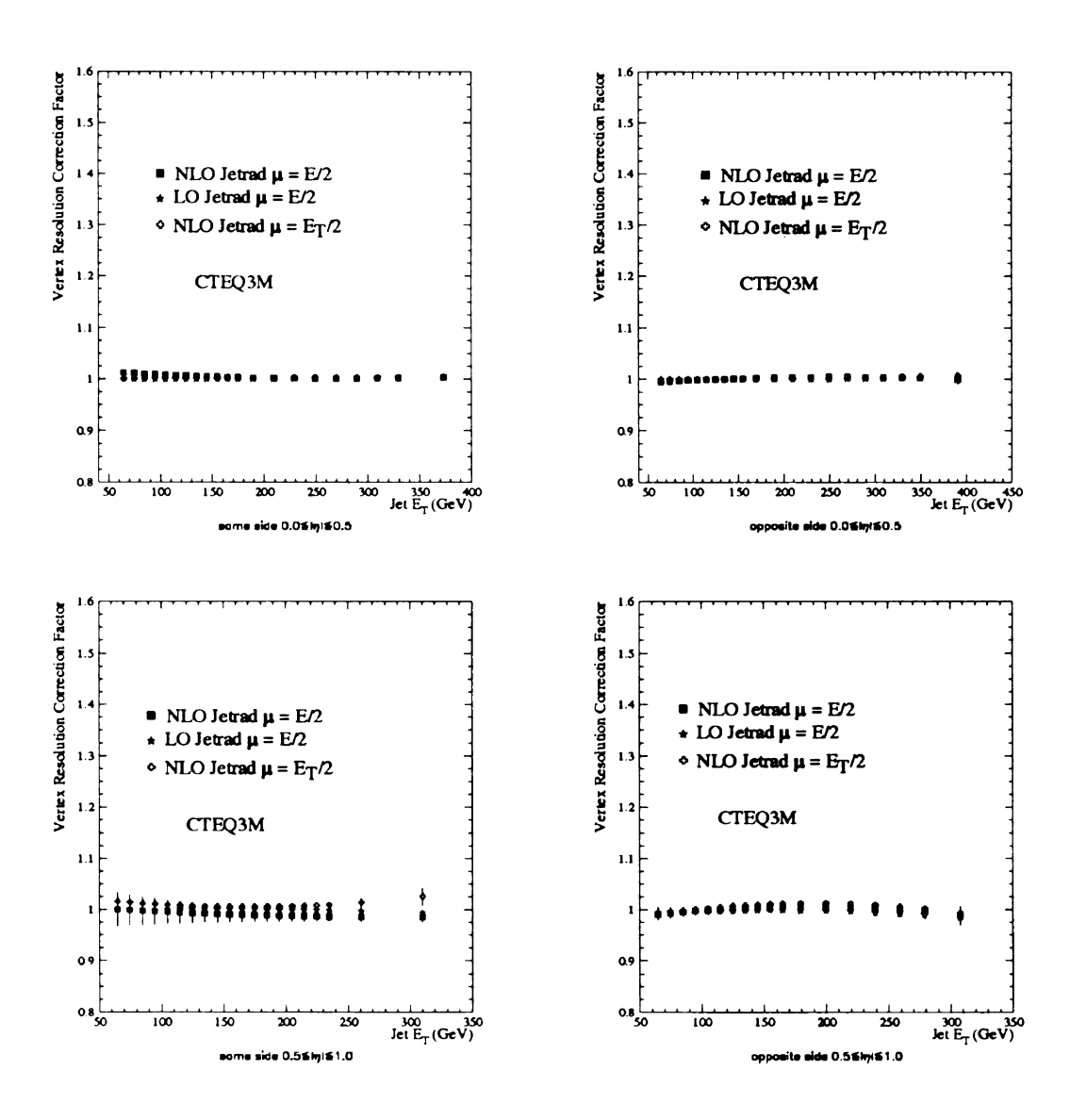


Figure 5.15: Effective vertex position resolution correction factors and errors derived from three Monte Carlo samples for slices 1 and 2.

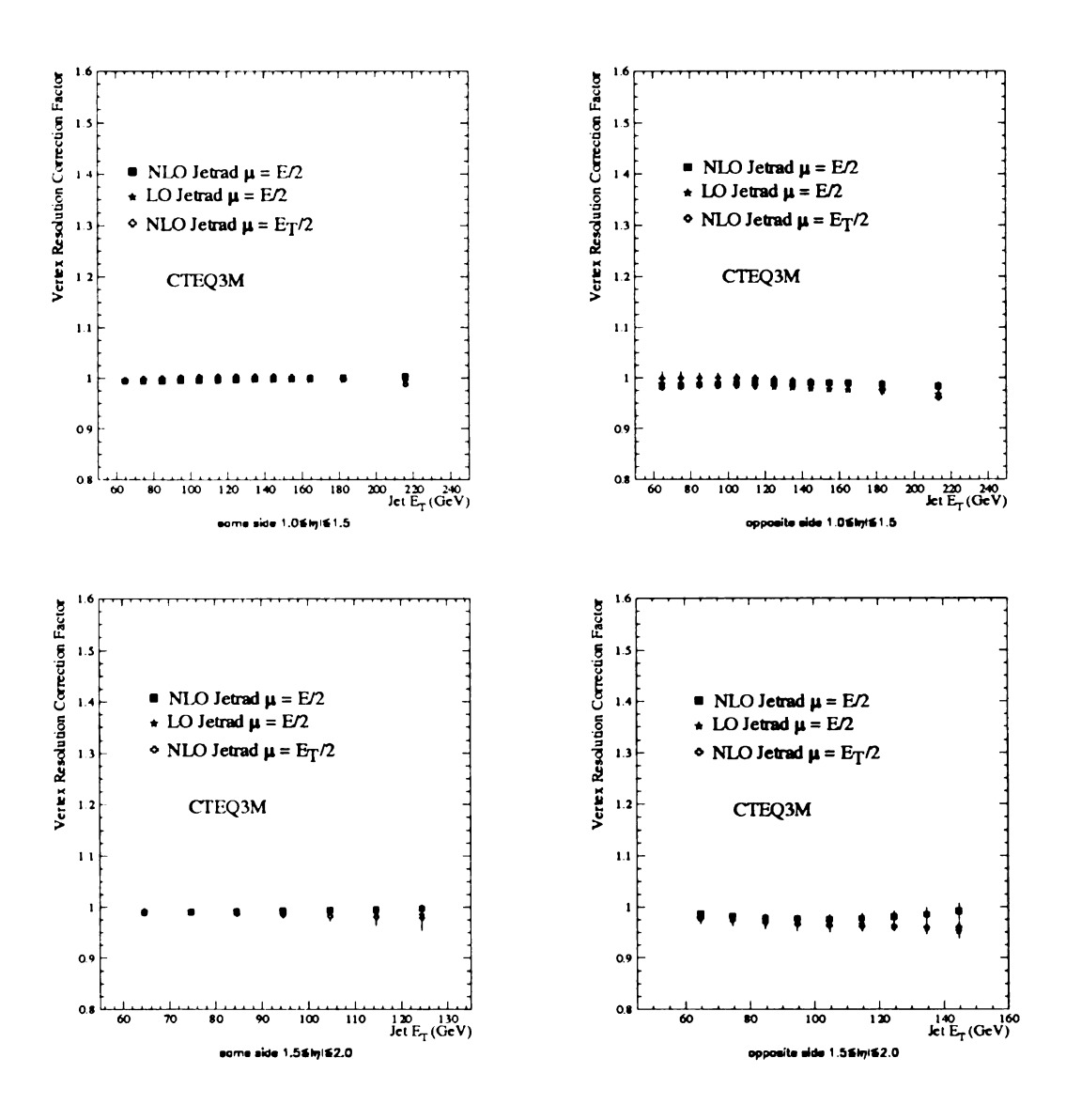


Figure 5.16: Effective vertex position resolution correction factors and errors derived from three Monte Carlo samples for slices 3 and 4.

# Chapter 6

# Results, Error Analyses, and

## **Conclusions**

In this chapter, the Triple Differential results and comparisons to theory are presented. The data and theory are presented on the same plot additionally, the fractional differences between the data and theory are presented.

A  $\chi^2$  test, which provides a quantified comparison to theory is also performed. In order to perform this test, the covariant error matrix for the Triple Differential must be understood. We describe the mechanism for producing this matrix and finally, quote a value for  $\chi^2$  for each of the theoretical predictions studied.

### 6.1 Graphical Comparisons to Theory

The error contributions for each of the eight slices are presented in Figures 6.1 and 6.2.

The fully corrected cross sections are presented in Figures 6.3 and 6.5. Addi-

tionally, the fractional differences with regard to one theory are presented in Figures 6.4 and 6.6. The results are compared to NLO Jetrad with the CTEQ3M parton distribution function with  $\mu=E/2$  in Figures 6.4 and 6.6. Figures 6.7 and 6.8 contain the data-theory comparisons using the CTEQ4M parton distribution function. Figures 6.9 and 6.10 compare the data to the CTEQ4HJ parton distribution function which predicts more jet production at high  $E_T$  than CTEQ4M. Figures 6.11 through 6.16 compare the data to a recent analysis of global data by the MRST group[23] called the MRST partons distribution functions. Figures 6.11 and 6.12 contain their nominal fit, Figures 6.13 and 6.14 contain a high fit to the MRST gluon distribution and Figures 6.15 and Figures 6.16 contain a low fit to the MRST gluon distribution. All the predictions shown use factorization and renormalization scales of  $\mu=E/2$ .

The components of the systematic error for each slice are presented in Figures 6.1 and 6.2 and numerically in Tables 6.1 and 6.2. The energy scale error is the largest component for all slices; the components of the energy scale error are itemized in Chapter 4.

The data appear to be in very good agreement with the CTEQ3M family with scale  $\mu=E/2$ . CTEQ4M appears to have a slightly different normalization, but the data still agree for all slices considered. CTEQ3M and CTEQ4M differ in that CTEQ4M contains collider jet data while CTEQ3M does not. CTEQ4HJ brings down the slight excess in the OS central cross section, but produces some disagreement in the rest of the slices.

<sup>&</sup>lt;sup>†</sup>Here, high and low are ambiguous terms used to describe perturbations to the fit performed to the MRST gluon distribution.

MRST appears to be too high in the central region, but agrees well elsewhere. The high gluon fit from the MRS group MRSTg† appears to be consistent with DØ data, while the low gluon fit, MRSTg↓, shows considerable disagreement almost everywhere.

Slice 1		Slice 2	
E scale	8 - 20	E scale	8 - 20
cut efficiency	< 1.0	cut efficiency	< 1.0
luminosity	6.8 - 5.4	luminosity	6.8 - 5.4
unfolding	.2 - 4	unfolding	.6 - 7
vertex corr.	< 1.0	vertex corr.	< 1.0
eta bias corr.	~ 1	eta bias corr.	~ 1

Table 6.1: Fractional (%) error components for slices 1 and 2 of the Triple Differential.

Slice 3		Slice 4	
E scale	10 - 40	E scale	19 - 35
cut efficiency	< 1.0	cut efficiency	< 1.0
luminosity	6.8 - 5.4	luminosity	6.8 - 5.4
unfolding	2 - 5	unfolding	2 - 12
vertex corr.	< 1.0	vertex corr.	< 1.0
eta bias corr.	1 - 3	eta bias corr.	1 - 5

Table 6.2: Fractional (%) error components for slices 3 and 4 of the Triple Differential.

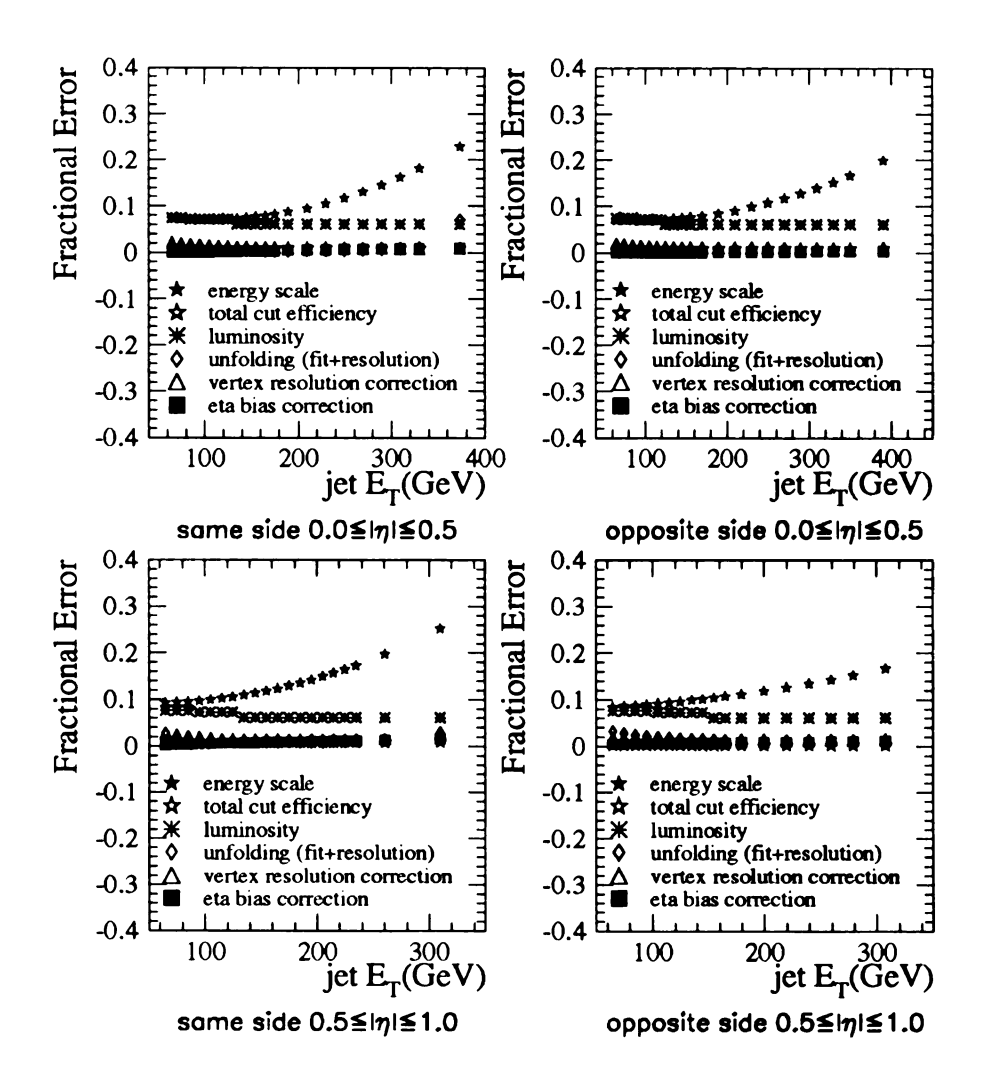


Figure 6.1: Components of the error for slices 1 and 2.

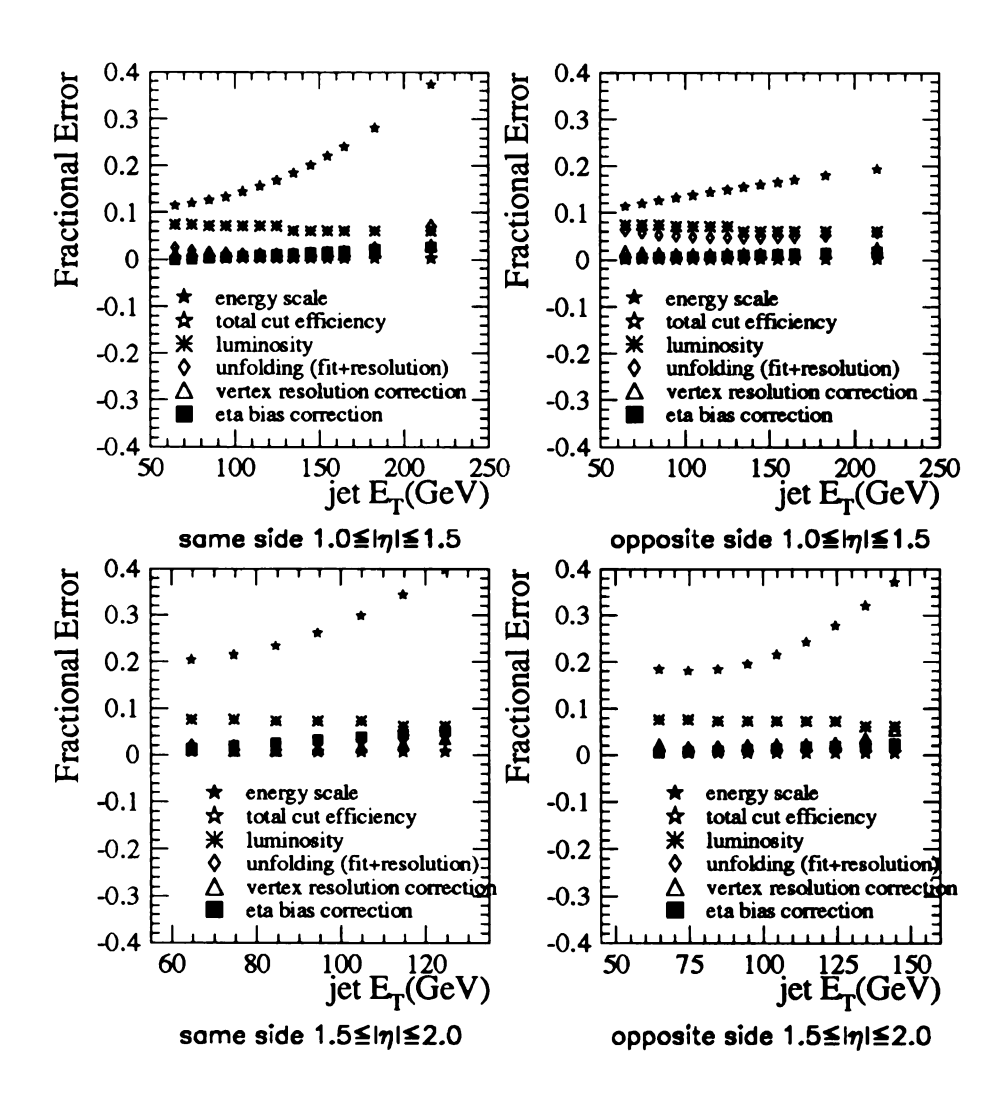


Figure 6.2: Components of the error for slices 3 and 4.

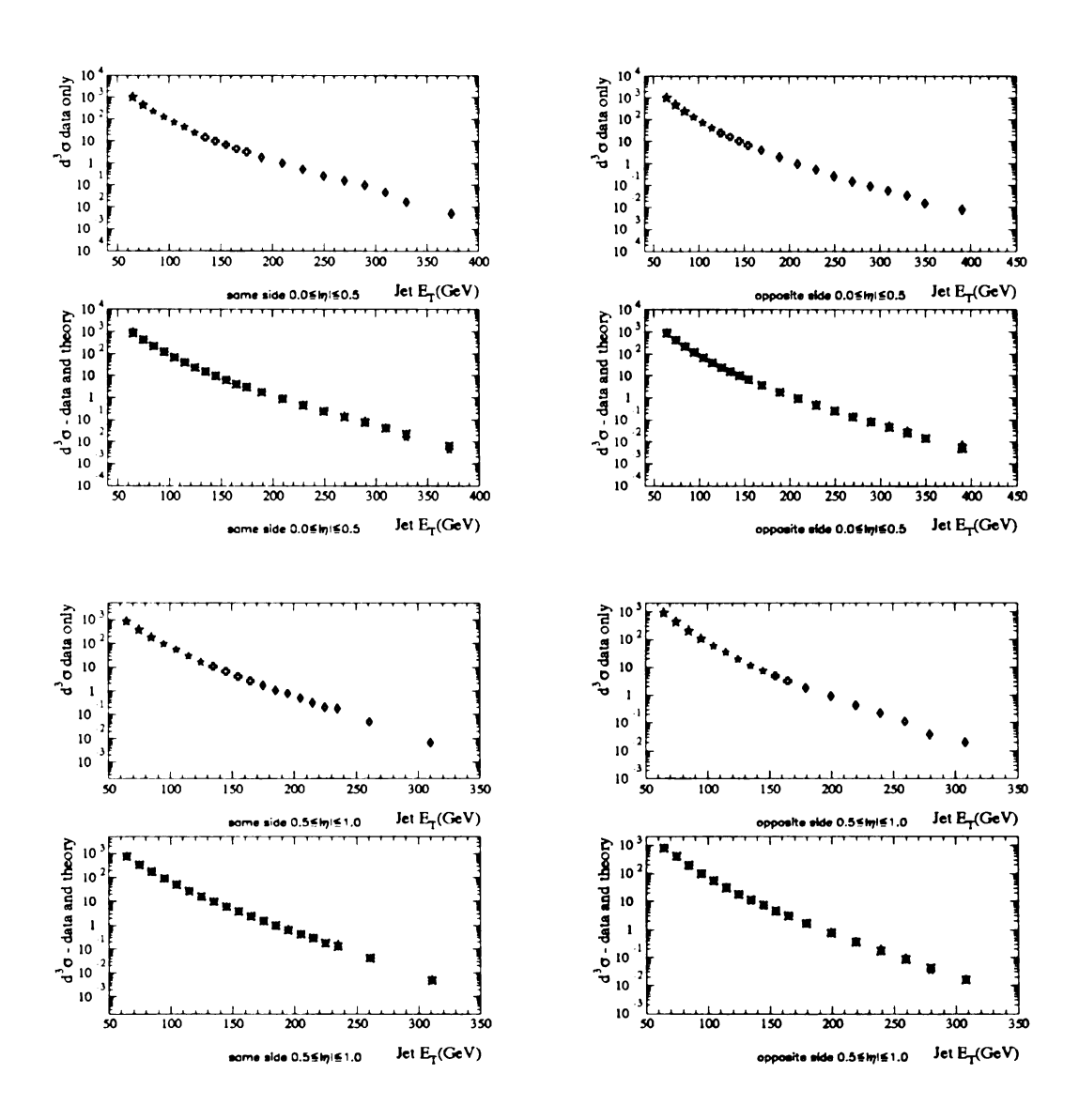


Figure 6.3: The fully corrected triple differential compared to NLO Jetrad, CTEQ3M,  $\mu = \frac{1}{2}E$  for slices 1 and 2. The cross sections have units of picobarns.

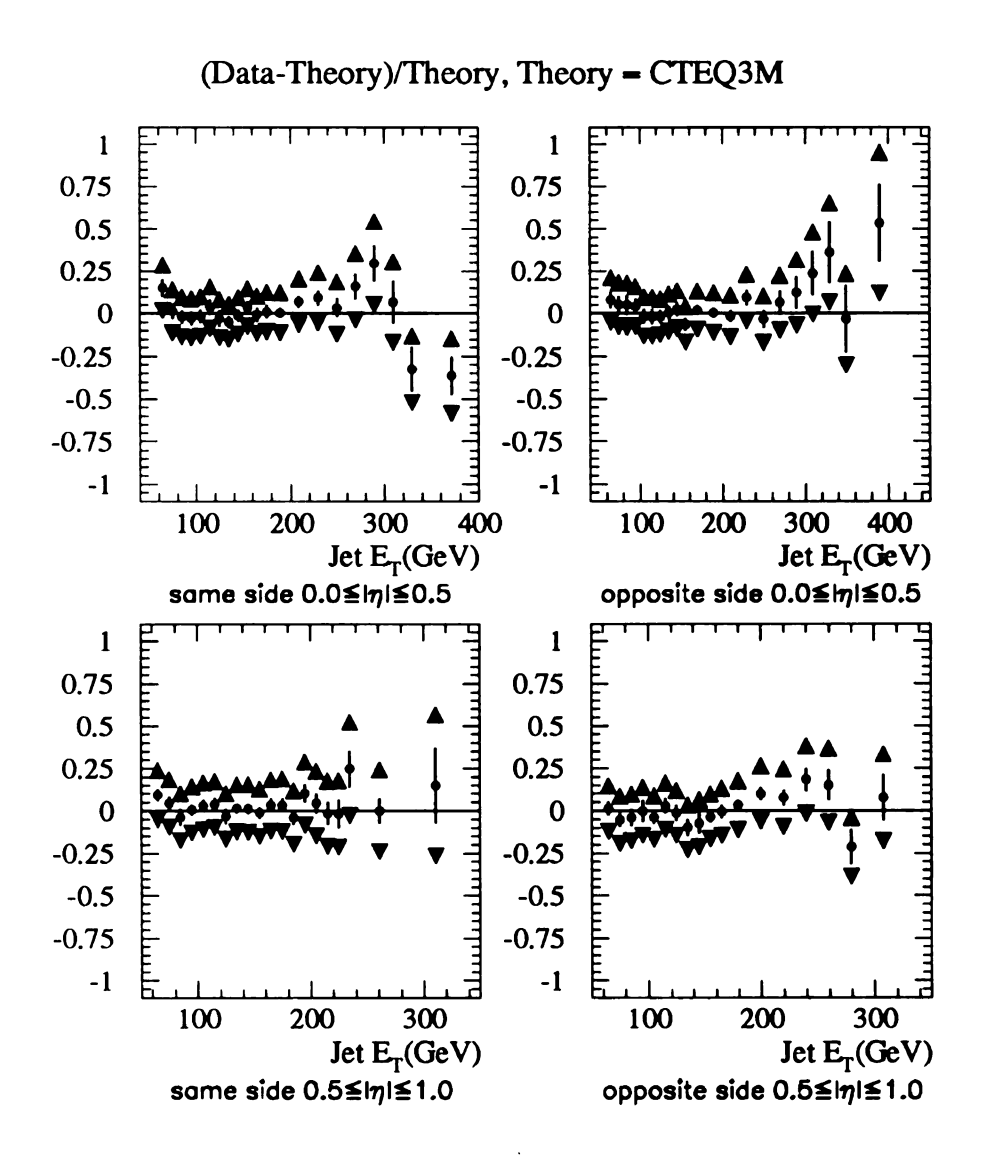


Figure 6.4: The fully corrected triple differential compared to NLO Jetrad, CTEQ3M,  $\mu = \frac{1}{2}E$  for slices 1 and 2, (data - theory)/theory. The inner error bars are statistical only, the outer are the sum of all errors, statistical + systematic.

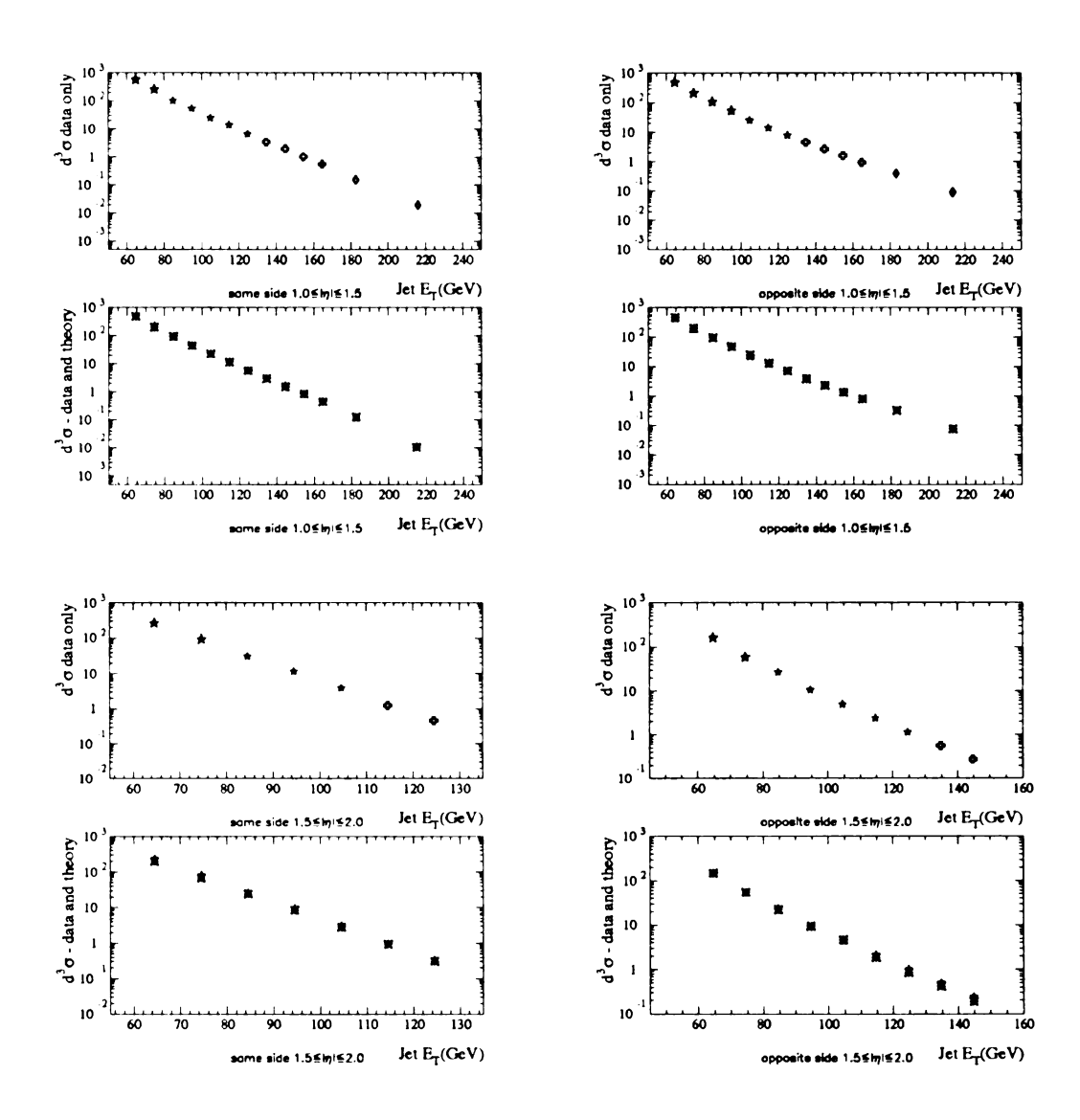


Figure 6.5: The fully corrected triple differential compared to NLO Jetrad, CTEQ3M,  $\mu=\frac{1}{2}E$  for slices 3 and 4. The cross sections have units of picobarns.

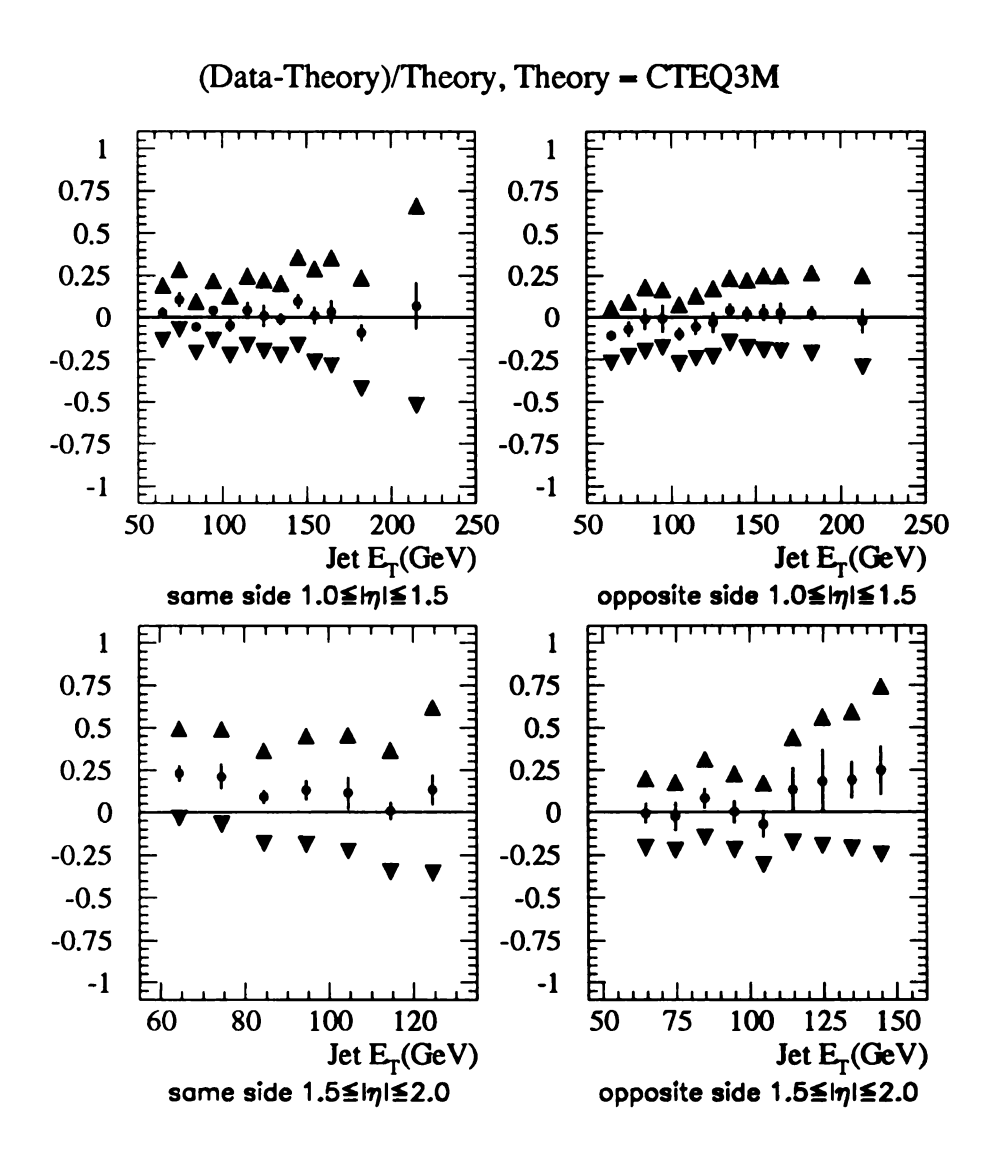


Figure 6.6: The fully corrected triple differential compared to NLO Jetrad, CTEQ3M,  $\mu = \frac{1}{2}E$  for slices 3 and 4, (data - theory)/theory. The inner error bars are statistical only, the outer are the sum of all errors, statistical + systematic.

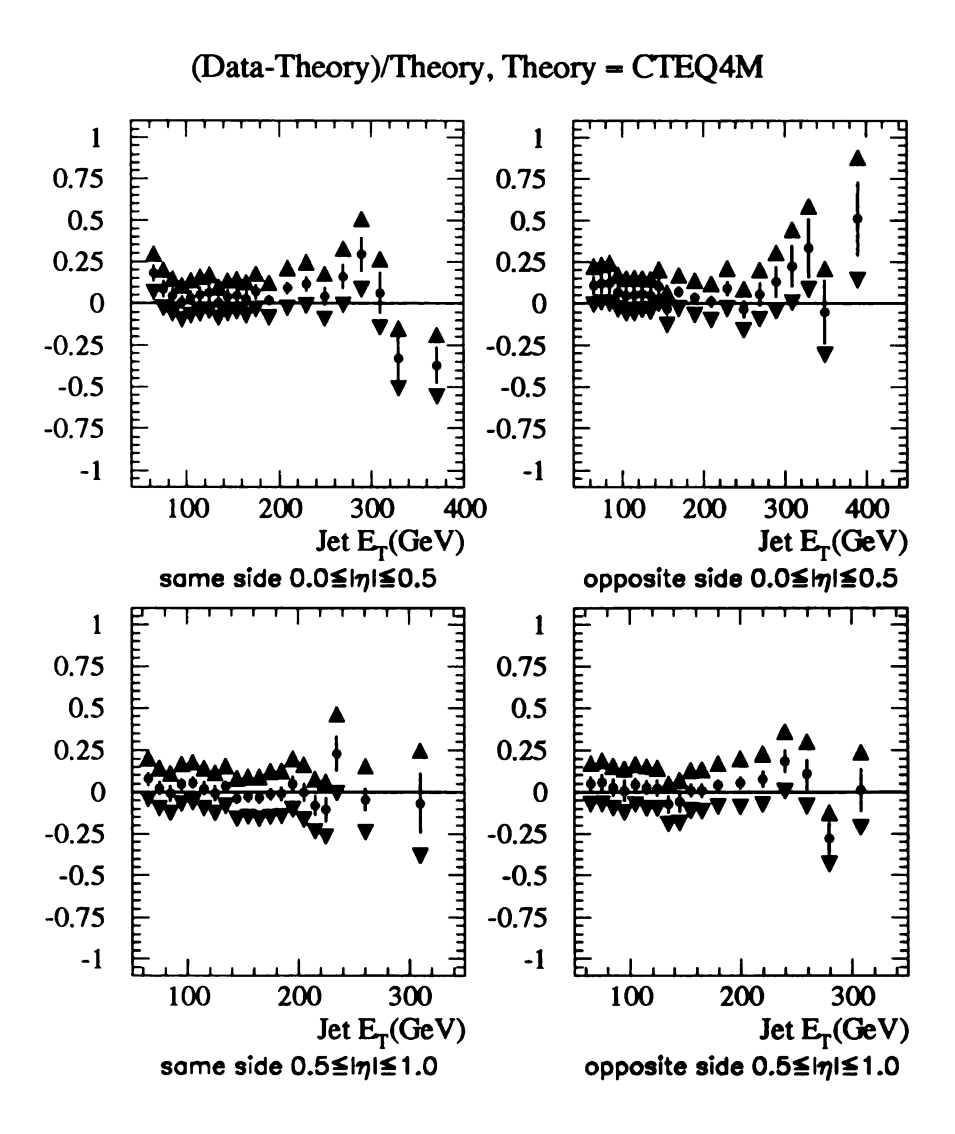


Figure 6.7: The fully corrected triple differential compared to NLO Jetrad, CTEQ4M,  $\mu = \frac{1}{2}E$  for slices 1 and 2, (data - theory)/theory. The inner error bars are statistical only, the outer are the sum of all errors, statistical + systematic.

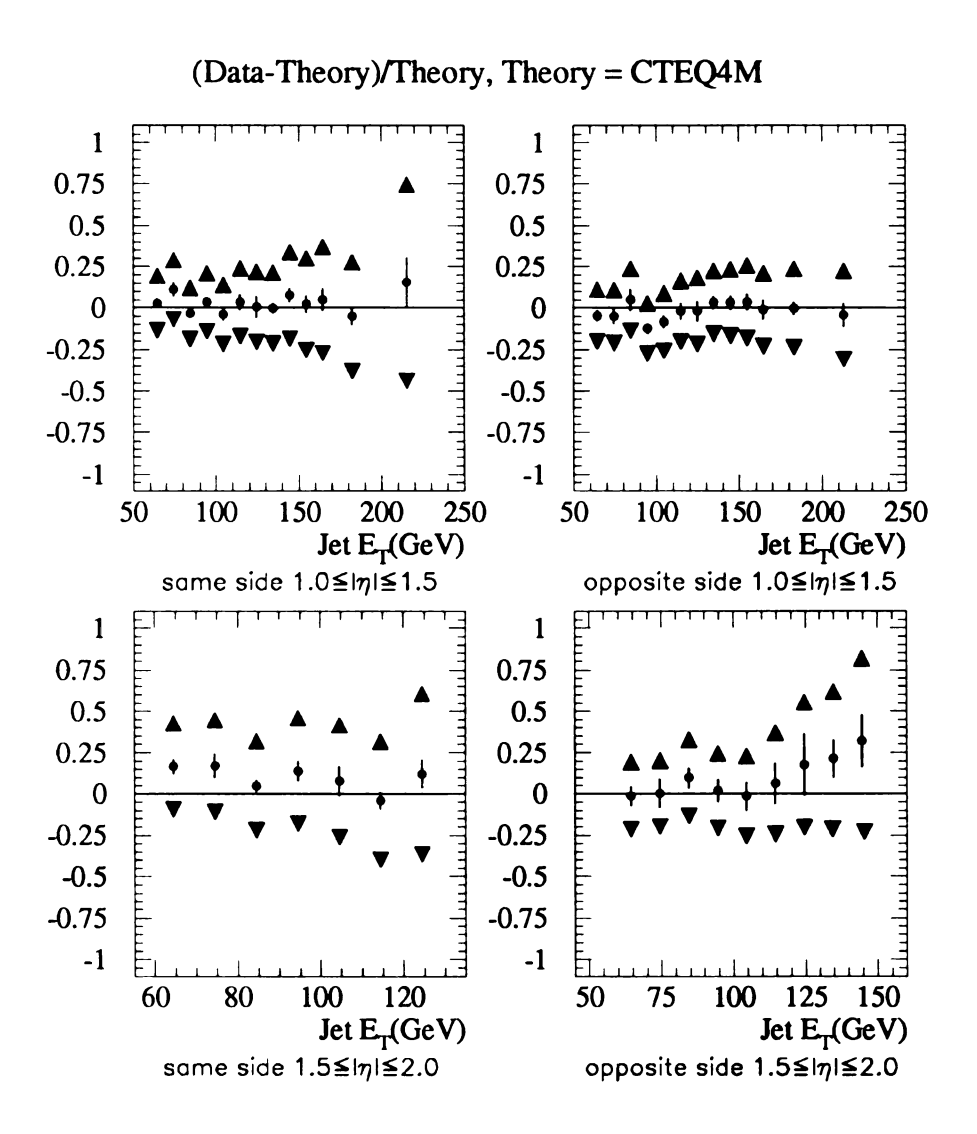


Figure 6.8: The fully corrected triple differential compared to NLO Jetrad, CTEQ4M,  $\mu = \frac{1}{2}E$  for slices 3 and 4, (data - theory)/theory. The inner error bars are statistical only, the outer are the sum of all errors, statistical + systematic.

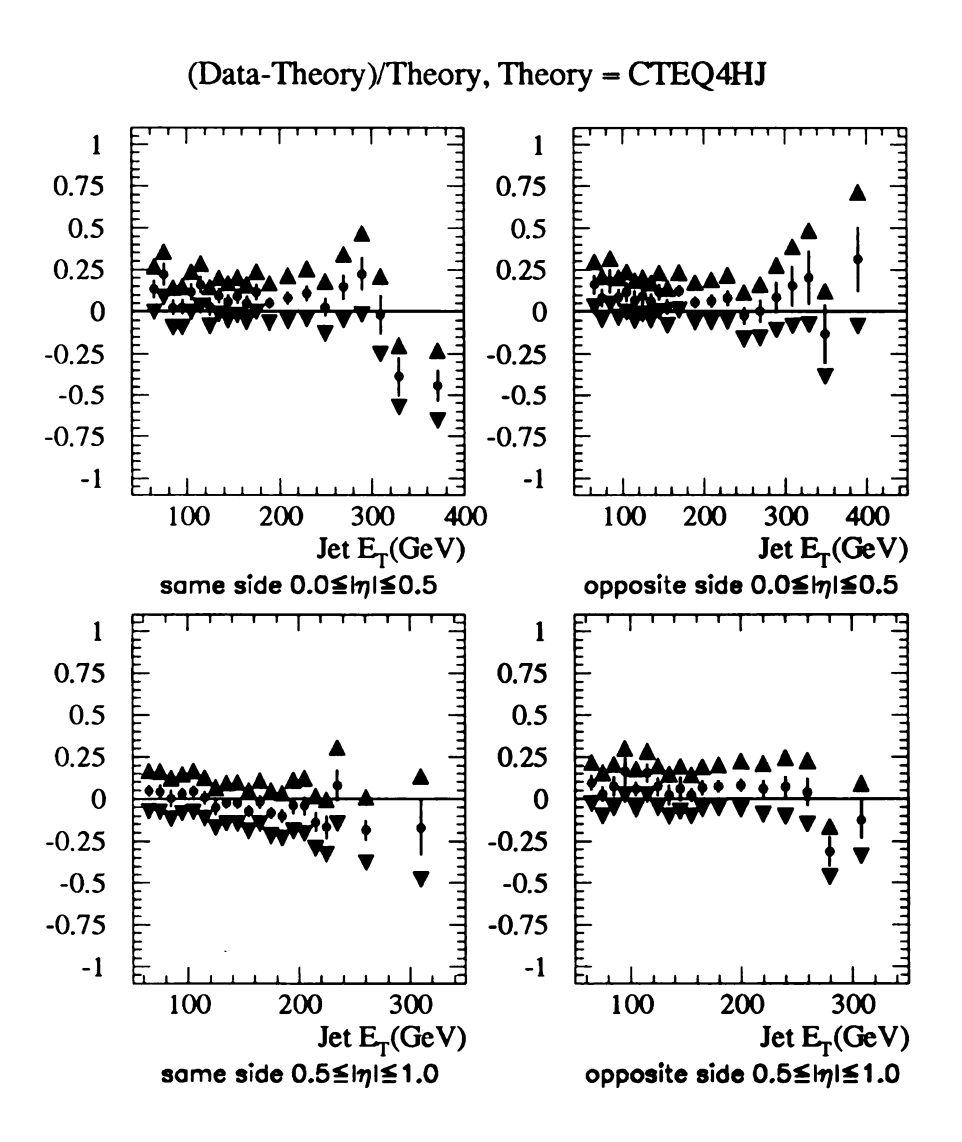


Figure 6.9: The fully corrected triple differential compared to NLO Jetrad, CTEQ4HJ,  $\mu = \frac{1}{2}E$  for slices 1 and 2, (data - theory)/theory. The inner error bars are statistical only, the outer are the sum of all errors, statistical + systematic.

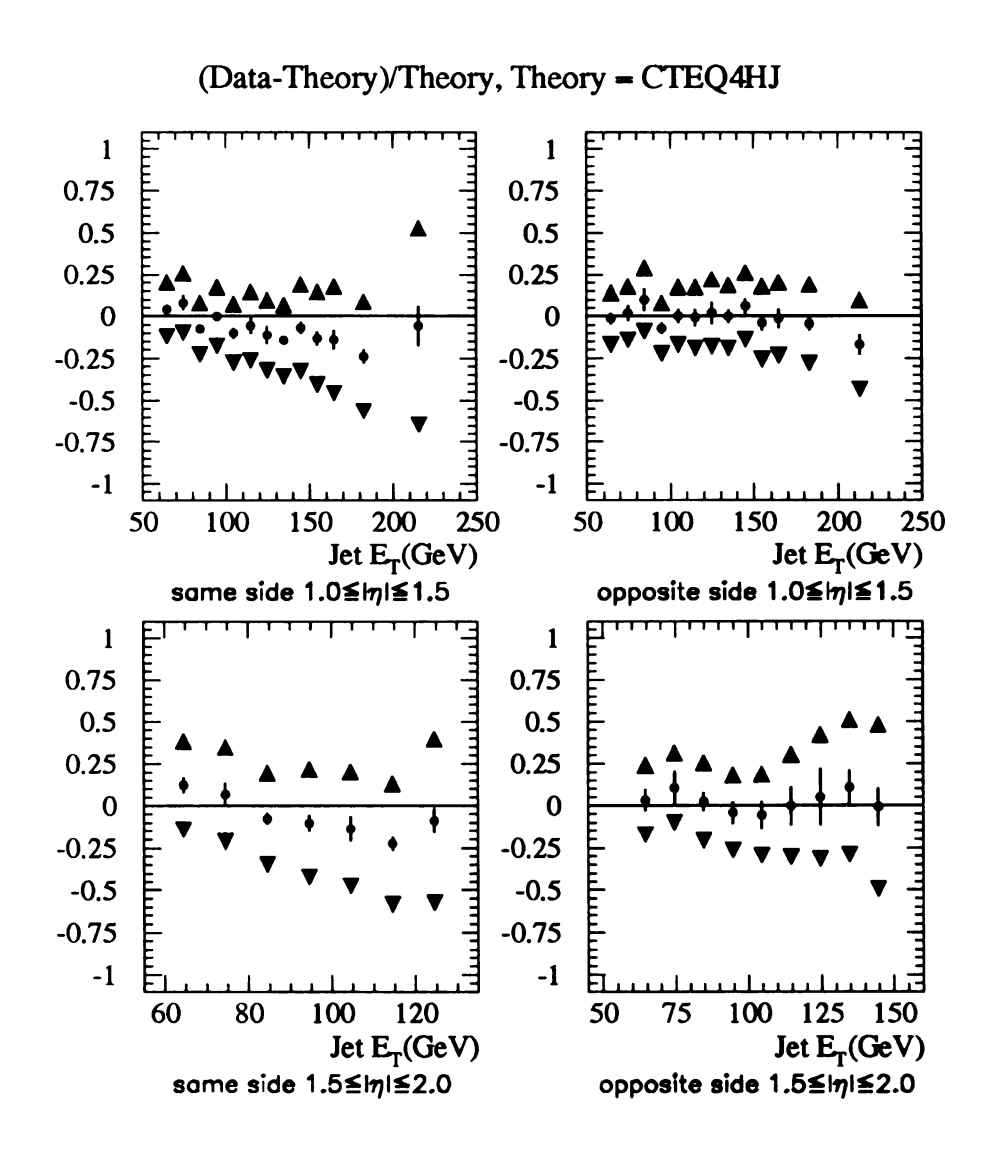


Figure 6.10: The fully corrected triple differential compared to NLO Jetrad, CTEQ4HJ,  $\mu = \frac{1}{2}E$  for slices 3 and 4, (data - theory)/theory. The inner error bars are statistical only, the outer are the sum of all errors, statistical + systematic.

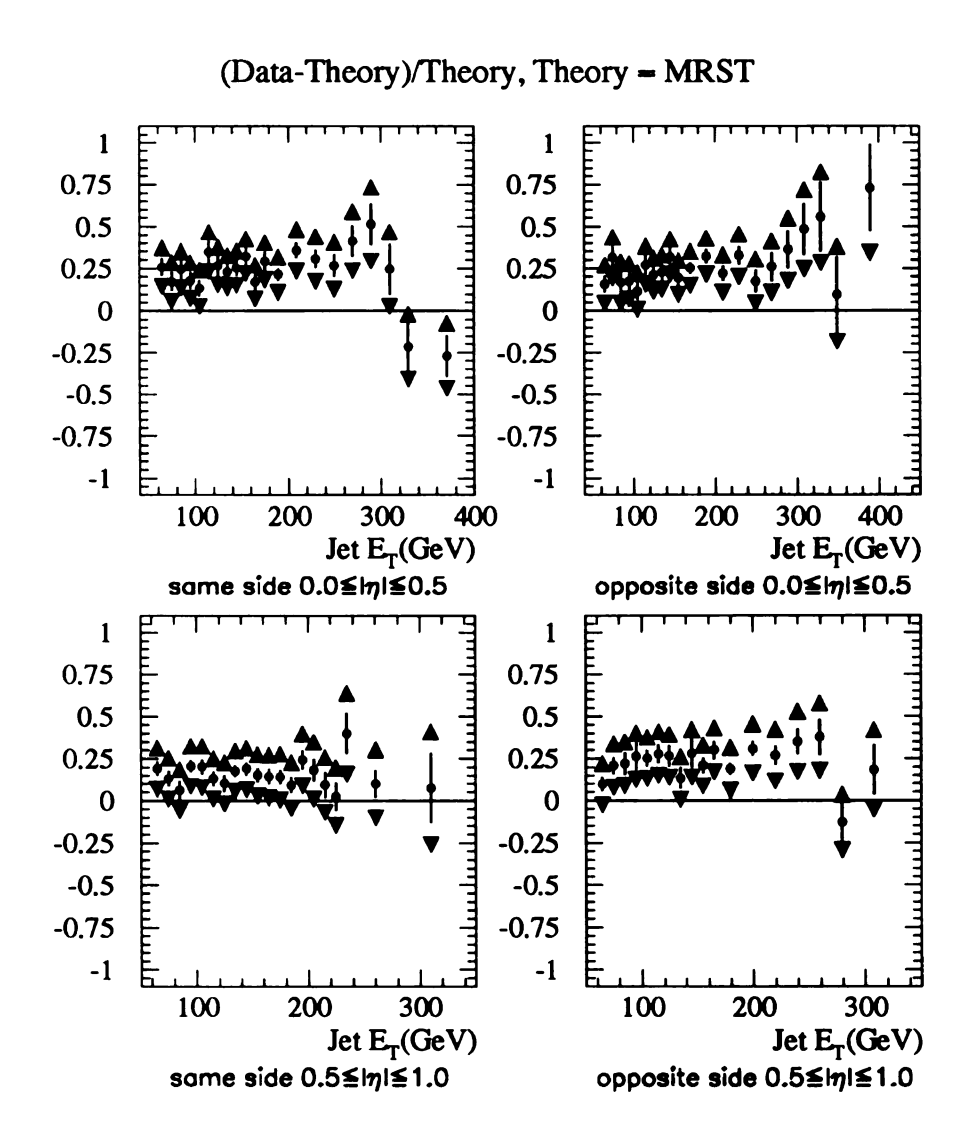


Figure 6.11: The fully corrected triple differential compared to NLO Jetrad, MRST,  $\mu = \frac{1}{2}E$  for slices 1 and 2, (data - theory)/theory. The inner error bars are statistical only, the outer are the sum of all errors, statistical + systematic.

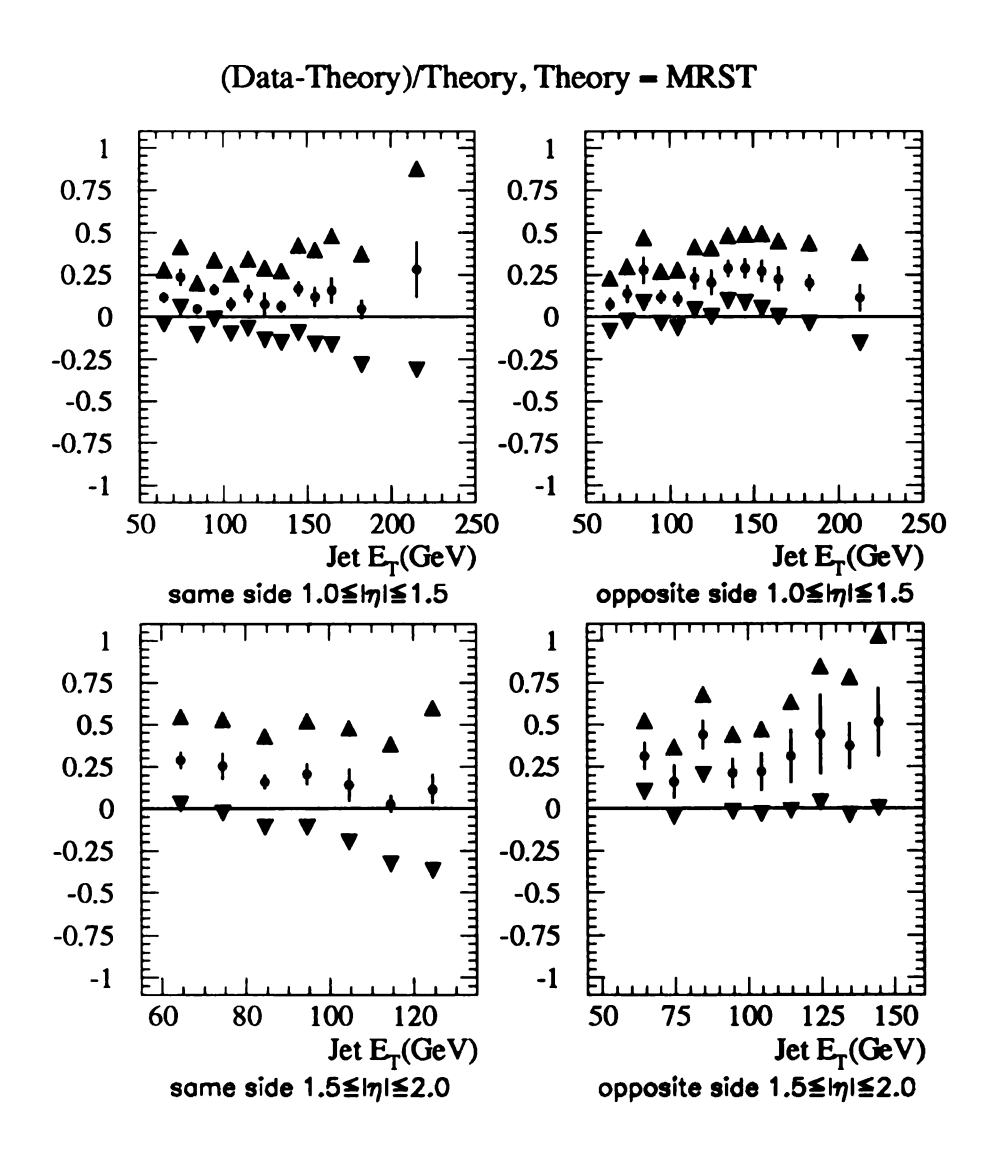


Figure 6.12: The fully corrected triple differential compared to NLO Jetrad, MRST,  $\mu = \frac{1}{2}E$  for slices 3 and 4, (data - theory)/theory. The inner error bars are statistical only, the outer are the sum of all errors, statistical + systematic.

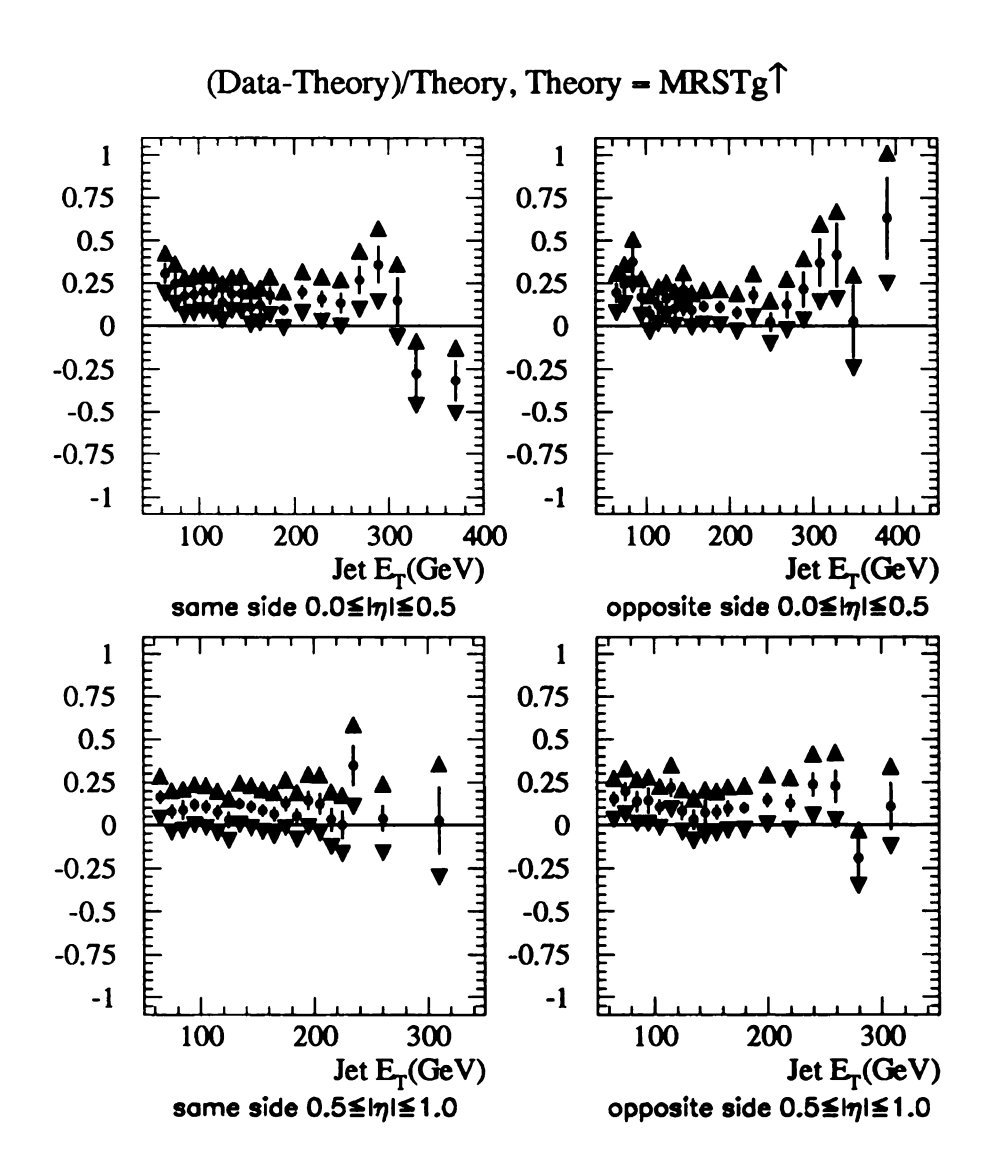


Figure 6.13: The fully corrected triple differential compared to NLO Jetrad, MRSTg $\uparrow$ ,  $\mu = \frac{1}{2}E$  for slices 1 and 2, (data - theory)/theory. The inner error bars are statistical only, the outer are the sum of all errors, statistical + systematic.

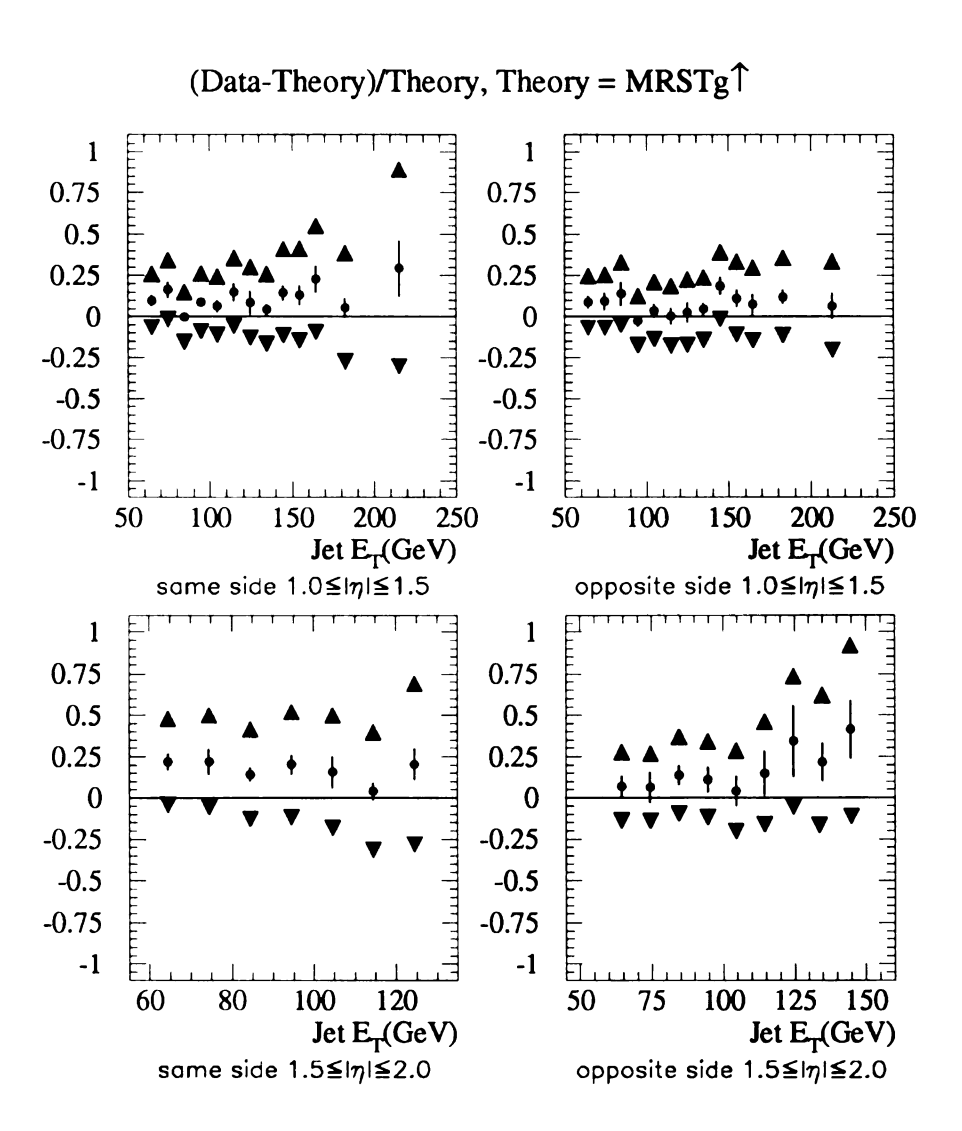


Figure 6.14: The fully corrected triple differential compared to NLO Jetrad, MRSTg $\uparrow$ ,  $\mu = \frac{1}{2}E$  for slices 3 and 4, (data - theory)/theory. The inner error bars are statistical only, the outer are the sum of all errors, statistical + systematic.

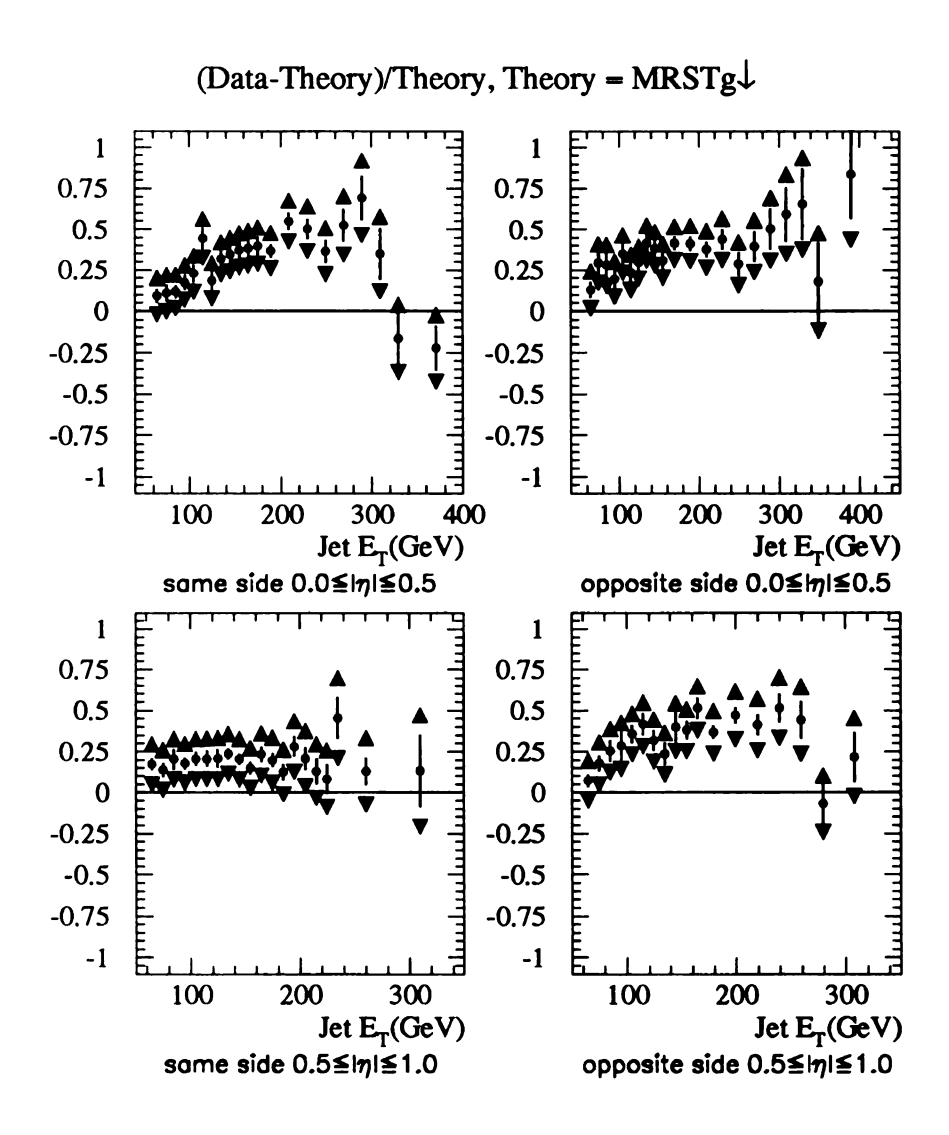


Figure 6.15: The fully corrected triple differential compared to NLO Jetrad, MRSTg $\downarrow$ ,  $\mu=\frac{1}{2}E$  for slices 1 and 2, (data - theory)/theory. The inner error bars are statistical only, the outer are the sum of all errors, statistical + systematic.

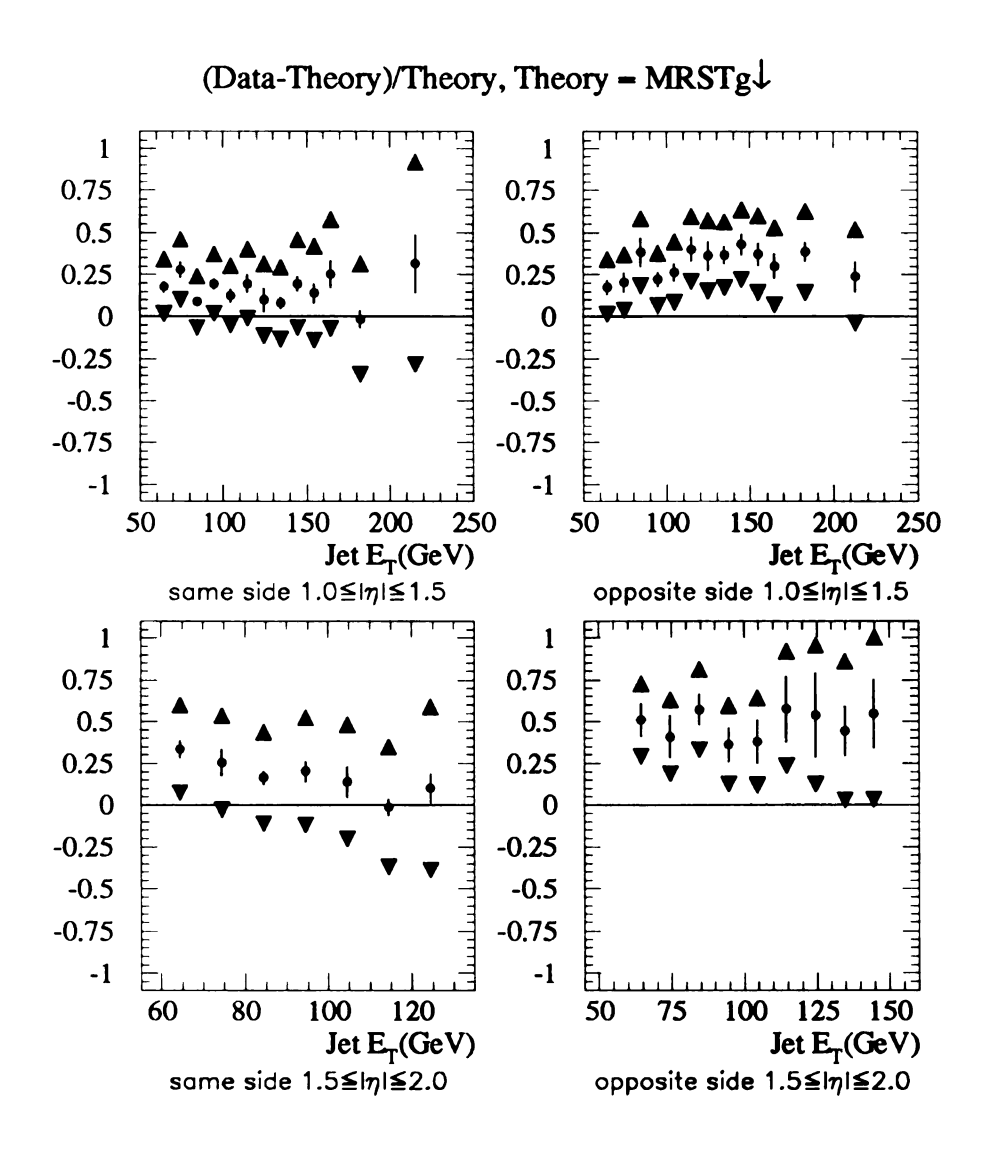


Figure 6.16: The fully corrected triple differential compared to NLO Jetrad, MRSTg $\downarrow$ ,  $\mu = \frac{1}{2}E$  for slices 3 and 4, (data - theory)/theory. The inner error bars are statistical only, the outer are the sum of all errors, statistical + systematic.

#### 6.2 Quantitative Theory Comparisons

In order to quantify a comparison to a theoretical prediction, a more sophisticated error analysis can be performed. The goal is to understand the *correlations* between each data point's error bar and the error associated with the other data points. This is equivalent to the construction of the *correlation matrix*. If the elements of the correlation matrix are multiplied by the errors of the corresponding data points, the *covariance matrix* results. We will discuss the elements necessary to construct this matrix for the Triple Differential.

The sources of error in the Measurement of the Triple Differential are presented in Table 6.3, which describes each error contribution and its correlations to the other data points in the cross section. Each error can be classified as either uncorrelated, totally correlated, or partially correlated. In addition, totally and partially correlated errors can be correlated across each slice (in  $E_T$ ), and not correlated with other slices, or correlated across the entire Triple Differential.

error	$E_T$ correlation	cross section correlation
data statistical	uncorrelated	uncorrelated
cut efficiency	uncorrelated	uncorrelated
luminosity	correlated	correlated
unsmearing	correlated	uncorrelated
vertex res. corr.	correlated	uncorrelated
eta bias corr.	correlated	uncorrelated
energy scale	partially	partially

Table 6.3: Sources of error in the Triple Differential and their correlations

We first treat the errors not associated with the energy scale correction as they are either totally correlated or completely uncorrelated. We then discuss the energy

# 6.2.1 Construction of the Covariance Matrix for Errors not Associated with the Energy Scale Correction

We begin by defining the error associated with data point i as  $\delta_i$ ; the index i runs across each  $E_T$  bin in each cross section. The cross sections are ordered (arbitrarily) such that i = 1, 21 defines the same side central slice, i = 22, 42 covers the opposite side central slice, i = 43, 63 spans the same side cross section in the bin  $0.5 \le |\eta| \le 1.0$  and so forth; i runs from 1 to 123 as there are 123 total bins in our measurement of the Triple Differential.

We construct a matrix defined by  $M_{i,j} = \delta_i \delta_j$  for each of the errors described in Table 6.3. Next  $M_{i,j}$  is multiplied by one of three matrices depending on the degree of correlation,  $\sigma_{i,j} = M_{i,j} \times \rho_{i,j}$ .  $\sigma_{i,j}$  is the covariance matrix for errors not associated with the energy scale.  $\rho_{i,j}$  is either a unit matrix for totally correlated errors across the entire Triple Differential, a matrix defined by  $\rho_{i,j} = \delta_{i,j}^{kr}$  where  $\delta^{kr}$  is the Kronecker delta symbol<sup>‡</sup>, in the case of totally uncorrelated errors, or a block diagonal matrix in the case of errors which are correlated between each  $E_T$  bin in a cross section, but uncorrelated between cross sections.

This formalism can be visualized by studying the correlation matrix,  $\rho_{i,j}$  for these errors, presented in Figure 6.17. The figure contains the correlation matrix for all errors except errors associated with the energy scale. Although the inputs to each component's correlation are either 1.0 or 0.0, the net effect introduces partial

 $<sup>{}^{\</sup>dagger}\delta_{i,j}^{kr}=1$ , if i=j, 0 otherwise.

correlations, this explains the fractional correlations visible in the figure.

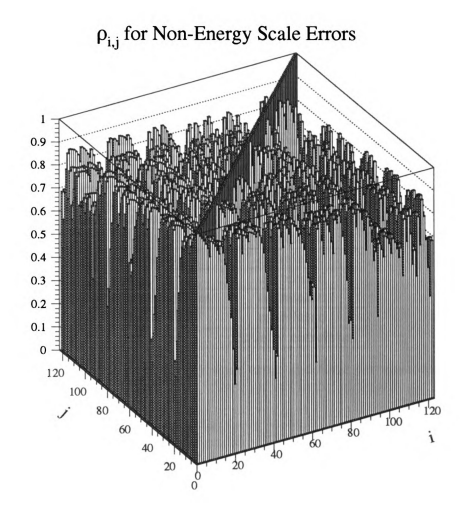


Figure 6.17: The correlation matrix for errors not associated with the energy scale correction.

# 6.2.2 Construction of the Covariance Matrix for Errors Associated with the Energy Scale Correction

The energy scale correction has different sources of error with different degrees of correlation between  $E_T$  bins. These errors are summarized in Table 6.4. Correlated energy scale errors are considered to be correlated across all cross sections.

errors	correlation	
statistical	uncorrelated	
offset	correlated	
showering	correlated	
background	correlated	
systematic biases	correlated	
low $E_T$ bias	correlated	
response	partially correlated	

Table 6.4: Sources of energy scale error and their correlations.

The response correction is treated differently as its error is partially correlated between  $E_T$  bins. The response is a fit to many data points, this fit introduces the partial correlation in the response error. This fit was studied, by varying each data point and studying the change of the response correction for each of the other data points. The correlation matrix for the response error is presented in[11]. Since there isn't enough data in the cross sections to adequately populate the energy scale covariance matrix, a simple Monte Carlo was developed. In this toy Monte Carlo, an event is generated and weighted by the measured cross section. This event is then studied to determine the energy scale correction and error associated with each component. This is repeated for many events and appropriately averaged to populate the energy scale covariance matrix.

We can test this formalism by exploiting the fact that the energy scale error associated with each point is identical to the square root of the diagonal of the energy scale covariance matrix:

$$\sigma_{i,j}^{escale} = \delta i \delta j \rho_{i,j}$$

however, across the diagonal i = j which implies

$$\sigma_{i,i}^{escale} = \delta i \delta i \rho_{i,i}$$

and

$$\delta_i^{escale} = \sqrt{\sigma_{i,i}^{escale}}.$$

This can be compared to the error obtained from the energy scale package during execution to test the accuracy of the toy Monte Carlo. The results of this test are presented in Figure 6.18.

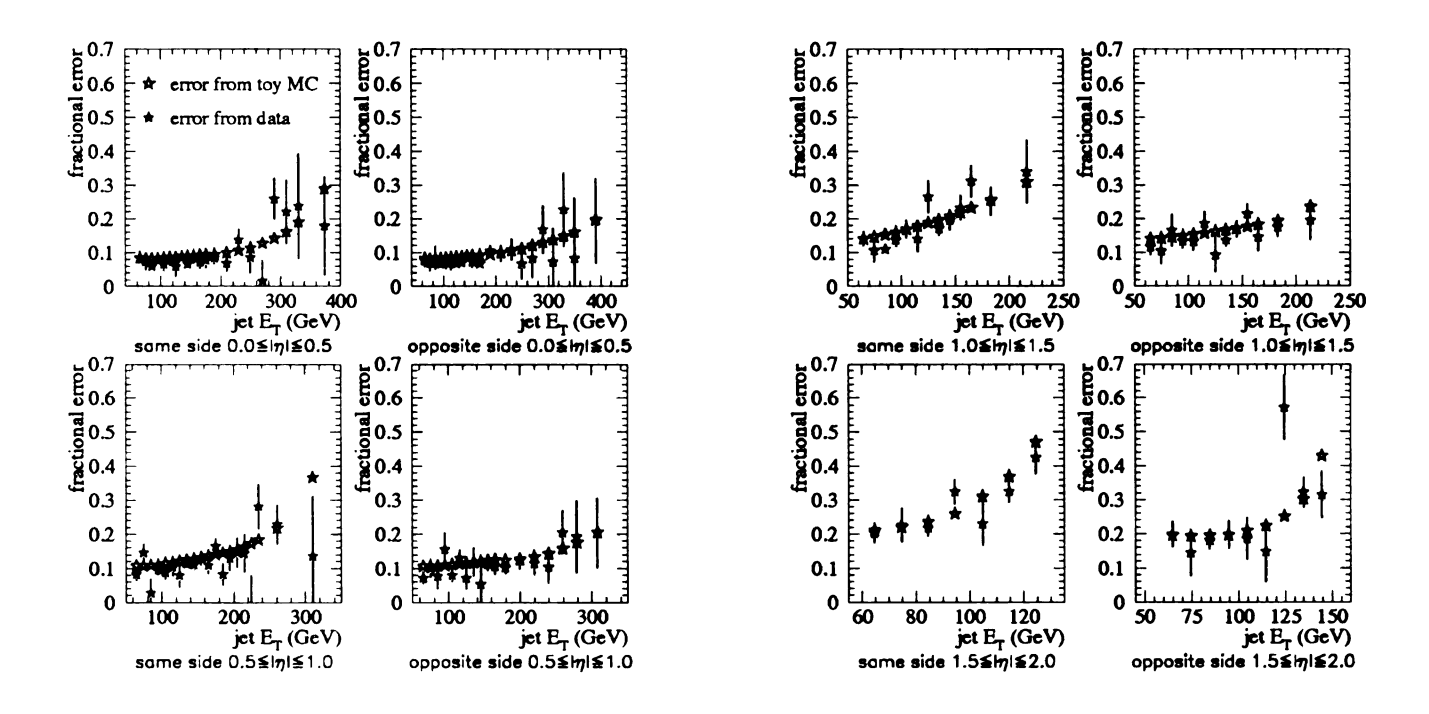


Figure 6.18: Comparison of energy scale errors from data and from the toy Monte Carlo used to study the energy scale error correlations.

Finally, the energy scale correlation matrix can be studied to assure reasonable (within  $\pm 1$ ) correlations. This matrix is presented in Figure 6.19.

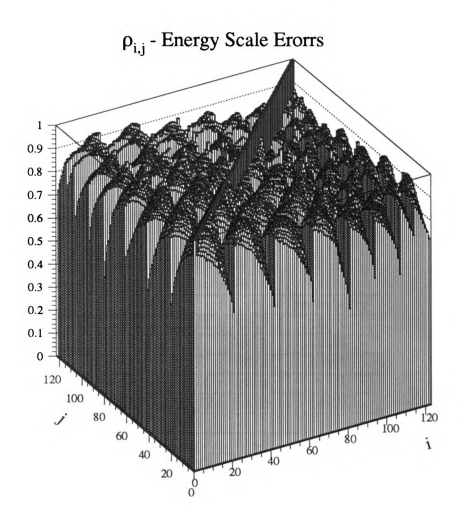


Figure 6.19: The correlation matrix for errors associated with the energy scale correction.

#### 6.2.3 $\chi^2$ Tests

Now that we have the covariance matrix for the energy scale errors and for all other errors we can add them together to create the covariance matrix for the Triple Differential. Once this matrix exists, a  $\chi^2$  test can be performed. This provides a means to quantify the measured data's agreement with theory. The variable takes the form:

$$\chi^2 = \sum_{j=1}^{123} \sum_{i=1}^{123} (D_i - T_i) \sigma_{i,j}^{-1} (D_j - T_j).$$
 (6.1)

In Equation 6.1,  $D_i(T_i)$  is the data(theory) point in bin i,  $\sigma_{i,j}$  is the covariance matrix for the Triple Differential.

We present the results of the  $\chi^2$  test for the different theories in Table 6.5, the probability presented in the table defines the likelihood that each theory describes the data.

Theory	$\chi^2$	probability
CTEQ3M $\mu = E/2$	138.2	16.5%
CTEQ3M $\mu = E$	153.1	3.4%
CTEQ3M $\mu = 2E$	180.3	0.06%
CTEQ3M $\mu = E/4$	160.4	1.3%
CTEQ3M $\mu = E_T/2$	140.8	13.1%
CTEQ4M $\mu = E/2$	119.8	56.4%
CTEQ4HJ $\mu = E/2$	142.1	12.8%
MRST $\mu = E/2$	147.02	6.9%
MRSTg $\uparrow \mu = E/2$	115.95	66.1%
MRSTg $\downarrow \mu = E/2$	221.56	$1.3 \times 10^{-5}\%$

Table 6.5:  $\chi^2$  test results for the Triple Differential, there are 123 degrees of freedom in the measurement.

#### 6.2.4 Conclusion

The Triple Differential has been measured in the region  $|\eta| \leq 2.0$ . We have argued that the measurement should be sensitive to variations in the theoretical predictions.

Observe, in Table 6.5, that the result appears to have considerable discriminatory capability. We present the  $\chi^2$  test as an example of the power of the result. This measurement would be better utilized as an *input* to a global parton distribution function fit. This would represent a more accurate input than currently available from any previous study of hadron-hadron jet data. As it stands alone, the Triple Differential prefers the CTEQ4M and the MRST $g \uparrow$  parton distributions evaluated at renormalization and factorization scales  $\mu_f, \mu_\tau = E/2$ .

## Appendix A

### Resolution Monte Carlo Closure

This appendix describes the Monte Carlo closure test of the resolution measurement.

### A.1 Zero Bias Overlay

Data are overlaid by a package which fills an imaginary calorimeter first with particles from the Herwig Monte Carlo event generator and then with the average energy detected by the DØ detector during a zero bias event. This is useful to more closely model real data during taken running. This procedure is expected to provide a good approximation to actual DØ data but has the advantage that the energy of the particle jets is known.

#### A.2 Closure Tests

To check the Di-jet asymmetry method of resolution measurement, the *straight* resolutions are calculated. The straight resolutions are the actual transverse energy

resolution of the DØ detector modeled by Monte Carlo. A particle jet of known energy is created and sent into the DØ calorimeter. All detector effects are accounted for and the jet energy is again measured at the calorimeter level. The quantity  $E_{T\ cal}-E_{T\ part}$  is measured and defined as the straight or true resolution.  $E_{T\ cal}$  refers to the transverse energy of the calorimeter jet and  $E_{T\ part}$  to the corresponding particle jet. The straight resolutions are compared to the resolutions obtained via the di-jet asymmetry method from the same Monte Carlo data. Figure A.1 contains the difference between the straight resolutions and the resolutions obtained from the di-jet asymmetry method for the central and forward  $\eta$  regions. The upper and lower curves define the closure error applied to the measured energy resolutions. This curve is parameterized by  $d_1/E_T^2+d_2$  where  $d_1=14.3$  and  $d_2=0.0024$ . This parameterization represents the 68% confidence interval for closure; if many data points existed, 68% of them would be contained within this curve.

The data necessary to perform this study were only generated for the most forward ( $|\eta| > 1.6$ ) and the central ( $|\eta| < 0.4$ ) pseudo-rapidity bins.

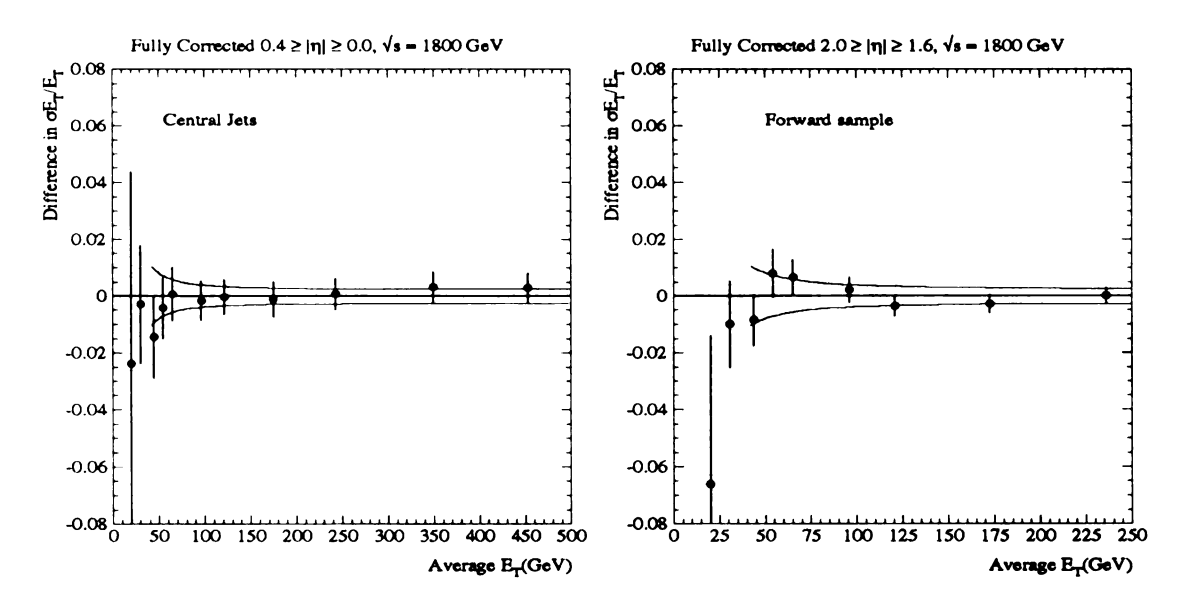


Figure A.1: Monte Carlo closure of the di-jet asymmetry method for central (left) and forward (right) jets.

## A.2.1 Vertex Position Resolution and Energy Resolution Closure

As discussed in Chapter 5, in the presence of imperfect vertex position resolution, the same side asymmetries are expected to represent the jet energy resolutions only and the opposite side resolutions are expected to be sensitive to the effective vertex resolution. In order to investigate this effect, the Monte Carlo was amended to model the vertex resolution measured in the data. During this test, for the calorimeter jets used in the asymmetry measurement, the jet quantities were calculated assuming imperfect vertex position resolution. The energy resolutions were calculated for the same and opposite side samples as well as for the combined sample. The results are presented in Figure A.2 for the forward slice. One can observe good agreement in the same side case, but not in the opposite side or the combined sample. This supports the claim that the same side resolutions are the ones to use to correct for the finite energy resolution of the DØ calorimeter. The same side energy resolutions only are used in this analysis to represent the energy resolution of the DØ calorimeter.

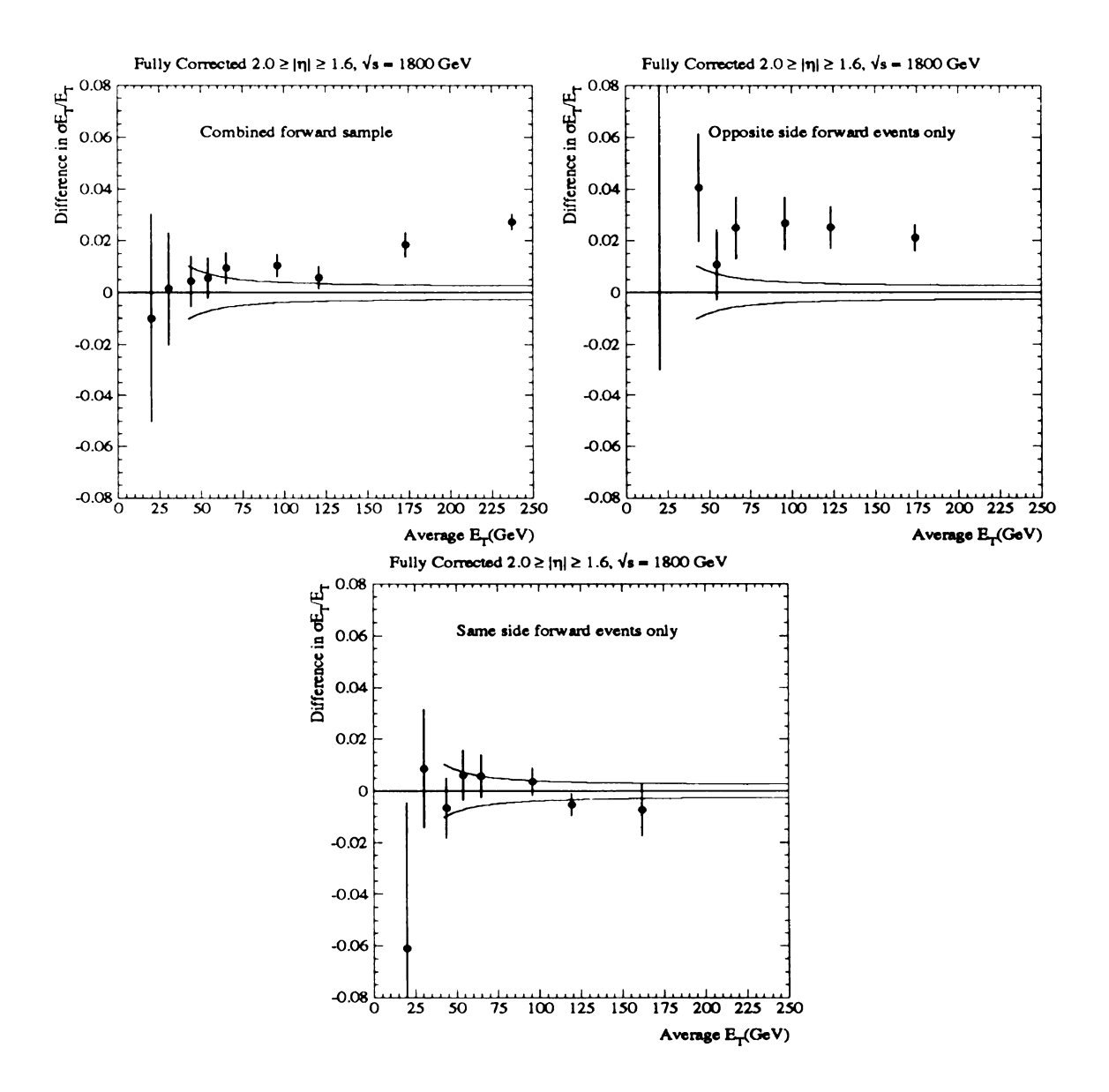


Figure A.2: Monte Carlo closure measurement with an input vertex resolution for the combined sample (top left), the opposite side sample (top right) and the same side sample (bottom left).

## Appendix B

## **Numerical Cross Sections**

This appendix contains the numerical Triple Differential results.

$E_T$	Cross Section	error (stat)	error(sys)
0.646E + 02	0.947E+03	0.169E+02	0.980E + 02
0.746E+02	0.422E+03	0.113E+02	0.425E+02
0.847E + 02	0.209E+03	0.217E+01	0.196E+02
0.947E+02	0.114E+03	0.161E+01	0.110E+02
0.105E+03	0.655E+02	0.122E+01	0.628E+01
0.115E+03	0.407E+02	0.965E+00	0.408E+01
0.125E+03	0.222E+02	0.714E+00	0.205E+01
0.135E+03	0.142E+02	0.166E+00	0.122E+01
0.145E+03	0.933E+01	0.135E+00	0.837E+00
0.155E+03	0.625E+01	0.110E+00	0.558E+00
0.165E+03	0.405E+01	0.888E-01	0.363E+00
0.175E+03	0.296E+01	0.760E-01	0.291E+00
0.189E+03	0.173E+01	0.317E-01	0.172E+00
0.209E+03	0.924E+00	0.231E-01	0.106E+00
0.229E+03	0.482E+00	0.167E-01	0.594E-01
0.249E+03	0.243E+00	0.118E-01	0.298E-01
0.270E + 03	0.149E+00	0.926E-02	0.225E-01
0.290E+03	0.931E-01	0.729E-02	0.172E-01
0.310E+03	0.427E-01	0.491E-02	0.707E-02
0.330E+03	0.153E-01	0.292E-02	0.191E-02
0.371E+03	0.418E-02	0.719E-03	0.628E-03

Table B.1: The DØ Triple Differential for same side events,  $|\eta| \leq 0.5$ . Units on the cross section and errors are picobarns,  $E_T$  is in GeV.

$E_T$	Cross Section	error (stat)	error(sys)
0.646E+02	0.865E + 03	0.151E + 02	0.101E+03
0.746E+02	0.375E + 03	0.996E+01	0.425E+02
0.847E+02	0.183E+03	0.698E + 01	0.199E+02
0.947E+02	0.968E+02	0.138E+01	0.109E+02
0.105E+03	0.540E + 02	0.103E+01	0.626E+01
0.115E+03	0.298E+02	0.764E+00	0.338E+01
0.125E+03	0.167E + 02	0.572E+00	0.185E+01
0.135E+03	0.108E+02	0.134E+00	0.126E+01
0.145E+03	0.658E+01	0.104E+00	0.781E+00
0.155E+03	0.403E+01	0.812E-01	0.468E+00
0.165E+03	0.262E+01	0.652E-01	0.317E+00
0.175E + 03	0.170E+01	0.404E-01	0.222E+00
0.185E+03	0.104E+01	0.315E-01	0.133E+00
0.195E+03	0.766E+00	0.269E-01	0.110E+00
0.205E+03	0.485E+00	0.212E-01	0.754E-01
0.215E+03	0.309E+00	0.169E-01	0.446E-01
0.225E+03	0.193E+00	0.132E-01	0.285E-01
0.235E+03	0.174E+00	0.124E-01	0.361E-01
0.261E+03	0.464E-01	0.279E-02	0.856E-02
0.310E + 03	0.558E-02	0.870E-03	0.146E-02

Table B.2: The DØ Triple Differential for same side events,  $0.5 \le |\eta| \le 1.0$  Units on the cross section and errors are picobarns,  $E_T$  is in GeV.

$E_{T}$	Cross Section	error (stat)	error(sys)
0.646E+02	0.566E + 03	0.120E+02	0.631E + 02
0.746E+02	0.255E + 03	0.813E+01	0.330E+02
0.847E+02	0.998E + 02	0.138E+01	0.114E+02
0.947E+02	0.515E+02	0.992E+00	0.629E+01
0.105E+03	0.241E+02	0.677E+00	0.305E+01
0.115E+03	0.131E+02	0.498E+00	0.181E+01
0.125E+03	0.627E+01	0.342E+00	0.945E+00
0.135E+03	0.322E+01	0.706E-01	0.493E+00
0.145E+03	0.185E+01	0.529E-01	0.316E+00
0.155E+03	0.939E+00	0.372E-01	0.165E+00
0.165E+03	0.510E+00	0.270E-01	0.931E-01
0.183E+03	0.132E+00	0.589E-02	0.262E-01
0.215E+03	0.145E-01	0.152E-02	0.484E-02
0.301E+03	0.366E-03	0.948E-04	0.735E-03

Table B.3: The DØ Triple Differential for same side events  $1.0 \le |\eta| \le 1.5$ . Units on the cross section and errors are picobarns,  $E_T$  is in GeV.

$E_T$	Cross Section	error (stat)	error(sys)
0.645E+02	0.261E+03	0.828E + 01	0.522E + 02
0.745E+02	0.892E+02	0.482E+01	0.167E + 02
0.845E+02	0.291E+02	0.739E+00	0.537E+01
0.946E+02	0.106E+02	0.440E+00	0.197E+01
0.105E+03	0.348E+01	0.246E+00	0.662E+00
0.115E+03	0.104E+01	0.378E-01	0.215E+00
0.124E+03	0.359E+00	0.211E-01	0.903E-01
0.138E+03	0.592E-01	0.541E-02	0.135E-01

Table B.4: The DØ Triple Differential for same side events,  $1.5 \le |\eta| \le 2.0$ . Units on the cross section and errors are picobarns,  $E_T$  is in GeV.

$E_T$	Cross Section	error (stat)	error(sys)
0.646E+02	0.960E + 03	0.171E+02	0.982E + 02
0.746E+02	0.453E + 03	0.118E + 02	0.450E + 02
0.847E + 02	0.227E + 03	0.838E + 01	0.237E+02
0.947E+02	0.119E+03	0.165E+01	0.111E+02
0.105E+03	0.659E + 02	0.123E+01	0.624E+01
0.115E+03	0.388E+02	0.943E+00	0.357E+01
0.125E+03	0.234E+02	0.213E+00	0.198E+01
0.135E+03	0.153E + 02	0.173E+00	0.136E+01
0.145E+03	0.101E+02	0.140E+00	0.908E+00
0.155E+03	0.624E+01	0.110E+00	0.554E+00
0.169E + 03	0.379E + 01	0.469E-01	0.362E+00
0.189E+03	0.182E+01	0.326E-01	0.179E+00
0.209E+03	0.903E+00	0.229E-01	0.940E-01
0.229E+03	0.499E+00	0.170E-01	0.572E-01
0.249E+03	0.244E+00	0.119E-01	0.276E-01
0.270E + 03	0.144E+00	0.912E-02	0.184E-01
0.290E+03	0.877E-01	0.711E-02	0.129E-01
0.310E+03	0.552E-01	0.564E-02	0.988E-02
0.330E+03	0.334E-01	0.438E-02	0.587E-02
0.350E + 03	0.140E-01	0.283E-02	0.244E-02
0.390E+03	0.745E-02	0.110E-02	0.220E-02

Table B.5: The DØ Triple Differential for opposite side events,  $|\eta| \leq 0.5$ . Units on the cross section and errors are picobarns,  $E_T$  is in GeV.

$E_T$	Cross Section	error (stat)	error(sys)
0.646E+02	0.885E + 03	0.154E+02	0.100E+03
0.746E+02	0.427E + 03	0.107E + 02	0.513E+02
0.847E + 02	0.205E+03	0.743E + 01	0.235E+02
0.947E + 02	0.108E+03	0.538E+01	0.122E+02
0.105E+03	0.591E+02	0.108E+01	0.663E+01
0.115E+03	0.348E+02	0.830E+00	0.408E+01
0.125E+03	0.199E+02	0.627E+00	0.221E+01
0.135E+03	0.116E+02	0.480E+00	0.128E+01
0.145E+03	0.759E+01	0.387E+00	0.860E+00
0.155E+03	0.487E+01	0.899E-01	0.557E+00
0.165E+03	0.334E+01	0.743E-01	0.397E+00
0.179E+03	0.189E+01	0.304E-01	0.235E+00
0.199E+03	0.917E+00	0.211E-01	0.128E+00
0.219E+03	0.427E+00	0.143E-01	0.610E-01
0.239E+03	0.227E+00	0.104E-01	0.373E-01
0.259E+03	0.112E+00	0.723E-02	0.191E-01
0.279E + 03	0.383E-01	0.421E-02	0.473E-02
0.308E+03	0.198E-01	0.211E-02	0.367E-02
0.358E+03	0.615E-02	0.860E-03	0.235E-02

Table B.6: The DØ Triple Differential for opposite side events,  $0.5 \le |\eta| \le 1.0$ . Units on the cross section and errors are picobarns,  $E_T$  is in GeV.

$E_T$	Cross Section	error (stat)	error(sys)
0.646E+02	0.470E + 03	0.111E+02	0.640E+02
0.746E+02	0.205E+03	0.734E+01	0.275E+02
0.847E + 02	0.106E+03	0.530E+01	0.164E+02
0.947E + 02	0.443E+02	0.932E+00	0.569E+01
0.105E+03	0.250E + 02	0.700E+00	0.356E+01
0.115E+03	0.138E+02	0.521E+00	0.207E+01
0.125E+03	0.771E+01	0.389E+00	0.124E+01
0.135E+03	0.437E+01	0.849E-01	0.686E+00
0.145E+03	0.263E+01	0.656E-01	0.424E+00
0.155E+03	0.153E+01	0.500E-01	0.278E+00
0.165E+03	0.908E+00	0.383E-01	0.167E+00
0.183E + 03	0.372E+00	0.108E-01	0.740E-01
0.213E+03	0.813E-01	0.495E-02	0.186E-01
0.255E+03	0.912E-02	0.103E-02	0.252E-02

Table B.7: The DØ Triple Differential for opposite side events,  $1.0 \le |\eta| \le 1.5$ . Units on the cross section and errors are picobarns,  $E_T$  is in GeV.

$E_T$	Cross Section	error (stat)	error(sys)
0.645E+02	0.159E + 03	0.652E + 01	0.224E+02
0.746E+02	0.584E + 02	0.397E+01	0.784E+01
0.846E+02	0.266E + 02	0.730E+00	0.488E+01
0.947E + 02	0.105E+02	0.459E+00	0.192E+01
0.105E+03	0.485E+01	0.312E+00	0.890E+00
0.115E+03	0.238E + 01	0.218E+00	0.533E+00
0.125E+03	0.112E+01	0.149E+00	0.277E+00
0.135E+03	0.549E+00	0.298E-01	0.157E+00
0.145E+03	0.252E+00	0.196E-01	0.733E-01
0.163E+03	0.581E-01	0.490E-02	0.207E-01

Table B.8: The DØ Triple Differential for opposite side events,  $1.5 \le |\eta| \le 2.0$ . Units on the cross section and errors are picobarns,  $E_T$  is in GeV.

### References

- [1] Yu. L. Dokshitzer, V.A. Khoze, A.H. Mueller and S.I. Troyan, "Basics of Perturbative QCD", Editions Frontières, 1991.
- [2] Francis Halzen and Alan Martin, "Quarks and Leptons: An Introductory Course in Modern Particle Physics", John Wiley and Sons, 1984.
- [3] David Griffiths, "Introduction to Elementary Particles", John Wiley and Sons, 1987.
- [4] J. Thompson, "Introduction to Colliding Beams at Fermilab", FERMILAB-TM-1909, 1994.
- [5] B. Abbott et al. "Direct Measurement of the Top Quark Mass at D0" hepex/801025, Fermilab-Pub-98/031-E, January, 1998.
- [6] F. Abe et al. "Observation of Top Quark Production in  $p\bar{p}$  Collisions with the CDF Detector at Fermilab", Fermilab-Pub-95/022-E
- [7] G. Marchesini (Parma U. & INFN, Parma), B.R. Webber (Cambridge U.), G. Abbiendi (Padua U. & INFN, Padua), I.G. Knowles (Glasgow U.), M.H. Seymour (Cambridge U.), L. Stanco (Padua U. & INFN, Padua). CAVENDISH-HEP-91-26, May 1991.

- [8] W.T. Giele, E.W.N. Glover, and D.A. Kosower, Phys. Rev. Letters **73**, 2019 (1994).
- [9] Kate Frame et al., "Trigger Efficiencies for Run 1B Inclusive Jet Triggers", DØ Internal Note # 3178, September 23, 1996 (Unpublished).
- [10] Levan Babukhadia et al., "Standard Jet Cuts and their Efficiencies for Run 1B DØ Collider Data", DØ Internal Note # 3407, March 27, 1998 (Unpublished).
- [11] B. Abbott *et al.*, "Determination of the Absolute Jet Energy Scale in the DØ Calorimeters", Fermilab-Pub-97/330-E.
- [12] Gian Di Loreto, "The Derivation of the Offset Correction for Run 1B Cone Jets Implemented in Cafix 5.1", DØ Internal Note # 3542, October 23, 1998 (Unpublished).
- [13] S. Abachi et al., "The DØ detector", Nuclear Instruments and Methods, A338, 185, (1994).
- [14] J. Bantly et al., "The DØ Luminosity Monitor Constant for the 1994-1996 Tevatron Run", Fermilab-TM-1995, DØ Note 3199, Feb, 1, 1997.
- [15] E. Glover and Dave Kosower, "Recombination Methods for Jets in  $p\bar{p}$  Collisions", hep-ph/9510420, October 26, 1995.
- [16] S. Ellis et al. in Research Directions for the Decade, Proceedings of the Summer Study, Snowmass, Colorado, 1990, ed. E. L. Berger (World Scientific, Singapore, 1992).

- [17] Mrinmoy Bhattacharjee et al., "Jet Energy Resolutions", DØ Internal Note # 2887, May 22, 1996 (Unpublished).
- [18] Brad Abbott, "Effects of  $\eta$  and  $\phi$  Definitions on Reconstructing Jets", DØ Internal Note # 2769, November 10, 1995 (Unpublished).
- [19] Victor Daniel Elvira, "Jet  $\eta$  bias and resolution", DØ Internal Note # 2173, June 8, 1994 (Unpublished).
- [20] Kim, Heuring, Jun, "Position Biases and Resolutions in Jet Measurements"
  DØ Internal Note # 3407, February 15, 1995 (Unpublished).
- [21] H. Schellman, "The Relation Between  $E_T$ , Asymmetry, Jet Resolutions and Vertex Resolution" DØ Internal Note #3454, May 8,1998 (Unpublished).
- [22] Victor Daniel Elvira, "Measurement of the Inclusive Jet Cross Sections at  $\sqrt{s} = 1.8 TeV$  with the DØ detector" Ph.D. thesis, 1994 (Unpublished).
- [23] "Parton Distributions: A New Global Analysis", A.D. Martin, R.G. Roberts,W.J. Stirling, and R.S. Thorne, hep-ph/9803445, March, 1998.

MICHIGAN STATE UNIV. LIBRARIES
31293017663109